



## 저작자표시-비영리-변경금지 2.0 대한민국

이용자는 아래의 조건을 따르는 경우에 한하여 자유롭게

- 이 저작물을 복제, 배포, 전송, 전시, 공연 및 방송할 수 있습니다.

다음과 같은 조건을 따라야 합니다:



저작자표시. 귀하는 원저작자를 표시하여야 합니다.



비영리. 귀하는 이 저작물을 영리 목적으로 이용할 수 없습니다.



변경금지. 귀하는 이 저작물을 개작, 변형 또는 가공할 수 없습니다.

- 귀하는, 이 저작물의 재이용이나 배포의 경우, 이 저작물에 적용된 이용허락조건을 명확하게 나타내어야 합니다.
- 저작권자로부터 별도의 허가를 받으면 이러한 조건들은 적용되지 않습니다.

저작권법에 따른 이용자의 권리는 위의 내용에 의하여 영향을 받지 않습니다.

이것은 [이용허락규약\(Legal Code\)](#)을 이해하기 쉽게 요약한 것입니다.

[Disclaimer](#)

**Ph. D. DISSERTATION**

**Development of a cathodoluminescence system for TEM  
and its applications to the investigation of bandgap-  
transition characteristics of GaN and MoS<sub>2</sub>**

투과전자현미경용 음극형광 분석 시스템 개발과 이를  
활용한 GaN과 MoS<sub>2</sub> 밴드갭 천이 특성에 관한 연구

**by**

**Mi-Hyang Sheen**

**February 2017**

**Department of Materials Science and Engineering**

**College of Engineering**

**Seoul National University**

## Abstract

---

Cathodoluminescence (CL) is an optical and an electrical phenomenon arising from interactions between accelerated electrons and materials. When the highly energetic electrons exposed on a luminescent material, the primary electrons excite the electrons in the matter, and the excited electrons release its excess energy as photons in accordance with their internal transitions. The CL spectroscopy provides invaluable information on electronic structure such as bandgap energy, excitonic states, impurity-, and dopant-levels. In this thesis, the developments of the CL system for transmission electron microscopy (TEM) and its applications to semiconductor research were presented.

Firstly, it was developed that the novel TEM-CL holder with a retractable light-collecting optics, which is composed of miniaturized optical components and integrated on head part of the holder. By moving the whole optics isolated from built-in cryostat, large CL observation area and successive measurement of EDS signal were guaranteed while maintaining accurate alignment of the optics. Performance and applicability of the system were demonstrated by analyzing ZnO nanowires.

Secondly, the TEM-CL analysis results of polar (0001) GaN light-emitting diodes (LEDs) were discussed. The luminescence properties of V-shape pits, which are the characteristic defects in c-plane InGaN/GaN quantum well structures, were directly correlated with its microstructure. It was clearly revealed that potential barriers, formed by discontinuous QWs around the hexagonal pit, can effectively block the diffusion of carriers into the  $\{10\bar{1}1\}$ -faceted quantum well structures (QWs) and threading dislocations (TDs), which in turn increases the effective carrier density usable for radiative recombination.

Thirdly, the emission properties of the semi-polar (11 $\bar{2}2$ )-GaN LEDs were analyzed. The CL maps clearly identify the type of the extended defects and visualize their distribution at a glance. In addition, it was directly observed that the influence of substrate pattern on the defect reduction. The characteristic surface undulations of the semi-polar (11 $\bar{2}2$ ) GaN epi were also investigated. It was clearly observed that the undulations are also present in QWs composed of the flat

(11 $\bar{2}2$ ) facets and the sidewall {01 $\bar{1}1$ } facets. The high In-incorporation efficiency of the sidewall {01 $\bar{1}1$ } facets caused high In composition and long wavelength emission, resulting in non-uniform luminescence and anisotropic emission of LED. It is expected that this result will assist the analysis on the characteristics of the semi-polar GaN epi and the development of the high efficiency GaN LEDs.

Lastly, the luminescence properties of few-layered MoS<sub>2</sub> were investigated with the optical excitation and the electron beam excitation. As a result, it was observed the peak A and B due to direct excitonic transitions at K point in both photoluminescence (PL) and CL. The large peak C, which is more close to the quasiparticle bandgap energy, is appeared only in CL. Based on previously reported calculation works, the peak C may correspond to nearly degenerate excitonic transitions near  $\Gamma$  point. The luminescence of the high-energy exciton in MoS<sub>2</sub> was firstly observed and investigated. I believe that these results provide insight into understanding the excitonic behavior of MoS<sub>2</sub> and exploring novel optoelectronic applications.

**Keyword:** Cathodoluminescence, Transmission electron microscopy, defects, Dislocation, Stacking faults, Quantum well, GaN, Light-emitting diodes, MoS<sub>2</sub>

**Student ID:** 2013-30182

Mi-Hyang Sheen

# Table of Contents

---

<b>Abstract .....</b>	<b><i>i</i></b>
<b>Table of Contents .....</b>	<b><i>iii</i></b>
<b>List of Tables .....</b>	<b><i>v</i></b>
<b>List of Figures .....</b>	<b><i>vi</i></b>
Chapter 1. Introduction .....	1
1. 1. Background .....	1
1. 2. Scopes and contents .....	4
1. 3. Bibliography .....	5
Chapter 2. PART I: Development of a novel CL stage with retractable light- collecting optics for TEM .....	6
2. 1. Introduction .....	6
2. 2. Experimental details .....	9
2. 3. Results and discussions .....	15
2. 4. Bibliography .....	20
Chapter 3. PART II: Investigation of bandgap-transition characteristics of GaN and MoS <sub>2</sub> .....	22
3. 1. Role of V-pits as a diffusion barrier for carriers in polar InGaN/GaN quantum wells .....	22
3. 1. 1. Introduction .....	22
3. 1. 2. Experimental details .....	24
3. 1. 3. Results and discussions .....	25
3. 1. 4. Bibliography .....	33

3. 2. Directly visualized distributions of $I_1$ - and $I_2$ -BSFs in semipolar $(11\bar{2}2)$ GaN thin film.....	35
3. 2. 1. Introduction .....	35
3. 2. 2. Experimental details .....	42
3. 2. 3. Results and discussions .....	43
3. 2. 4. Bibliography .....	51
3. 3. Correlation study between the surface morphology and the luminescence characteristics of semipolar $(11\bar{2}2)$ InGaN/GaN quantum wells.....	54
3. 3. 1. Introduction .....	54
3. 3. 2. Experimental details .....	56
3. 3. 3. Results and discussions .....	57
3. 3. 4. Bibliography .....	65
3. 4. Directly observed interband transitions in few-layered $\text{MoS}_2$ by using cathodoluminescence.....	67
3. 4. 1. Introduction .....	67
3. 4. 2. Experimental details .....	70
3. 4. 3. Results and discussions .....	72
3. 4. 4. Bibliography .....	84
Chapter 4. Conclusions .....	86
Abstract (in Korean) .....	88

## List of Tables

---

Table 3.2.1. Dislocations and planar defects in hexagonal structure.

**b**: Burger's vector, **R**: displacement vector.

Table 3.2.2. Characteristic emission energies of the defects in GaN. FE: free exciton, BSFs: basal-plane stacking faults, PSFs: prismatic stacking faults, PDs: partial dislocations, and DAP: donor-acceptor pair.

## List of Figures

---

- Figure 1.1.1. A schematic diagram of the electron transitions associated with non- and radiative recombination processes
- Figure 2.1.1. An electron beam-specimen interaction in general TEM-CL stage with a parabolic mirror
- Figure 2.1.2. Design and fabrication of CL stage with a retractable mirror: (a, d) overall appearance of CL stage, (b, e) head part with locating the mirror at a closed position for CL signal collection, (c, f) head part with locating the mirror at an opened position for characteristic X-ray signal collection (c, f).
- Figure 2.1.3. A photograph of a whole TEM-CL acquisition system
- Figure 2.1.4. Sequential TEM images during a retraction of the mirror: (a) at a position for CL signal collection, (b, c) at intermediate positions (d) at a position for characteristic X-ray signal collection.
- Figure 2.1.5. Collection of CL signals under low-temperature: (a) Temperature change of the CL stage after pouring liquid nitrogen into the dewar (b) CL point spectra of ZnO nanowires before and after CL stage cooling. The inset figures in (b) represent the position of an electron beam with red spots.
- Figure 2.1.6. Successive acquisition of a CL and a EDS signal: (a) TEM bright field image of ZnO nanowires. A red spot indicates a position of an electron beam (b) CL point spectrum (c) EDS point spectrum. The inset figures of (b) and (c) show the position of the mirror at each measurement.
- Figure 2.1.7. Successive acquisition of the CL and EDS map of ZnO nanowires: (a) TEM bright field image (b) CL intensity map ( $\lambda$ : 375–385 nm) (c) EDS map of Zn-K $\alpha$  (d) EDS map of O-K $\alpha$ .
- Figure 3.1.1. Bright field TEM images of an LED specimen. (a) Cross-section view and (b) Plan-view with the selected area diffraction pattern of the same area in the inset. (c) Schematic diagram of the structure near the V-pit in InGaN/GaN QW.



Figure 3.1.2. The luminescence characteristics of the V-pit analyzed by TEM-CL from a cross-sectional LED specimen. (a) STEM-ADF image of the V-pit. Yellow dotted line indicates the CL line scan position and direction. White arrows indicate the TD core (A),  $\{10\bar{1}1\}$ -faceted QWs (B), V-pit corner (C), and C-plane QWs (D). (b) Hyperspectral CL map along the yellow dotted line in (a). The x-axis indicates to the spatial position in the scan line and the y-axis indicates the wavelength. The relative CL intensity is represented with a color scale from black to white. (c) CL point spectra of the four regions marked with white arrows in (a) and (b).

Figure 3.1.3. The optical behaviors of V-shaped pit are analyzed by TEM-CL on cross-sectional LED specimen. (a) Bright field image of the active region shows that the MQWs were affected by the V-shaped pit with white circle. (b) Panchromatic CL map on the same area ( $\lambda$ : 350–500 nm) presented the NRC of TD crossing active regions. Monochromatic CL map of flat MQWs ( $\lambda$ : 460–490 nm) (c) and v-defect sidewall ( $\lambda$ : 370–390 nm) (d). (e) RG composite image (R: flat QWs, G: sidewall QWs). (f) Red-Green composite color CL map of the V-pit overlapped on its STEM image. Red indicates the emission of C-plane QWs ( $\lambda$ : 460–490 nm), and green indicates the emission of  $\{10\bar{1}1\}$ -faceted QWs ( $\lambda$ : 370–390 nm). (g) A high-resolution TEM image including the V-pit corner. The white arrows indicate the positions of the V-pit corners, i.e.,  $\{10\bar{1}1\}$ -plane to C-plane QW transition zone.

Figure 3.1.4. A plan-view of the luminescence mapping of an LED specimen, with wavelength windows equivalent to  $\{10\bar{1}1\}$ -plane and C-plane emission. Monochromatic CL wavelength mappings from (a) 370–390 nm ( $\sim\{10\bar{1}1\}$ -faceted QW), (b) 460–475 nm ( $\sim$ C-plane QW), and (c) 475–490 nm. (d) Red-green composite color CL mapping of R- and C-plane QW emission wavelengths in green and red, respectively. Positions of the (A) TD core, (B)  $\{10\bar{1}1\}$ -faceted QWs, (C) V-pit corner, (D) extra emission of C-plane QWs near the V-pit

corner, and (\*) normal C-plane QW emissions. (e) Inset is Hyperspectral CL map along the yellow arrow on (d).

Figure 3.2.1. (a) Electronic band structure of strained InGaN/GaN QWs. (b) Schematics of crystallographic planes of typical polar, non- and semi-polar GaN.

Figure 3.2.2. Schematic diagram of semipolar  $(11\bar{2}2)$  GaN film.

Figure 3.2.3. (a) A cross-section view TEM-BF image of the  $(11\bar{2}2)$  GaN based LED specimen. Monochromatic CL intensity maps from the emission of (b) NBE (3.48 – 3.45 eV), (c)  $I_1$  type BSFs (3.44-3.41 eV), (d)  $I_2$  type BSFs (3.39 – 3.35 eV), (e) PDs and PSFs (3.34 – 3.29 eV), and (f) MQWs (2.81 – 2.67 eV).

Figure 3.2.4. CL point spectra of the extended defects (a) and MQWs (b) in the cross-section view  $(11\bar{2}2)$  GaN based LED specimen. Solid line represents Gaussian fitted curves and grey dots show measured CL spectra in (a).

Figure 3.2.5. (a) A cross-section view TEM-BF image of the  $(11\bar{2}2)$  GaN based LED specimen. Monochromatic CL intensity maps from the emission of (b) NBE (3.48 – 3.45 eV) and (c)  $I_1$  type BSFs (3.42 – 3.40 eV), (d)  $I_2$  type BSFs (3.37 – 3.36 eV), (e) PDs and PSFs (3.33 – 3.21 eV), and Red-green composite color map (f). Red: NBE (3.48 – 3.45 eV) and Green: PSFs (3.33 – 3.21 eV).

Figure 3.2.6. A plan-view TEM-BF image (a) and a panchromatic CL map (2.48 – 3.54 eV) of  $(11\bar{2}2)$  p-GaN film (b). Monochromatic CL intensity maps from the emission of (c) NBE (3.48 – 3.45 eV), (d)  $I_1$  type BSFs (3.42-3.41 eV), (e)  $I_2$  type BSFs (3.37 – 3.34 eV), and (f) PDs and PSFs (3.33 – 3.28 eV).

Figure 3.2.7. (a) Red-Green-Blue (RGB) composite color CL map. Red: NBE (3.48 – 3.45 eV), Green:  $I_2$  type BSFs (3.37 – 3.34 eV), and Blue:  $I_1$  type BSFs (3.42-3.41 eV). (b) Red-Green composite color CL map. Red: NBE (3.48 – 3.45 eV) and Green: PDs and PSFs (3.33 – 3.28 eV). (c) CL point spectra of four points labeled  $\alpha$ ,  $\beta$ ,  $\gamma$ , and  $\delta$  in (a) and (b).

Figure 3.3.1. Cross-sectional ADF STEM image of the  $(11\bar{2}2)$  semipolar

InGaN/GaN LED structure grown on the HPSS.

Figure 3.3.2. (a) Cross-sectional BF image of the specimen and (b) panchromatic CL map ( $\lambda$ : 350-550 nm) of the region of (a). (c) CL point spectra of the two regions labeled GaN-A and GaN-B in (b). (d) CL point spectra of the two regions labeled flat MQWs and sidewall MQWs in (b).

Figure 3.3.3. Monochromatic CL intensity mapping from the emission of (a) NBE and BSFs ( $\lambda$ : 360-370 nm), (b) PDs and PSFs ( $\lambda$ : 373-380 nm), (c) the intersection of the flat MQW and the sidewall MQWs ( $\lambda$ : 425-445 nm), (d) flat MQWs ( $\lambda$ : 410-425 nm), (e) sidewall MQWs ( $\lambda$ : 445-485 nm). (f) Red-green-yellow (RGY) composite color CL map. Red color indicates the emission of sidewall MQWs, green color represents the emission of flat MQWs, and yellow color shows the emission of the NBE and BSFs. (g) ADF-STEM image of the MQWs indicated with an white arrow in (f). (g) An enlarged image of (f) is superimposed on its STEM image (g).

Figure 3.3.4. (a) The ADF-STEM image of the MQWs indicated with an white arrow in Fig. 3.3.3 (f). High-resolution ADF-STEM images of the left sidewall MQWs (b), flat MQWs (c), and right sidewall MQWs (d). (e) Schematic diagram of an atomic arrangement in semipolar ( $11\bar{2}2$ ) GaN. (f) An enlarged image of the Fig. 3.3.4 (b). (g) fast Fourier transformed (FFT) image of Fig. 3.3.4 (f).

Figure 3.3.5. (a) STEM-EDS quantification results of the flat MQWs and the sidewall MQWs. (b) STEM-EDS mapping results of the flat MQWs and the sidewall MQWs.

Figure 3.4.1. (a) Top and side views of the 2H-MoS<sub>2</sub>. Mo atoms have trigonal prismatic coordination. (b) Calculated band structure of monolayer MoS<sub>2</sub>.

Figure 3.4.2. (a) Experimental flow chart. Optical images of the MoS<sub>2</sub> flake on a SiO<sub>2</sub>/Si substrate (b) and on a perforated carbon film (c).

Figure 3.4.3. Characterizing optical properties of few-layer MoS<sub>2</sub> using laser excitation (a) An optical image of a mechanically exfoliated MoS<sub>2</sub>

flake on a SiO<sub>2</sub>/Si substrate. (b) PL spectra of the few-layer MoS<sub>2</sub> (c) Closeup of the PL spectra near the emission of SiO<sub>2</sub>/Si substrate, which is filled with gray color. (d) Raman spectra of the NL-(N = 1-3, 5 and 6) and bulk MoS<sub>2</sub>. The position of two main mode ( $E_{2g}^1$  and  $A_{1g}$ ) are indicated as dot-line. (e) Stokes and anti-Stokes Raman spectra of the few-layer MoS<sub>2</sub>.

Figure 3.4.4. (a) A bright field TEM image of the MoS<sub>2</sub> flake on the perforated carbon film. (b) CL spectra of the mono- and bi-layer MoS<sub>2</sub> (c) CL spectra of the NL-(N = 1-3, 5 and 6) MoS<sub>2</sub>.

Figure 3.4.5. Measured CL spectrum (black line) and Gaussian fitted CL spectrum (red line) of NL-(N = 1-3, 5 and 6) MoS<sub>2</sub>. Each Gaussian-fitting curve is indicated by their peak energy.

Figure 3.4.6. (a) Peak energies of the A, B, C' and C excitons with a different number of layers. (b) Peak intensities of the A, B, C' and C excitons with a different number of layers.

Figure 3.4.7. (a) A bright field TEM image and an optical image of the MoS<sub>2</sub> flake on a perforated carbon film. (b) CL spectra with a different number of layers.

Figure 3.4.8. Monochromatic CL intensity map (left) and peak wavelength map (right) from the emission of exciton A ( $\lambda$ : 475 – 560) (a, b), exciton B ( $\lambda$ : 590 – 620) (c, d) and exciton C ( $\lambda$ : 645 – 680) (e, f) in the MoS<sub>2</sub> flake on the perforated carbon film.

Figure 3.4.9. (a) A setup for TEM-CL measurement at low electron-beam acceleration voltage (80 kV) (b) CL spectra with a different electron-beam acceleration voltage.

# Chapter 1. Introduction

## 1. 1. Background

Cathodoluminescence (CL) is an optical and electrical phenomenon arising from interactions between accelerated electrons and materials. When the highly energetic electrons exposed on a luminescent material, the primary electrons excite the electrons in the matter, and the excited electrons release its excess energy as photons in accordance with their internal transitions. Therefore, the energy of the emitted photons corresponds to the difference between the initial state  $E_i$  and the final state  $E_f$  of the excited electrons:

$$h\nu = E_f - E_i$$

The CL spectroscopy provides invaluable information on electronic structure such as bandgap energy, excitonic states, impurity-, and dopant-levels.<sup>1,2</sup> Figure 1 is a schematic diagram of the electron transitions associated with non- and radiative recombination processes. The intraband transition is a thermalization process between the phonons and the electrons excited above the conduction band edge.

When this CL spectroscopy is combined with an electron microscopy, we can analyze the optical properties of the materials with microscope images. For this reason, a scanning electron microscopy (SEM) equipped with CL is generally used for analyzing various semiconductor materials. Moreover, transmission electron microscopy (TEM) equipped with CL can provide us internal structural and optical information of the material with high spatial resolution, while the SEM-CL is based on the surface information.

The CL is an emission of light resulted in recombination of electron-hole pair, which is generated in the material under electron beam bombardment. While the photon in photoluminescence (PL) tends to stimulate particular emission

process depending on their excitation energy, the high energy and large momentum of the electron beam in CL lead to excite all the possible luminescence mechanisms.<sup>3-5</sup> This unique nature of the CL enables us to observe the most of the possible interband transitions, resulting in radiative recombination. Furthermore, the electron beam can be regarded as a super-continuum source of evanescent light, suitable for creating energetic excitations, such as large band-gap semiconductor and insulators.

Therefore, the TEM-CL analysis technique enables us to analyze the optical properties of nano sized material<sup>6-10</sup> and wide bandgap semiconductor beyond the limitations of conventional PL and SEM-CL analysis.

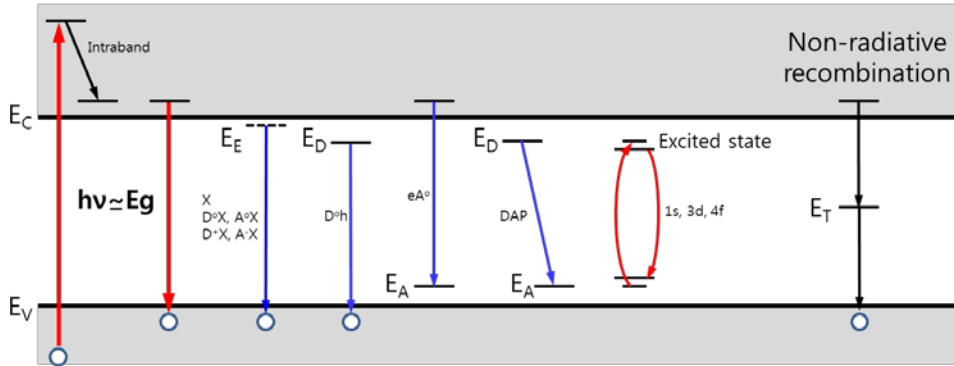


Figure 1. A schematic diagram of the electron transitions associated with non- and radiative recombination processes ( $X$ : Free-exciton recombination,  $D^0X, A^0X$ : Excitons bound to neutral impurities,  $D^+X, A^-X$ : Excitons bound to ionized impurities,  $D^0h$ : Donor-to-free-hole transition,  $eA^0$ : Free-electron-to-acceptor transition, DAP: Donor-acceptor pair and  $E_T$ : deep trap level of defects)

## 1. 2. Scopes and contents

This thesis consists of four chapters. Chapter 1 introduces the excitation mechanism of CL and important luminescence processes of the semiconductor materials. It also presents the advantages of TEM-CL technique to analyze the optical properties of the semiconductor materials.

Chapter 2 covers a fabrication of a CL system equipped with a retractable light-collecting optics. The movable optics integrated on a head part of the stage guarantee a large observation area with securing characteristic X-ray signal. The novel TEM-CL stage provide structural-, optical-, and chemical-analysis platform beyond the limitations of conventional CL system with stationary optics.

Chapter 3 presents the applications of the TEM-CL system to semiconductor research. Chapter 3.1 reports TEM-CL study on the characteristic luminescence of V-shaped pit in c-plane InGaN/GaN MQWs. It concluded that the role of V-pits as a diffusion barrier for carriers could improve the efficiency of LEDs. Chapter 3.2 presents TEM-CL analysis results of semi-polar (11 $\bar{2}$ 2)GaN using optical fingerprint method to distinguish the extended defects such as I<sub>1</sub>-, I<sub>2</sub>-BSFs, PDs, and PSFs. The CL maps with high spatial resolution clearly identify the types of the defects and visualize their distribution at a glance. In chapter 3.3, it was directly observed and demonstrated that the anisotropic luminescence characteristics of the semi-polar (11 $\bar{2}$ 2) InGaN/GaN MQWs located underneath the surface undulation. Chapter 3.3 shows the luminescence of the excitonic states in a mechanically exfoliated few-layer MoS<sub>2</sub>.

At the conclusion, chapter 4 summarized this thesis.



### 1. 3. Bibliography

1. Petrov, V. *Physics-Uspekhi* **1996**, 39, (8), 807-818.
2. Yacobi, B. G.; Holt, D. B., *Cathodoluminescence microscopy of inorganic solids*. Springer Science & Business Media: 2013.
3. Yacobi, B. G.; Holt, D. B., *Cathodoluminescence microscopy of inorganic solids*. Plenum Press: New York, 1990; p ix, 292 pages.
4. Petrov, V. I. *Phys Usp* **1996**, 39, (8), 807.
5. Mitdank, R.; Sveshnikova, A.; Schulze, E.; Oelgart, G.; Reinhart, F.-K. *Semicond Sci Technol* **1995**, 10, 835.
6. Schmidt, G.; Veit, P.; Berger, C.; Bertram, F.; Dadgar, A.; Strittmatter, A.; Christen, J. *Japanese Journal of Applied Physics* **2016**, 55, (5S), 05FF04.
7. Griffiths, J. T.; Zhang, S.; Rouet-Leduc, B.; Fu, W. Y.; Bao, A.; Zhu, D.; Wallis, D. J.; Howkins, A.; Boyd, I.; Stowe, D. *Nano letters* **2015**, 15, (11), 7639-7643.
8. Zagonel, L. F.; Mazzucco, S.; Tence, M.; March, K.; Bernard, R.; Laslier, B.; Jacopin, G.; Tchernycheva, M.; Rigutti, L.; Julien, F. H.; Songmuang, R.; Kociak, M. *Nano Lett* **2011**, 11, (2), 568-73.
9. Urban, A.; Müller, M.; Karbaum, C.; Schmidt, G.; Veit, P.; Malindretos, J.; Bertram, F.; Christen, J.; Rizzi, A. *Nano letters* **2015**, 15, (8), 5105-5109.
10. Zhou, X.; Lu, M.-Y.; Lu, Y.-J.; Jones, E. J.; Gwo, S.; Gradecak, S. *ACS nano* **2015**, 9, (3), 2868-2875.

## **Chapter 2. PART I: Development of a novel CL stage with retractable light-collecting optics for TEM**

### **2. 1. Introduction**

Cathodoluminescence (CL) is an optical and electrical phenomenon arising from interactions between accelerated electrons and materials. When the highly energetic electrons exposed on a luminescent material, the primary electrons excite the electrons in the matter, and the excited electrons release its excess energy as photons in accordance with their internal transitions. Thus, CL spectroscopy provides invaluable information on electronic structure such as bandgap energy, excitonic states, impurity-, and dopant-levels.<sup>1, 2</sup>

There have been many efforts to combine the CL spectroscopy with an electron microscope. In the early stage of the CL system development, it was connected with scanning electron microscope (SEM).<sup>3-5</sup> SEM-CL was easy to install, but spatial resolution was poor because of large electron-beam interaction volume within a sample. After then, a CL system established in a transmission electron microscope (TEM) was reported.<sup>6, 7</sup> Nowadays, thanks to recent progress in developing TEM-CL system, CL analysis technique have unveiled quantum-optical properties of nano materials, such as quantum dot,<sup>8</sup> quantum well,<sup>9</sup> quantum disk,<sup>10</sup> nanorods<sup>11</sup> and nanodisks<sup>12</sup>. Moreover, recently, CL analysis has attracted great interest to understand surface plasmon resonance in nanostructured metals.<sup>13-</sup>

<sup>16</sup>

In spite of these outstanding performances, however, a small number of custom-made and commercially supplied TEM-CL systems have been installed in worldwide. Because it is difficult and exclusive technique to fabricate light-collecting optics in a very limited space between pole-pieces of TEM, and in sometimes, the column need to be modified for CL acquisition.

There are two types of TEM-CL system. One is a dedicated CL system,

which has an embedded light-collecting optics in the column of TEM. Custom-made systems with a half-parabolic mirror<sup>17,18</sup> and a parabolic mirror<sup>19</sup> were reported. Last year, commercial product equipped with a fully motorized mirror was released (Attolight, Switzerland). The other one is a portable CL system, which has an integrated light-collecting optics in a TEM holder. Our previous CL setup<sup>20</sup> and recently released commercial CL system (Gatan, Inc., USA) based on this simple holder concept, which is compatible for standard TEM without remodeling of your own system.

Figure 2.1.1 is a schematic diagram of the interaction between electron beam and specimen in our CL system. The specimen is fitted into a slit of a miniaturized reflecting mirror and then a parabolic shaped inner surface of the mirror is covering the whole specimen except the region of small aperture for electron beam transmission. Although this design ensures high light-collection efficiency, the fixed mirror causes two problems. First, an observable area is reduced from whole grid ( $\Phi = 3$  mm) to the small aperture on the mirror ( $\Phi = 0.4$  mm), and it is time and effort consuming task to align the region of interest to the position of the aperture. Second, it is unable to analysis energy-dispersive spectroscopy (EDS) because the mirror blocks the escape of the characteristic X-ray signal from the specimen. Since there are transmitted electrons, we can still acquire electron energy-loss spectroscopy (EELS) for chemical analysis but EDS and EELS are complementary techniques to understand your specimen thoroughly.

In this study, I report a design and fabrication of a CL holder equipped with a retractable light-collecting optics. The movable optics integrated on the head part of the holder enable us to achieve large observation area and to acquire characteristic X-ray signal. This novel TEM-CL stage can provide structural-, optical-, and chemical-analysis platform beyond the limitations of conventional CL system with stationary optics.

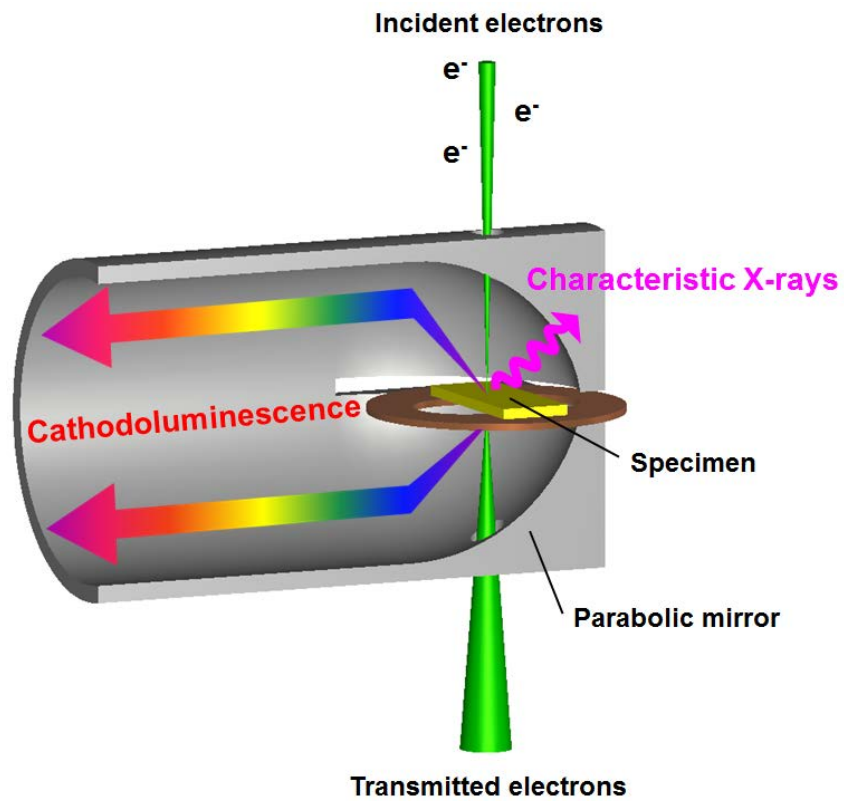


Figure 2.1.1. An electron beam-specimen interaction in general TEM-CL stage with a parabolic mirror

## 2. 2. Experimental details

The newly invented TEM-CL stage provides three functions, i.e., collection and transportation of light, retractability of the reflecting mirror, and cooling capability of the specimen stage. Implementation details of each function are presented in consecutive order.

### (1) Collection and transportation of the light

Figure 2.1.2 (a) shows a design of the TEM-CL stage and inset of Figure 2.1.2 (a) is an enlarged image of the head part of the CL stage. The overall dimensions of the stage are satisfying specifications for JEOL-TEM equipped with high-resolution pole-pieces. A light collecting module on the head part of the stage is mainly composed of a reflecting mirror, a focusing lens, and an optical fiber. Among them, the design of mirror is most important process for implementing high collection efficiency, because it firstly reflects the CL signal, which is weak and emitted in any direction. The mirror is made of aluminum to ensure high reflectance in wide range of wavelengths and an inner surface of the mirror is shaped in parabolic to provide an omnidirectional reflector. A through hole ( $\Phi=0.4$  mm) for transmission of electrons is placed at the focal length of the parabola and an entrance slit for specimen insertion is located at front side of the mirror. The dimensions of each feature are determined to minimize optical losses.

The convex-type focusing lens (SIGMA KOKI CO., LTD., Japan) is attached on the exit of the mirror, while keeping the distance between the lens and the focal point of the parabolic inner surface at the focal length of the lens (6 mm). The front face of the optical fiber (Ocean Optics, Inc., USA) is also located at a distance from the other side of the lens. The numerical aperture of the fiber is 0.22 and the diameter of the fiber core is 1000  $\mu\text{m}$ . It can transport the light from ultra-violet (UV) to visible (VIS) range. The whole body of the fiber, excepting the front face, is covered with an aluminum jacket to protect the fiber core from an external mechanical and thermal shock. The optical fiber and the mirror are connected through sapphire fixture rods and a small aluminum block.

When a specimen is fitted into the slit of a mirror, as a result, the CL

signal from the specimen is reflected on the inner surface of the mirror and directed toward the optical fiber through the biconvex lens. The optical fiber guided the light to a vacuum feedthrough, which is coupled with a spectrometer in air.

## (2) Retractability of the reflecting mirror

A stretchable bellows was applied to move the light collection module, as shown in Figure 2.1.2 (a) and 2.1.2 (d). One side of the bellows is welded to fixed heavy parts, i.e., a handle of the stage connected with a liquid nitrogen dewar, and the other side of the bellows is bonded to a support plate, which is carrying the vacuum feedthrough of the optical fiber and is attached on a linear stage. As we adjust a micrometer of the linear stage, the bellows is expanded or contracted, resulting in an axial advance or a retraction of the fiber accompanied with the light collection module. At this time, the expansion direction of the bellows is designed to against vacuum pressure. Otherwise, the expansion force of the bellows cannot overcome the pulling force of vacuum.

Figure 2.1.2 (b), (c), (e), and (f) show the retraction of the light collection module on the head part of the stage. On closed position, the specimen is covered with the reflecting mirror for CL signal collection. After retracting the assembly, the characteristic X-ray signal from the specimen escape outward. By moving the whole assembly, we can easily maintain the alignment and the spacing of the optics. For accurate linear motion, a pair of ruby guide rail is placed on the both inner sidewall of the stage and the sapphire fixture rods are touched with it to minimize the error of linear movement due to friction. In addition, a pair of sapphire alignment pins is present on both sides of the specimen to guide the insertion of the mirror at exact position.

## (3) Cooling capability of the specimen stage

A cryostat is built on the TEM-CL stage for reducing electron-beam damage and acquiring high CL intensity with high spatial resolution. Liquid nitrogen dewar is attached on the handle of the stage, and a cold finger on the bottom of the dewar is coupled with oxygen-free high-purity copper (OFHC) tube covering the optical fiber. The front part of the copper tube is connected with the

head part of the stage, thus the specimen can be cool down. In order to read-out the temperature, a K-type thermocouple is attached on the cold head and wired to an electrical feedthrough. To prevent thermal loss, the holder body is isolated from the cold head through an engineering plastic part. The movable assembly, i.e., light collection module, is also separated from the cold head through minimum contact between the sapphire fixture rod and the ruby guide rail.

Figure 2.1.3 is a photograph of a whole TEM-CL system. The TEM-CL stage is inserted to the specimen chamber of the TEM equipped with field emission gun (JEM-2010F, JEOL, Japan). An optical fiber from the CL stage is connected to the spectrometer (Shamrock 163, Andor Technology PLC, Belfast, UK) with electron multiplying charge-coupled device (Newton EMCCD, Andor Technology PLC, Belfast, UK), and the output of the EMCCD is transported to the data PC. Custom-made CL acquisition and analyzing software enables us to acquire point spectra, hyperspectral maps, monochromatic maps, and panchromatic maps. I used a beam control unit (SEMISTEM, Oxford instruments, UK) for scanning the electron beam and EDS detector (6498, Oxford instruments, UK) for acquiring characteristic X-ray signal.

Figure 2.1.4 shows sequential TEM images during a retraction of the mirror. At the position for CL signal collection (Fig. 2.1.4 (a)), a mesh grid is covered with the reflecting mirror except the through hole for electron transmission. As adjusting the micrometer of the linear stage, the mirror is moving downward, and the edge of the mirror is appeared (Fig. 2.1.4 (b) and Fig. 2.1.4 (c)). After removing the mirror on the field of view (Fig. 2.1.4 (d)), the specimen is ready for EDS measuring.

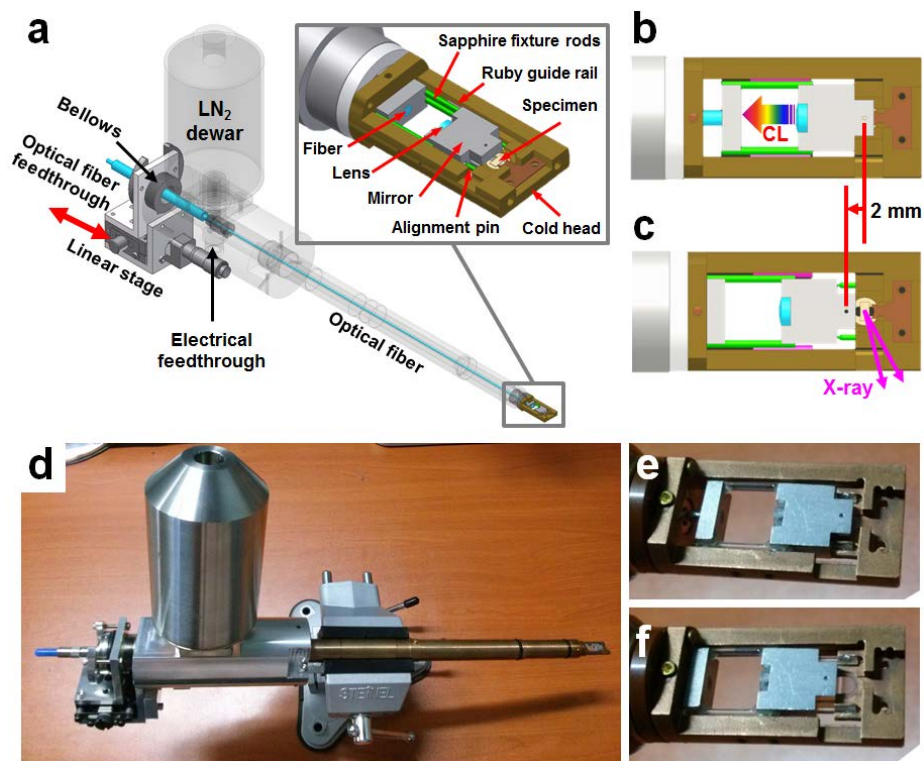


Figure 2.1.2. Design and fabrication of CL stage with a retractable mirror: (a, d) overall appearance of CL stage, (b, e) head part with locating the mirror at a closed position for CL signal collection, (c, f) head part with locating the mirror at an opened position for characteristic X-ray signal collection (c, f).



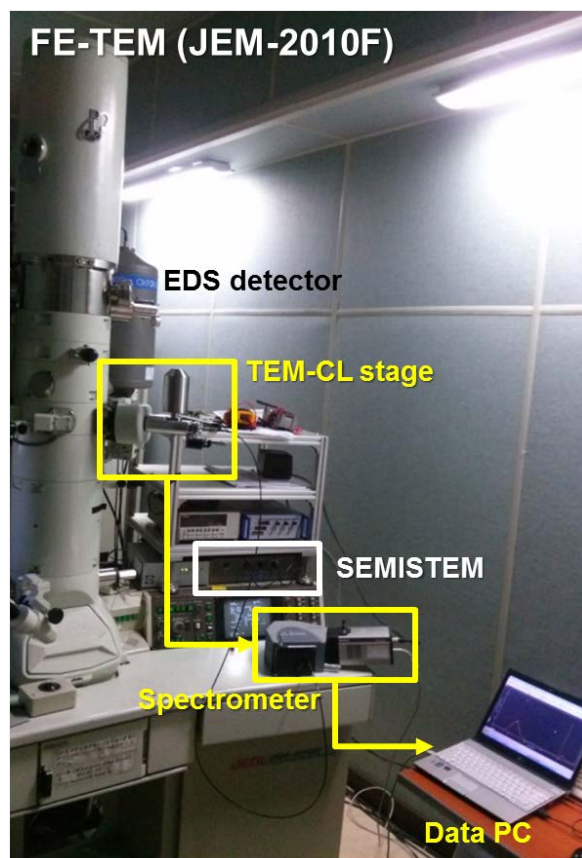


Figure 2.1.3. A photograph of a whole TEM-CL acquisition system

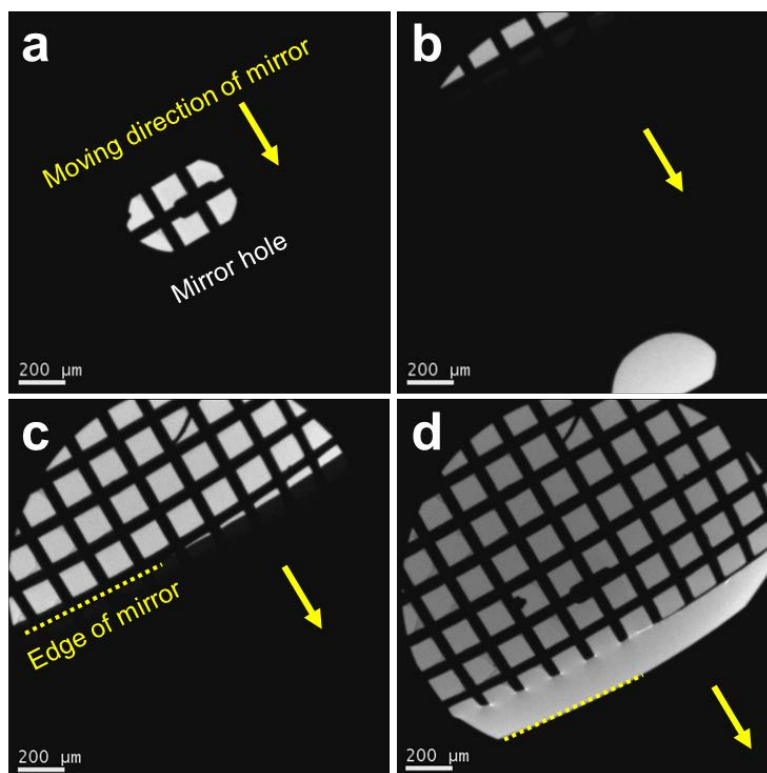


Figure 2.1.4. Sequential TEM images during a retraction of the mirror: (a) at a position for CL signal collection, (b, c) at intermediate positions (d) at a position for characteristic X-ray signal collection.

## 2. 3. Results and discussions

Performance and stability of the TEM-CL stage was tested on zinc oxide (ZnO) nanowires. ZnO nanowires has been widely studied for nanoscale electronic and optoelectronic devices<sup>21-23</sup> thanks to its nature of wide bandgap ( $E_g \sim 3.3$  eV) and large binding energy of exciton (60 meV) at room temperature.<sup>24</sup> In our experiments, the nanowires were synthesized via conventional vapour–liquid–solid (VLS) process using Au deposited Si substrates.<sup>25</sup> For TEM sample preparation, the substrate with ZnO nanowire is immersed in isopropyl alcohol (IPA) and subjected to ultrasonic treatment. After that, several drops of the dispersion are placed on a perforated carbon film supported by Cu mesh grid.

Figure 2.1.5 represents test results of cooling capability of the CL stage. As shown in Figure 2.1.5 (a), after pouring LN<sub>2</sub> into the dewar, the temperature of the cold head decreased and saturated at -127 °C after 40 minutes. The saturated temperature was maintained for 3 hours with  $\pm 1$  °C oscillation. Figure 2.1.5 (b) shows point CL spectra of ZnO nanowire before and after the stage cooling. In order to minimize electron beam induced damage, each CL spectrum was acquired on a fresh nanowire with low electron-beam acceleration voltage of 120 kV. The inset figures indicate the position of the electron beam on each measured nanowire. Two characteristic peaks are observed in both spectra. One is strong and sharp emission peak around 370 nm corresponding to UV emission due to near band-edge transition, and the other one is broad and weak emission peak around 550 nm referring to green emission caused by defect states related transition.<sup>26</sup> After cooling of the stage, the intensity of the UV emission extremely increased and the peak wavelength is slightly move to short wavelength due to release of temperature induced band-gap shrinkage.<sup>27</sup>

Figure 2.1.6 shows successive acquisitions of CL and EDS signal on same position of a ZnO nanowire. The experiment steps are as follows: first, the reflecting mirror is placed on the grid (Inset of Figure 2.1.6 (b)). TEM image and CL signal of a target nanowire were obtained through the electron beam hole

(Figure 2.1.6 (a) and Figure 2.1.6 (b)); second, for securing the exit of characteristic X-ray signals, the mirror is retracted as adjusting the micrometer on the linear stage until the mirror is completely removed from the nanowire (Inset of Figure 2.1.6 (c)); third, a clamp of the linear stage is locked to fix the position of the mirror; last, EDS signal is obtained and analyzed on the target nanowire (Figure 2.1.6 (c)). In addition, successive acquisitions of CL and EDS map can be achieved in the same procedure as described above. Figure 2.1.7 presents bright field image of ZnO nanowires (Figure 2.1.7 (a)), CL intensity map integrated from 375 nm to 385 nm (Figure 2.1.7 (b)), elemental map of Zn-K $\alpha$  (Figure 2.1.7 (c)) and O-K $\alpha$  (Figure 2.1.7 (d)). Based on the test results of ZnO nanowires, it was confirmed that the cooling capability of the TEM-CL stage and successive acquisition of CL and EDS signal. When the mirror is inserted or retracted, however, there is an unavoidable small change of position because manually controlled linear stage was used.

In conclusion, I developed a novel TEM-CL holder with a retractable light-collecting optics, which is composed of miniaturized optical components and integrated on head part of the holder. By moving the whole optics isolated from built-in cryostat, I obtain large CL observation area and successive measurement of EDS signal while maintaining accurate alignment of the optics. Performance and applicability of the system were successfully demonstrated by analyzing ZnO nanowires. I believe that this remarkable TEM-CL stage, which is portable and compatible with a commercial TEM, provides easy interface for users and opens a new horizon for hybrid analysis system including structural-, optical-, and chemical-analysis.

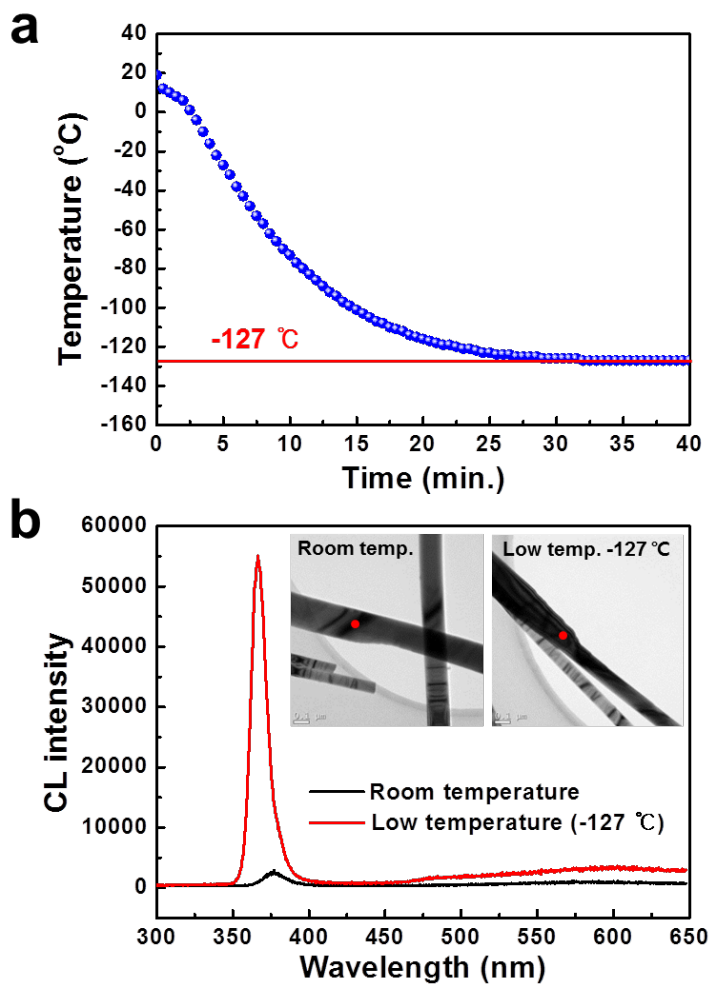


Figure 2.1.5. Collection of CL signals under low-temperature: (a) Temperature change of the CL stage after pouring liquid nitrogen into the dewar (b) CL point spectra of ZnO nanowires before and after CL stage cooling. The inset figures in (b) represent the position of an electron beam with red spots.

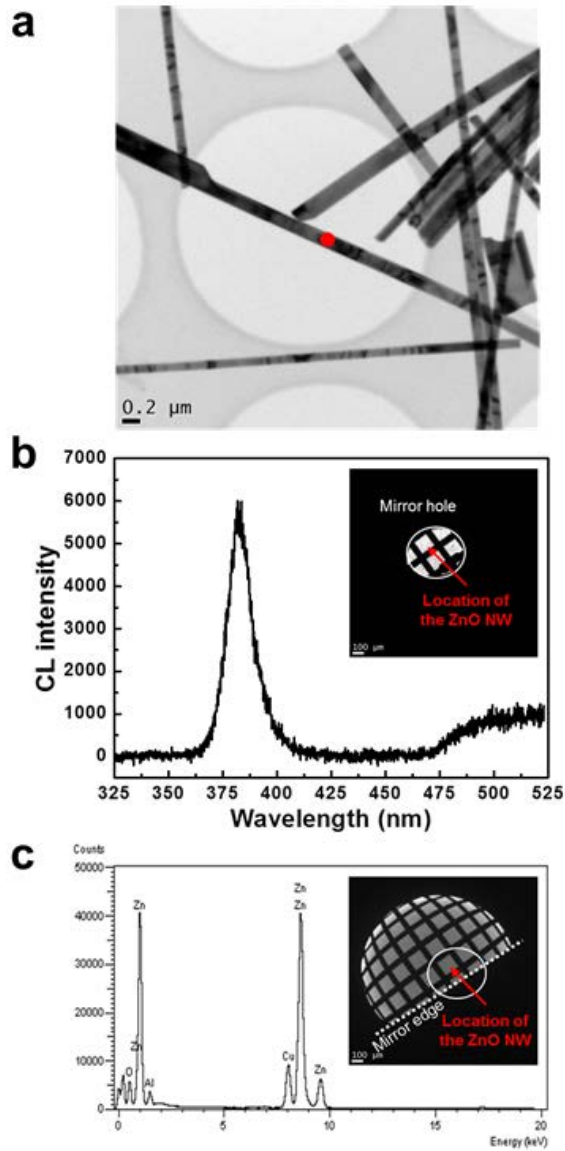


Figure 2.1.6. Successive acquisition of a CL and an EDS signal: (a) TEM bright field image of ZnO nanowires. A red spot indicates a position of an electron beam (b) CL point spectrum (c) EDS point spectrum. The inset figures of (b) and (c) show the position of the mirror at each measurement.

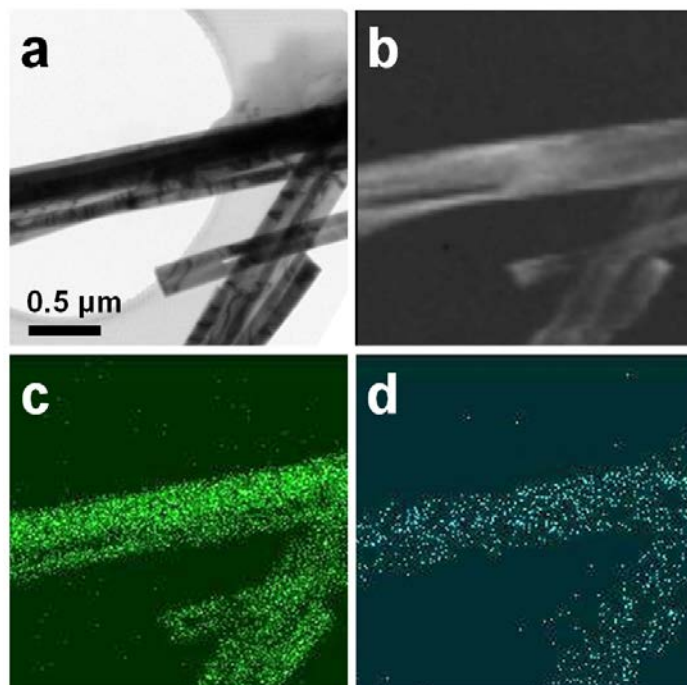


Figure 2.1.7. Successive acquisition of the CL and EDS map of ZnO nanowires: (a) TEM bright field image (b) CL intensity map ( $\lambda$ : 375–385 nm) (c) EDS map of Zn-K $\alpha$  (d) EDS map of O-K $\alpha$

## 2. 4. Bibliography

1. Petrov, V. *Physics-Uspekhi* **1996**, 39, (8), 807-818.
2. Yacobi, B. G.; Holt, D. B., *Cathodoluminescence microscopy of inorganic solids*. Springer Science & Business Media: 2013.
3. Davidson, S.; Rasul, A. *Journal of Physics E: Scientific Instruments* **1977**, 10, (1), 43.
4. Giles, P. *JOURNAL DE MICROSCOPIE ET DE BIOLOGIE CELLULAIRE* **1975**, 22, (2-3), 357-369.
5. Steyn, J.; Holt, D. *Journal of Microscopy* **1976**, 107, (2), 107-128.
6. Pennycook, S.; Brown, L.; Craven, A. *Philosophical magazine A* **1980**, 41, (4), 589-600.
7. Petroff, P.; Lang, D. *Applied Physics Letters* **1977**, 31, (2), 60-62.
8. Schmidt, G.; Veit, P.; Berger, C.; Bertram, F.; Dadgar, A.; Strittmatter, A.; Christen, J. *Japanese Journal of Applied Physics* **2016**, 55, (5S), 05FF04.
9. Griffiths, J. T.; Zhang, S.; Rouet-Leduc, B.; Fu, W. Y.; Bao, A.; Zhu, D.; Wallis, D. J.; Howkins, A.; Boyd, I.; Stowe, D. *Nano letters* **2015**, 15, (11), 7639-7643.
10. Zagonel, L. F.; Mazzucco, S.; Tence, M.; March, K.; Bernard, R.; Laslier, B.; Jacopin, G.; Tchernycheva, M.; Rigutti, L.; Julien, F. H.; Songmuang, R.; Kociak, M. *Nano Lett* **2011**, 11, (2), 568-73.
11. Urban, A.; Müller, M.; Karbaum, C.; Schmidt, G.; Veit, P.; Malindretos, J.; Bertram, F.; Christen, J.; Rizzi, A. *Nano letters* **2015**, 15, (8), 5105-5109.
12. Zhou, X.; Lu, M.-Y.; Lu, Y.-J.; Jones, E. J.; Gwo, S.; Gradecak, S. *ACS nano* **2015**, 9, (3), 2868-2875.
13. Kawasaki, N.; Meuret, S.; Weil, R.; Lourenço-Martins, H.; Stéphan, O.; Kociak, M. *ACS Photonics* **2016**, 3, (9), 1654-1661.
14. Losquin, A.; Zagonel, L. F.; Myroshnychenko, V.; Rodríguez- González, B.; Tencé, M.; Scarabelli, L.; Förstner, J.; Liz-Marzán, L. M.; García de Abajo, F. J.; Stéphan, O. *Nano letters* **2015**, 15, (2), 1229-1237.



15. Yamamoto, N.; de Abajo, F. J. G.; Myroshnychenko, V. *Physical Review B* **2015**, 91, (12), 125144.
16. Zhao, M.; Bosman, M.; Danesh, M.; Zeng, M.; Song, P.; Darma, Y.; Rusydi, A.; Lin, H.; Qiu, C.-W.; Loh, K. P. *Nano letters* **2015**, 15, (12), 8331-8335.
17. Kociak, M.; de Abajo, J. G. *MRS bulletin* **2012**, 37, (01), 39-46.
18. Strunk, H.; Albrecht, M.; Scheel, H. *Journal of microscopy* **2006**, 224, (1), 79-85.
19. Yamamoto, N. *Microscopy* **2016**.
20. Sheen, M.-H.; Kim, S.-D.; Lee, J.-H.; Shim, J.-I.; Kim, Y.-W. *Journal of Electronic Materials* **2015**, 44, (11), 4134-4138.
21. Jean, J.; Chang, S.; Brown, P. R.; Cheng, J. J.; Rekemeyer, P. H.; Bawendi, M. G.; Gradečak, S.; Bulović, V. *Advanced Materials* **2013**, 25, (20), 2789-2789.
22. Liu, X.; Gu, L.; Zhang, Q.; Wu, J.; Long, Y.; Fan, Z. *Nature communications* **2014**, 5.
23. McCune, M.; Zhang, W.; Deng, Y. *Nano letters* **2012**, 12, (7), 3656-3662.
24. Özgür, Ü.; Alivov, Y. I.; Liu, C.; Teke, A.; Reshchikov, M.; Doğan, S.; Avrutin, V.; Cho, S.-J.; Morkoc, H. *Journal of applied physics* **2005**, 98, (4), 041301.
25. Huang, M. H.; Wu, Y.; Feick, H.; Tran, N.; Weber, E.; Yang, P. *Advanced Materials* **2001**, 13, (2), 113-116.
26. Huang, Z.; Chai, C.; Cao, B. *Crystal Growth & Design* **2007**, 7, (9), 1686-1689.
27. Cao, B.; Cai, W.; Zeng, H. *Applied physics letters* **2006**, 88, (16), 161101-161101.

## **Chapter 3. PART II: Applications of the TEM-CL technique to semiconductor research**

### **3. 1. Role of V-pits as a diffusion barrier for carriers in polar InGaN/GaN quantum wells**

#### **3. 1. 1. Introduction**

In<sub>x</sub>Ga<sub>1-x</sub>N/GaN quantum well (QW) structures fabricated by an hetero-epitaxial growth suffered from high dislocation density due to the large lattice mismatch between the substrates and the GaN thin film. Despite the high threading dislocation (TDs) density, In<sub>x</sub>Ga<sub>1-x</sub>N/GaN hetero-structures shows high electroluminescence efficiency, which has been explained by exciton localization<sup>1</sup> and V-pit formation.<sup>2</sup> The V-pit, a typical defect found in InGaN/GaN QW structures, is an open inverted hexagonal pyramid shaped defect, which originates from differences in the surface diffusion of Ga atoms at low growth temperatures. Recently, it was reported that the high potential barrier due to {10 $\bar{1}$ 1}-faceted QWs in the V-pit could prevent carriers from drifting towards TDs known as non-radiative recombination centers (NRCs).<sup>2-5</sup> In addition, the *p*-GaN layer filling the V-pits provides an alternative conductive pathway, and enhance an injection of holes into the QWs.<sup>6</sup> Therefore, the interference of the charge carrier transport due to the V-pits is important in the extraordinary emission efficiency of light emitting diodes (LEDs) at room temperature.<sup>7,8,9</sup>

Microstructures and their optical properties are closely correlated in III-nitride systems, and have been popular research topics for developing the high-efficiency devices. There has been debates about the existence of {10 $\bar{1}$ 1}-faceted QWs in the V-pit,<sup>10,11</sup> and the emission wavelength of the semipolar QWs is shorter<sup>12</sup> or longer<sup>13, 14</sup> than that of the {0001}-plane QWs.

Many research groups have been reported on the luminescence characteristics of the V-pits, using low-temperature photoluminescence,<sup>3,15</sup> low-temperature electroluminescence<sup>16</sup> and near-field scanning optical microscopy.<sup>4</sup> The relationships between the microstructure and optical properties were difficult to visualize in systems using optical probes, due to limitations of spatial resolution. The luminescence characteristics of the V-pits have also been investigated by using scanning electron microscopy (SEM) combined with cathodoluminescence (CL), taking advantage of high-spatial-resolution microscope images associated with simultaneous emission map of the same observation region.<sup>17,18</sup> However, the SEM can only observe surface structures because it collects secondary electrons (SEs) emitted from surface. The V-pits are, unfortunately, hidden under the surface more than several tens of nanometers thick. In order to observe the hidden V-pit structure, and to correlate it with optical properties, intentionally exposed V-pit samples have to be prepared to locate the target area within the escape depth of the SEs. By using the SEM-CL, optical properties of the V-pits were reported;<sup>5, 14</sup> however, extra consideration is necessary owing to the deviation from the operational LEDs with the top p-GaN layer. Moreover, the large electron-beam interaction volume reduces the spatial resolution of CL. Therefore, it still remained unclear how the microstructure of the V-pits influence on their optical properties

Here, high-resolution, position-specific luminescence maps of the V-pits were obtained using transmission electron microscopy (TEM) equipped with CL. It clearly identify the role of the V-pit in commercial LED devices. Distributions of emission wavelengths were superimposed on the high-resolution internal microstructural images, which clearly show the optical properties of each region of the V-pit, i.e., TD,  $\{10\bar{1}1\}$ -faceted QWs, and C-plane QWs. Furthermore, remarkable optical behavior of a V-pit corner, i.e., the  $\{10\bar{1}1\}$ -plane to C-plane transition zone, is observed and discussed.

### 3. 1. 2. Experimental details

A commercial LED chip (CREE, USA) was used to examine the optical properties of the V-pits. TEM specimens were prepared with a mechanical polishing and an ion milling (PIPS, Gatan) using 3 kV  $\text{Ar}^+$  ions for 30 minutes. The active region of the LED was consisted of eight pairs of  $\text{In}_{0.15}\text{Ga}_{0.85}\text{N}$  (3.5 nm)/GaN (9 nm) QWs and a 40-nm-thick AlGaN electron blocking layer, capped with a 220-nm-thick p-GaN layer.

The CL spectra and maps of the LED specimens were acquired by using a home-built CL stage with TEM (JEM-2010F, JEOL, Japan). A low-acceleration electron beam voltage (120 kV) was used to reduce radiation damage, and to increase the cross-section of carrier recombination. The CL signal, emitted from the specimen stimulated with the energetic electron beam, was reflected by a mirror and focused through a lens on the optical fiber. The fiber was coupled to a spectrometer with a  $600\text{ mm}^{-1}$  groove density grating. The spectrum range was 280 to 520 nm, with a 0.37 nm spectral resolution. The specimen was cooled to 137K to improve the exciton recombination rate and to reduce diffusion length of carriers. Point-to-point mapping was obtained by scanning a  $2 \times 2\text{ }\mu\text{m}$  area with a pixel size of  $\sim 15\text{ nm}$ . Panchromatic, monochromatic, and hyperspectral mapping of the collected wavelength spectra was processed with a custom made Java software. We used a JEM-2100F scanning transmission electron microscope (STEM) to acquire high-resolution (HR) and annular dark-field (ADF) images.

### 3. 1. 3. Results and discussions

Figure 3.1.1(c) is a schematic diagram of an LED specimen structure which contains a V-shaped pit in the InGaN/GaN QW structure. One pair of InGaN/GaN QWs is represented in the schematic diagram for simplicity. The p-type GaN and AlGaIn layers are also omitted to expose the surface of the semipolar QWs. As shown in the model, the V-pit has a TD core with surrounding semipolar  $\{10\bar{1}1\}$  planes, similar to an inverted cone with six planes. The QWs were expected to form on the revealed surfaces of the thin film when InGaN QWs were grown on the n-type GaN, which has exposed surfaces of the both  $\{0001\}$  C-plane and  $\{10\bar{1}1\}$  semi-polar plane on the side-walls of the V-pits, but the QW thicknesses may change due to the differences in diffusion coefficients.

Figure 3.1.1 (a) and (b) show a cross-section view and a plan-view TEM image of the LED specimen, which contain the layers of p-GaN, InGaN/GaN QWs, and a portion of n-GaN along the viewing direction, i.e., the  $\{0001\}$ -growth direction. The bright field image accompanied with selected area diffraction (SAD) patterns confirms that the V-pits were projected along  $\{0001\}$ , and each side of the hexagon corresponds to the intersections of the  $\{0001\}$  and  $\{10\bar{1}1\}$  planes. The density of the V-pits was approximately  $1.1 \times 10^9/\text{cm}^2$ , and each V-pit had a TDs at the center.

Figure 3.1.2 (a) is a cross-sectional ADF image of a V-pit showing the penetrating TD at the center and the symmetric  $\{10\bar{1}1\}$ -faceted QWs around the dislocation. The white arrows labeled A through D indicate the TD core,  $\{10\bar{1}1\}$ -faceted QWs, V-pit corner, and C-plane QWs, respectively. A hyperspectral map was obtained along the white dotted line in Fig. 3.1.2 (a) to visualize the spatial distribution of spectra, which is shown in Figure 3.1.2 (b). The hyperspectral map shows that the  $\{10\bar{1}1\}$ -faceted QWs (B) emit strongly blue-shifted emission when compared to the C-plane QWs (D). Weak emission intensities were observed at the TD core (A) and V-pit corner (C). Figure 3.1.2(c) shows the CL point spectra from four regions as shown in Figure 3.1.2(a) and (b). The  $\{10\bar{1}1\}$ -faceted QWs emits

photons with wavelengths of about 385 nm, which corresponds to the ultraviolet region and is close to the GaN near-band-edge emission.<sup>19</sup> The wavelength of the emission from  $\{10\bar{1}1\}$ -faceted QWs was much shorter than that from the C-plane InGaN QWs. The strongly blue-shifted emission from  $\{10\bar{1}1\}$ -faceted QWs is mainly caused by thin thickness of the QW, which can be seen clearly in the ADF image of Figure 3.1.2 (a) with two different thickness of C-plane and  $\{10\bar{1}1\}$ -faceted QWs. The TD core region exhibited weak emission centered around 380 nm, which is close to the emission wavelength from the  $\{10\bar{1}1\}$ -faceted QW. The TD core acts like an NRCs, but a portion the QW emission was detected, which might be detected from the adjacent  $\{10\bar{1}1\}$ -faceted, incorporated into the TD core region due to carrier diffusion. The V-pit corner, joining region of the C- and  $\{10\bar{1}1\}$ -planes, showed a weak CL intensity.

From the CL point spectra, monochromatic wavelength maps were extracted and correlated it with the microstructure (Fig. 3.1.3). Figure 3.1.3 (f) shows a composite image of luminescence from the C- and  $\{10\bar{1}1\}$ -faceted QW emissions, shown in red for 460–490 nm and in green for 370–390 nm. The luminescence image is superimposed on the Z-contrast image of the V-pit to associate the position-sensitive luminescence properties. The combined image clearly reveals no emission in the V-pit corner or the TD core. While it is well known that TDs behave as NRCs, dead luminescence from V-pit corners has not been reported yet, and is only possible to observe via high-resolution mapping of CL.

The origin of dead emission from the V-pit corner was analyzed by using high-resolution transmission electron microscopy (HR-TEM). Samples were prepared carefully for HR-TEM by removing an unwanted volume from the CL-mapped specimen, with the result shown in Figure 3.1.3 (g). Two different thicknesses are clearly observed in the  $\{10\bar{1}1\}$ - and C-plane QWs and discontinuities are seen at the V-pit corner. The low indium content at the V-pit corner resulted in a greater potential barrier than that of the surrounding QWs. The carriers generated at the V-pit corner preferentially escape to the adjacent InGaN

QWs, which have lower potential energies and high indium concentration. Therefore, the origin of dead emission at the V-pit corner can be explained by the suppression of carrier recombination due to the high potential barrier caused by the lack of indium contents.

Luminescence from the V-pits was investigated in plan-view specimens, to confirm the distribution of wavelengths. Figure 3.1.4 shows CL mapping results accompanied with their CL point spectra. Figure 3.1.4 (a) represents a CL map from  $\{10\bar{1}1\}$ -faceted QWs (370-390 nm) and Figure 3.1.4 (b) and Figure 3.1.4 (c) show CL maps from C-plane QWs. The emission of C-plane QWs has slightly different peak wavelengths. Figure 3.1.4 (b) shows a map of the satellite emission (460-475 nm) of C-plane QWs and Figure 3.1.4 (c) is an image of residual radiation (475-490 nm), obtained by subtracting the excess emission from the C-plane QW luminescence window (460-490 nm). Figure 3.1.4 (d) shows a color-coded composite CL map of the  $\{10\bar{1}1\}$ -faceted QWs and the satellite emission of C-plane QWs displayed in green and red, respectively. The combined color image clearly shows four different luminescence characteristics as the positions were moved from the center to the outside of the V-pit. (A) indicates the dark spot at the center of the V-pit, i.e., the position of TD; (B) shows emission from the V-pit sidewall QWs, represented in green; (C) is the dark rim along the periphery of the V-pit, corresponding to the V-pit corner; and (D) is the emission from the C-plane QW shown in red. These observations match the results from the cross-sectional TEM-CL results.

Note that the satellite emission was concentrated mainly near the V-pit (marked “\*”), and the region shows brighter luminescence than the normal, defect-free, C-plane QWs. This phenomenon might be caused by the increments of excess carriers near V-pit corner due to geometrical crystal orientation change, resulting in accumulation of the carriers around V-pit corner. Low diffusivity, from cooling to 137K, and from the low indium concentration at the V-pit corner plays a major role in the high carrier population near its periphery.

It has been proposed, and is generally accepted, that QWs maintain

continuity when the growth planes of InGaN QW changes from  $\{10\bar{1}1\}$  to  $\{0001\}$ .<sup>15</sup> If the QW continuity is preserved, the  $\{10\bar{1}1\}$ -faceted QW potential barrier behaves as a potential barrier for the carriers to diffuse into the NRC at the TD.<sup>2</sup> The high-resolution CL combined with TEM directly demonstrates that indium-deficient regions exist between C-plane QWs and  $\{10\bar{1}1\}$ -faceted QWs. The high potential barrier generated by the indium-deficient region along the perimeter of the hexagonal V-pit may effectively block the diffusion of the carriers towards the TD along the  $\{10\bar{1}1\}$ -faceted QWs.

In summary, the luminescence properties of V-pits were directly correlated with their microstructure using TEM-CL. The luminescence characteristics were analyzed with unprecedented spatial resolution of the cathodoluminescence at near the V-pit, and it was clearly revealed that there was the discontinuity in the luminescence at the corner between  $\{10\bar{1}1\}$ - and C-plane quantum wells. The NRCs occurred by TDs and the strongly blue-shifted emission of  $\{10\bar{1}1\}$ -faceted QWs were confirmed and the V-pit corners were found to be nearly pure GaN. Potential barriers, arise from discontinuous QWs around the hexagonal pit, can effectively block the diffusions of carriers into the  $\{10\bar{1}1\}$ -faceted QWs and TDs, which in turn increases the number of effective carriers contributed to radiative recombination. Therefore, modulation of carrier transport introduced by V-pits, i.e. suppression of non-radiative recombination and enhancement of radiative recombination, can contribute to an increase in the internal quantum efficiency of LEDs.



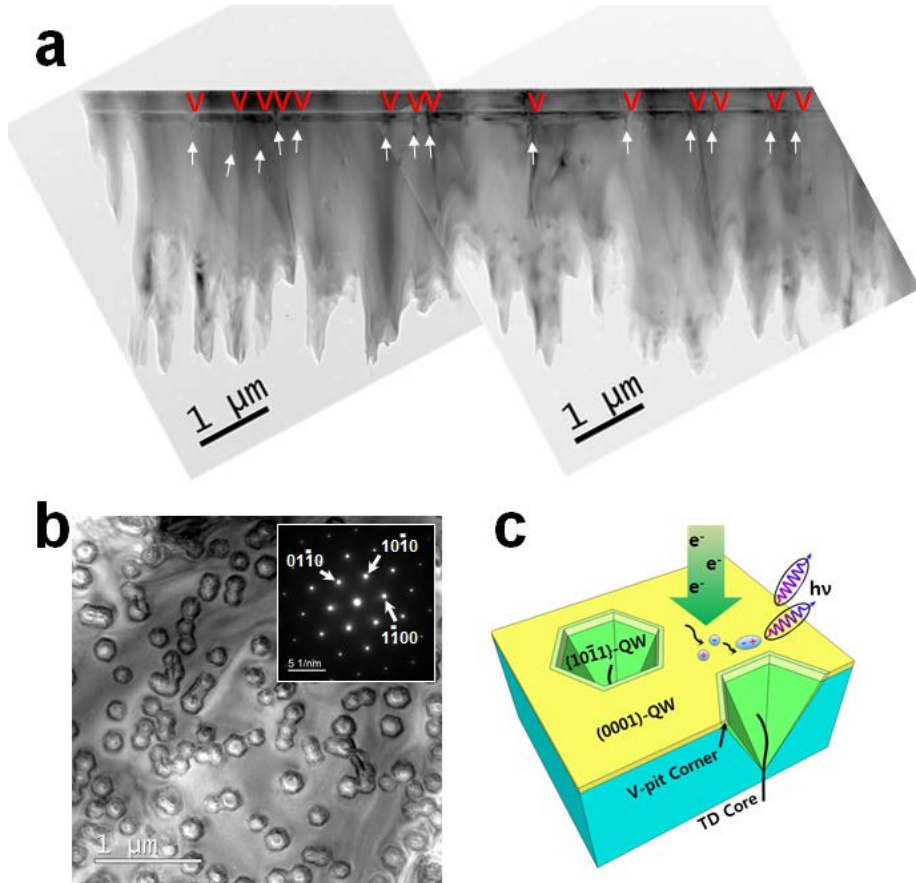


Figure 3.1.1. Bright field TEM images and schematic diagram of an LED specimen. (a) Cross-section view and (b) Plan-view with the selected area diffraction pattern of the same area in the inset. (c) Schematic diagram of the V-pit structure in InGaN/GaN QW.

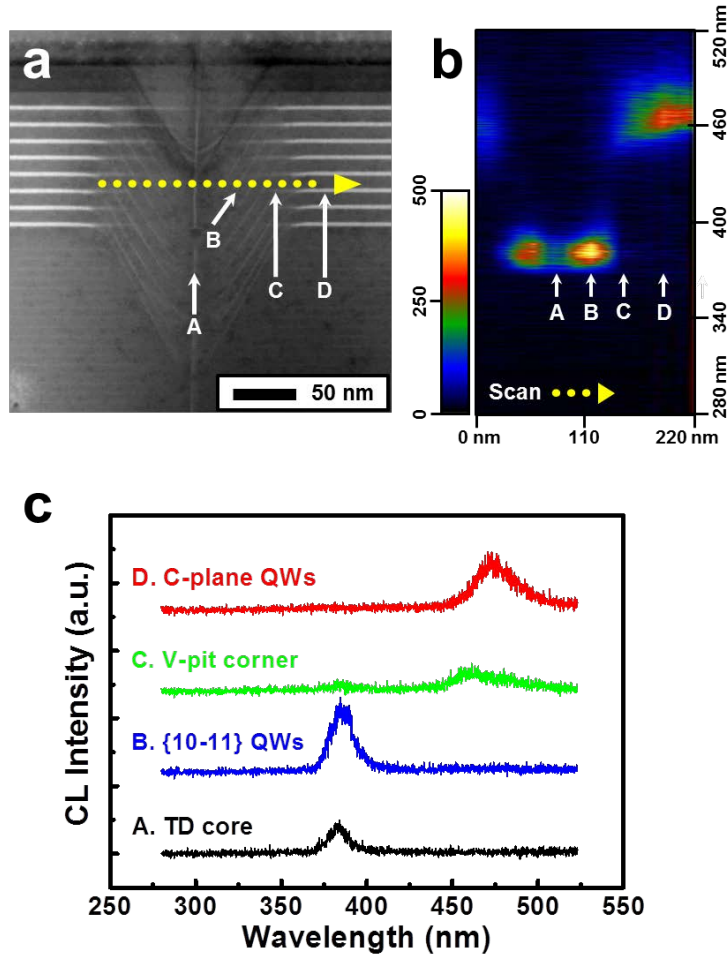


Figure 3.1.2. The luminescence characteristics of the V-pit analyzed by TEM-CL from a cross-sectional LED specimen. (a) STEM-ADF image of the V-pit. Yellow dotted line indicates the position and direction of the CL line scan. White arrows indicate the TD core (A),  $\{10\bar{1}1\}$ -faceted QWs (B), V-pit corner (C), and C-plane QWs (D). (b) Hyperspectral CL map along the yellow dotted line in (a). The  $x$ -axis indicates to the spatial position in the scan line and the  $y$ -axis indicates the wavelength. The relative CL intensity is represented with a color scale from black to white. (c) CL point spectra of the four regions marked with white arrows in (a) and (b).

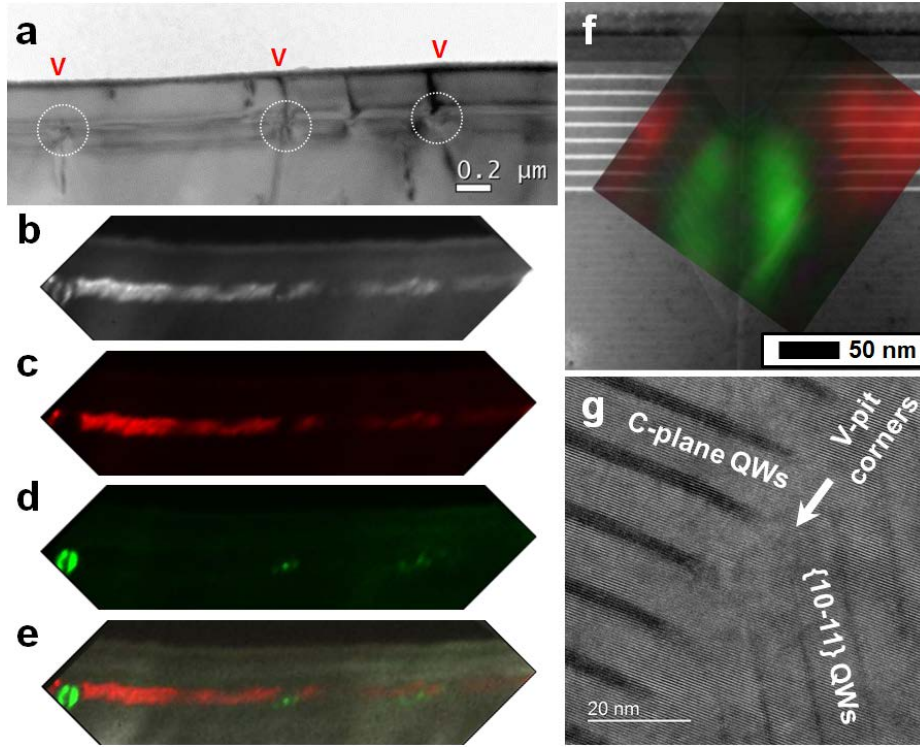


Figure 3.1.3. The optical behaviors of V-shaped pit are analyzed by TEM-CL on cross-sectional LED specimen. (a) Bright field image of the active region shows that the MQWs were affected by the V-shaped pit with white circle. (b) Panchromatic CL map on the same area ( $\lambda$ : 350–500 nm) presented the NRC of TD crossing active regions. Monochromatic CL map of flat MQWs ( $\lambda$ : 460–490 nm) (c) and V-defect sidewall ( $\lambda$ : 370–390 nm) (d). (e) RG composite image (R: flat QWs, G: sidewall QWs). (f) Red-Green composite color CL map of the V-pit overlapped on its STEM image. Red indicates the emission of C-plane QWs ( $\lambda$ : 460–490 nm), and green indicates the emission of  $\{10\bar{1}1\}$ -faceted QWs ( $\lambda$ : 370–390 nm). (g) A high-resolution TEM image of the V-pit corner. The white arrows indicate the positions of the V-pit corners, i.e.,  $\{10\bar{1}1\}$ -plane to C-plane QW transition zone.

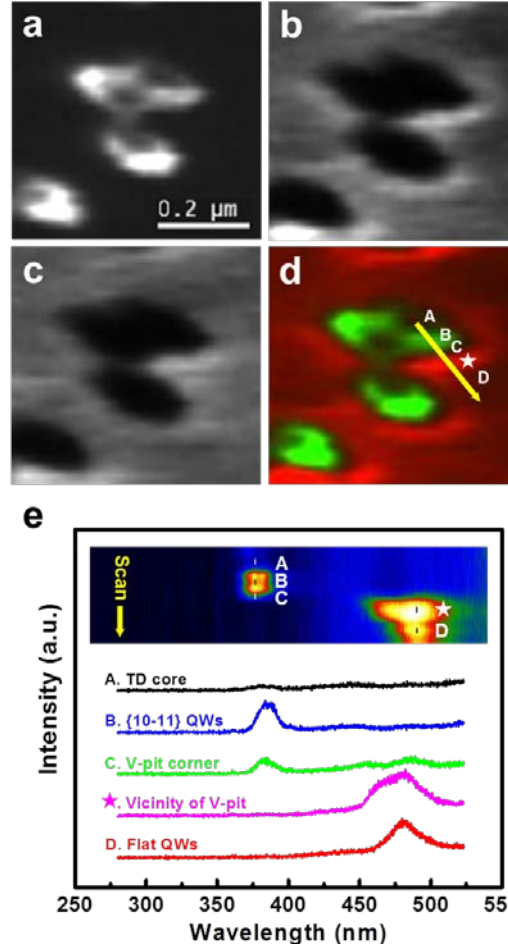


Figure 3.1.4. A plan-view of the luminescence mapping of an LED specimen, with wavelength windows equivalent to  $\{10\bar{1}1\}$ -plane and C-plane emission. Monochromatic CL wavelength mappings from (a) 370–390 nm ( $\sim\{10\bar{1}1\}$ -faceted QW), (b) 460–475 nm ( $\sim$ C-plane QW), and (c) 475–490 nm. (d) Red-green composite color CL mapping of semipolar  $\{10\bar{1}1\}$ - and C-plane QW emission wavelengths in green and red, respectively. Positions of the (A) TD core, (B)  $\{10\bar{1}1\}$ -faceted QWs, (C) V-pit corner, (D) extra emission of C-plane QWs near the V-pit corner, and (\*) normal C-plane QW emissions. (e) Inset is Hyperspectral CL map along the yellow arrow on (d). The x-axis refers to the wavelength and y-axis represents the spatial position on scan line. 5-distinguishable regions are indicated on the inset and each CL spectrum is stacked on the graph.

### 3. 1. 4. Bibliography

1. Chichibu, S. F.; Uedono, A.; Onuma, T.; Haskell, B. A.; Chakraborty, A.; Koyama, T.; Fini, P. T.; Keller, S.; Denbaars, S. P.; Speck, J. S.; Mishra, U. K.; Nakamura, S.; Yamaguchi, S.; Kamiyama, S.; Amano, H.; Akasaki, I.; Han, J.; Sota, T. *Nature materials* **2006**, 5, (10), 810-6.
2. Hangleiter, A.; Hitzel, F.; Netzel, C.; Fuhrmann, D.; Rossow, U.; Ade, G.; Hinze, P. *Physical Review Letters* **2005**, 95, (12).
3. Netzel, C.; Bremers, H.; Hoffmann, L.; Fuhrmann, D.; Rossow, U.; Hangleiter, A. *Physical Review B* **2007**, 76, (15).
4. Hitzel, F.; Klewer, G.; Lahmann, S.; Rossow, U.; Hangleiter, A. *Physical Review B* **2005**, 72, (8).
5. Kim, J.; Cho, Y. H.; Ko, D. S.; Li, X. S.; Won, J. Y.; Lee, E.; Park, S. H.; Kim, J. Y.; Kim, S. *Opt Express* **2014**, 22 Suppl 3, A857-66.
6. Li, Y. F.; Yun, F.; Su, X. L.; Liu, S.; Ding, W.; Hou, X. *J Appl Phys* **2014**, 116, (12).
7. Kim, J.; Kim, J.; Tak, Y.; Chae, S.; Kim, J. Y.; Park, Y. *Ieee Electr Device L* **2013**, 34, (11), 1409-1411.
8. Koike, K.; Lee, S.; Cho, S. R.; Park, J.; Lee, H.; Ha, J. S.; Hong, S. K.; Lee, H. Y.; Cho, M. W.; Yao, T. *Ieee Photonic Tech L* **2012**, 24, (6), 449-451.
9. Han, S. H.; Lee, D. Y.; Shim, H. W.; Lee, J. W.; Kim, D. J.; Yoon, S.; Kim, Y. S.; Kim, S. T. *Applied Physics Letters* **2013**, 102, (25).
10. Tsai, H.-L.; Wang, T.-Y.; Yang, J.-R.; Chuo, C.-C.; Hsu, J.-T.; Feng, Z.-C.; Shiojiri, M. *Materials Transactions* **2007**, 48, (5), 894-898.
11. Sharma, N.; Thomas, P.; Tricker, D.; Humphreys, C. *Applied Physics Letters* **2000**, 77, (9), 1274.
12. Bruckbauer, J.; Edwards, P. R.; Wang, T.; Martin, R. W. *Applied Physics Letters* **2011**, 98, (14), 141908.
13. Wu, X. H.; Elsass, C. R.; Abare, A.; Mack, M.; Keller, S.; Petroff, P. M.;

- DenBaars, S. P.; Speck, J. S. *Applied Physics Letters* **1998**, 72, (6).
14. Tao, T.; Zhi, T.; Liu, B.; Li, Y.; Zhuang, Z.; Xie, Z.; Chen, D.; Chen, P.; Zhang, R.; Zheng, Y. *physica status solidi (a)* **2014**, 211, (12), 2823-2827.
  15. Abell, J.; Moustakas, T. D. *Applied Physics Letters* **2008**, 92, (9), 091901.
  16. Wu, X. M.; Liu, J. L.; Quan, Z. J.; Xiong, C. B.; Zheng, C. D.; Zhang, J. L.; Mao, Q. H.; Jiang, F. Y. *Applied Physics Letters* **2014**, 104, (22).
  17. Doan, M.-H.; Lee, J. *Advances in Condensed Matter Physics* **2014**, 2014, 1-5.
  18. Jahn, U.; Brandt, O.; Luna, E.; Sun, X.; Wang, H.; Jiang, D. S.; Bian, L. F.; Yang, H. *Physical Review B* **2010**, 81, (12).
  19. PaÈssler, R. *Physica Status Solidi (b)* **1999**, 216, 975.

## **3. 2. Directly visualized distributions of $I_1$ - and $I_2$ -BSFs in semipolar $(11\bar{2}2)$ GaN thin film**

### **3. 2. 1. Introduction**

Conventional polar (0001) InGaN/GaN quantum wells (QWs) structure for light-emitting diodes (LEDs) has strong internal electrical fields along the  $c$ -axis due to a spontaneous- and a piezoelectric-polarization.<sup>1</sup> These internal electrical fields separate wave functions of electrons and holes in the QWs, leading to long radiative recombination times and thus low internal quantum efficiency (IQE), known as a quantum-confined stark effect (QCSE)<sup>2</sup> (see Figure 3.2.1). As increasing indium content of the QWs for longer wavelength, strain-induced piezoelectric field increases, leading to aggravation of QCSE and thus degradation of the LEDs efficiency. The QCSE, in addition, is also known to play an important role in the so-called efficiency droop phenomenon, which is a significant reduction of IQE at high current injection.<sup>3</sup>

Since the QCSE is a critical factor to deteriorate the emission efficiency of LEDs, many groups have been studied the growth of non-polar<sup>4,5</sup> and semi-polar<sup>6,7</sup> GaN films to reduce the internal electrical fields across in the QWs (Figure 3.2.1). Among the various non- and semi-polar planes,  $(11\bar{2}2)$  plane have known as a good candidate for high efficiency LED because of high indium incorporation rate guaranteeing superior crystal quality and low internal polarization-induced electric fields.<sup>8-10</sup>

The semi-polar  $(11\bar{2}2)$  InGaN/GaN QWs, however, suffered from complex structural defects such as basal plane stacking faults (BSFs), prismatic stacking faults (PSFs) and partial dislocations (PDs) besides threading dislocations (TDs) generally observed in polar GaN film. Figure 3.2.2 shows a schematic diagram of the semi-polar  $(11\bar{2}2)$  GaN film with the extended defects structure.

There are mainly three types of BSFs in hexagonal crystal structure,  $I_1$ ,  $I_2$ ,

and E. It can be considered as one, two, and three violations of the stacking rule, resulting in cubic stacks embedded in the hexagonal matrix. Since the forming energy increases with the number of violations, I<sub>1</sub>-BSFs have the lowest formation energy, leading to high density of it in semi-polar GaN film. The formation of I<sub>1</sub>-BSF is known to be originated from growth error during coalescence of islands in the Volmer-Wever growth mode.<sup>11</sup> The I<sub>1</sub>-BSFs are always bounded with sessile Frank-Shockley partial dislocations or connected to other I<sub>1</sub>-BSFs through PSFs accompanied with stair-rod dislocations.<sup>12, 13</sup> I<sub>2</sub>-BSFs are bounded with Shockley partial dislocations. It can be generated by growth errors or be formed by a single slip in basal plane.<sup>14</sup> Since E-BSFs have the highest formation energy, it was hardly observed in general semipolar thin film. The structural properties of the defects are summarized in Table 3.2.1.

In wurtzite (WZ) GaN, BSFs constitute zinc blende (ZB) segments in a WZ matrix. Since the bandgap energy of ZB GaN is smaller than that of WZ GaN, BSFs can be considered as QWs. The difference of the band gap energies were about 202 meV.<sup>14</sup> Characteristic luminescence of the structural defects was summarized in Table 3.2.2. The effective thicknesses of the BSFs induced QWs were calculated as 1.7 bilayers for I<sub>1</sub>-BSF, 2.7 bilayers for I<sub>2</sub>-BSF, and 3.7 bilayers for E-BSF considering microscopic electrostatic potential.<sup>15</sup> Therefore, the BSFs itself does not contribute to non-radiative recombination (NRC), it deteriorate the surface morphology of the thin films<sup>16-18</sup> and hetero-interfaces.<sup>19</sup> When the BSFs encounter the hetero-interface like InGaN/GaN, it may be terminated via a PD or threaded to the InGaN layer. In the latter case, it acts like a quantum wire<sup>20</sup> if the band alignment is type-I<sup>21</sup> or provide a competing recombination pathway for carriers if the band alignment is type-II.<sup>22-25</sup> It is not clear whether the band alignment for GaN WZ/ZB hetero-structure is type-II or I. Either way, the BSFs manipulate the performance of InGaN/GaN QWs and deteriorate the surface morphology. In addition, the structural defects associated with the BSFs such as PDs, PSFs, and stair-rod dislocations can contribute to the NRC, leading to decrease of LED efficiency. To improve the efficiency of semipolar (11 $\bar{2}$ 2)



InGaN/GaN LED, therefore, it is important that the characterizing of the structural defects according to their manufactural processes.

Since BSFs are atomically thin and it composes complex structure with other defects, however, it is difficult to identify their types and to aware their distributions by using conventional analyzing methods. For instance, imaging method of transmission electron microscopy (TEM) using  $\mathbf{g}\cdot\mathbf{R}$  invisibility criteria was applied to distinguish the  $I_1$ -BSFs and  $I_2$ -BSFs,<sup>26,27</sup> but the observation area is limited and it costs a lot of time and effort. In addition, scanning electron microscopy (SEM) combined with CL provided limited information due to lack of spatial resolutions.<sup>28, 29</sup>

In this chapter, it will be presented that TEM-CL analysis result of semi-polar  $(11\bar{2}2)$  GaN using optical fingerprint method. The  $(11\bar{2}2)$  GaN film was grown on hemispherical patterned sapphire substrate (HPSS) to reduce the structural defects. The CL maps with high spatial resolution clearly identify the type of defects and visualize their distribution at a glance. In addition, it will be discussed that the relationship between distributions of the BSFs and the substrate patterns.

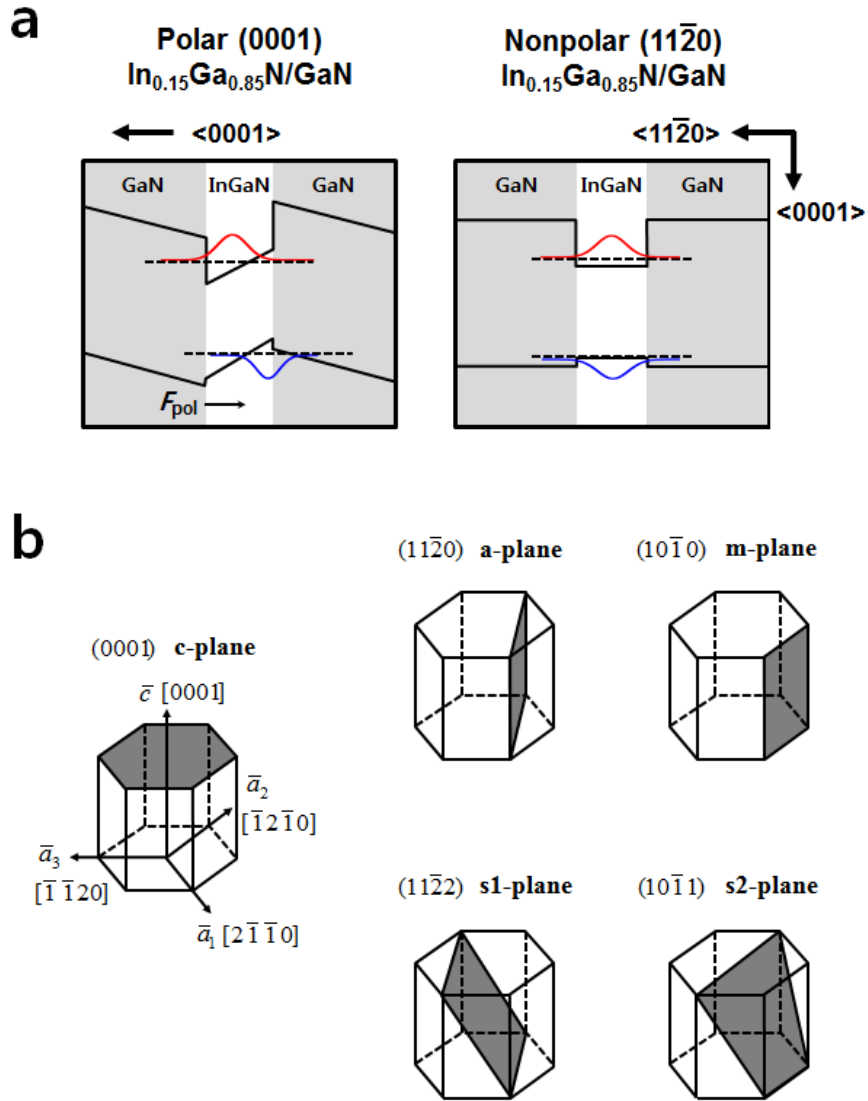


Figure 3.2.1. (a) Electronic band structure of strained InGaN/GaN QWs. (b) Schematics of crystallographic planes of typical polar, non- and semi-polar GaN.

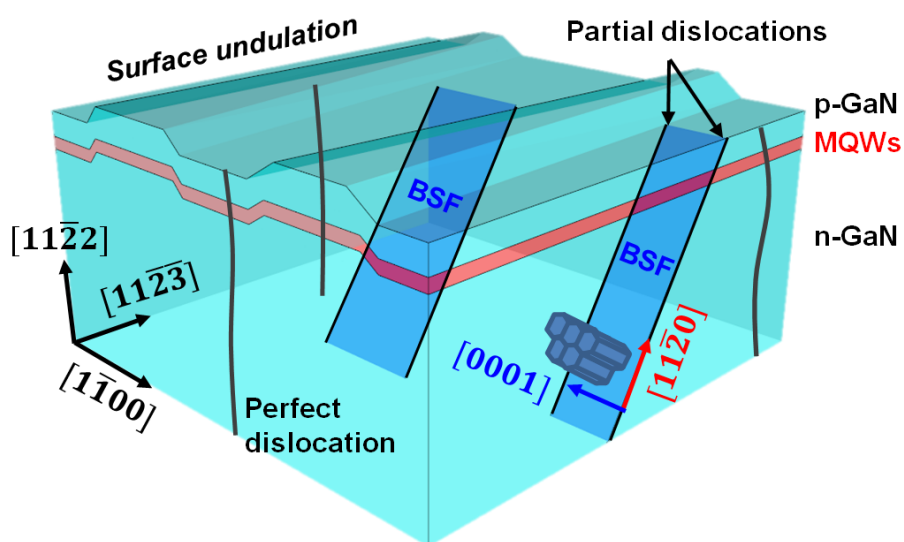


Figure 3.2.2. Schematic diagram of semipolar  $(11\bar{2}2)$  GaN film.

	Character	Type	$\vec{b}$	Remark
<b>Dislocation</b>	Perfect	Edge (a)	$1/3\langle 11\bar{2}0 \rangle$	
		Screw (c)	$[0001]$	
		Mixed (a+c)	$1/3\langle 11\bar{2}3 \rangle$	
	Partial	Frank-Shockley	$1/6\langle 20\bar{2}3 \rangle$	sessile, bound BSF-I <sub>1</sub> type
		Shockley	$1/3\langle 10\bar{1}0 \rangle$	glissile, bound BSF-I <sub>2</sub> type
		Frank	$1/2[0001]$	sessile, bound BSF-E type

	Plane	Type	$\vec{R}$	Stacking Sequence	Formation Energy (meV/Å <sup>2</sup> )
<b>Planar defect</b>	Basal	I <sub>1</sub>	$1/6\langle 20\bar{2}3 \rangle$	...ABAB <u>C</u> BCBC...	1.1 <sup>23</sup>
		I <sub>2</sub>	$1/3\langle 10\bar{1}0 \rangle$	...ABAB <u>C</u> ACAC...	2.7 <sup>23</sup>
		E	$1/2\langle 0001 \rangle$	...ABAB <u>C</u> ABAB...	4.2 <sup>23</sup>
	Prismatic	$\{11\bar{2}0\}$	$1/2\langle 10\bar{1}1 \rangle$		72 <sup>30</sup> , 99 <sup>31</sup>

Table 3.2.1. Dislocations and planar defects in hexagonal structure. **b**: Burger's vector, **R**: displacement vector.<sup>23, 30, 31</sup>

Type		Emission energy (eV)
WZ-GaN: FE		3.478 <sup>32</sup>
ZB-GaN: FE		3.276 <sup>33</sup>
BSFs	I <sub>1</sub>	3.40-3.42 <sup>14, 34, 35</sup>
	I <sub>2</sub>	3.32-3.36 <sup>14, 36</sup>
	E	3.29 <sup>14</sup>
PSFs, PDs, and stair-rod dislocations		3.21-3.33 <sup>34, 37</sup>
DAP		3.27 <sup>38</sup>

Table 3.2.2. Characteristic emission energies of the defects in GaN.<sup>32-38</sup> FE: free exciton, BSFs: basal-plane stacking faults, PSFs: prismatic stacking faults, PDs: partial dislocations, and DAP: donor-acceptor pair.

### 3. 2. 2. Experimental details

A (11 $\bar{2}2$ ) semipolar GaN film was grown on a hemispherical patterned m-plane sapphire substrate (HPSS) by metal organic chemical vapor deposition (MOCVD).<sup>39</sup> The HPSS was fabricated by using a conventional photolithography and dry etching process. The LED structure was composed of a 2  $\mu\text{m}$  thick Si-doped n-type GaN layer, five periods InGaN/GaN multi-quantum wells and a 150 nm thick Mg-doped p-type GaN layer. After the growth, thermal annealing was carried out at 800 °C for 5 minutes under N<sub>2</sub> atmosphere.

A cross-sectional and a plan-viewed TEM specimen were prepared with a classic mechanical thinning and an ion milling (PIPS, Gatan, USA) for an electron beam transparency. The cross section was chosen to intersect the BSFs along [11 $\bar{2}3$ ], which means that the zone axis of the specimen is parallel to  $\langle 1\bar{1}00 \rangle$ ; therefore, we can directly observe the distribution and the propagation of the BSFs from the substrate to the surface. The plan-view specimen were single side polished, leaving only the p-GaN surface. In other words, this specimen enables us to observe the surface distribution of BSFs penetrated the MQWs.

CL spectra and maps of the specimens were acquired by using the previously introduced custom-built stage for the conventional TEM (JEM-2010F, JEOL, Japan). A low electron-beam acceleration voltage (120 kV) was used to reduce the electron beam damage and to enhance the cross section of the inelastic scattering process. In addition, the specimen was cooled down to 137 K to improve the radiative recombination rate and to reduce the carrier diffusion length.

### 3. 2. 3. Results and discussions

Figure 3.2.3 (a) shows a cross-section view TEM-BF image of the (11 $\bar{2}$ 2) GaN based LED specimen. It were indicated that the region of the PSS pattern, unintentionally doped-GaN, n-typed doped GaN, and MQWs. Most of the defects were aligned toward a-axis. A void was observed on the PSS pattern, due to the competing growth of c-axis and a-axis. Figure 3.2.3 (b)-(f) represent the monochromatic CL intensity maps for characteristic luminescence of (11 $\bar{2}$ 2) GaN, i.e. NBE, I<sub>1</sub>-BSF type, I<sub>2</sub>-BSF type, PDs, PSFs, stair-rod dislocations and MQWs.

Five energy windows were selected according to the literature values.<sup>14</sup> The emission map of NBE (Fig. 3.2.3 (b)) shows dark regions due to non-radiative recombination (NRC) at the defects indicated with white arrows. In addition, it shows that the upper part of the epi structure about 2  $\mu$ m is brighter than the lower part, because n-type doped GaN enhance the luminescence of DAPs.<sup>39</sup> The emission map of I<sub>1</sub>-type BSFs (Fig. 3.2.3 (c)) and I<sub>2</sub>-type BSFs (Fig. 3.2.3 (d)) show bright straight inclined lines along the a-axis and these emissions are complementary to NBE emission (Fig. 3.2.3 (b)). Because, the luminescence of the BSFs are originated from the quantum well effect of zinc blende segment embedded in the wurtzite GaN matrix as we discussed previous section. The density of I<sub>1</sub>-type BSFs is higher than that of I<sub>2</sub>-type BSFs due to its low formation energy. Figure 3.2.3 (e) shows the emission of BSFs related structural defects such as PDs, PSFs, and stair-rod dislocations. It represents complex luminescence features spread over epitaxial layer and some of it accumulated around the PSS pattern. Figure 3.2.3 (f) shows that the emission of MQWs collapsed at the defect site observed in Fig. 3.2.3 (b).

Figure 3.2.4 (a) shows CL point spectra of the extended defects observed in Fig. 3.2.3. The dots represent measured CL spectrum and solid lines correspond to Gaussian fitted curves. The NBE peaks were observed in common. The ranges of emitted photon energy of NBE, I<sub>1</sub>-type BSFs, and I<sub>2</sub>-type BSFs were slightly

overlapped, but they are still distinguishable. Figure 3.2.4 (b) shows CL spectrum of MQWs centered at 2.8 eV.

Figure 3.2.5 shows CL analysis results on another site of the specimen. The complementary emissions of NBE and BSFs were observed again. Figure 3.2.5 (f) is red-green composite color map. Red color represents the emission of NBE (3.48–3.45 eV) (Fig. 3.2.5 (b)) and green color indicates the emissions of structural defects associated with the BSFs such as PDs, PFSs, and stair-rod dislocations (Fig. 3.2.5 (e)). It clearly shows that the fast growth of c-plane over the PSS pattern block the growth of a-plane, and leaving high density of structural defects around the PSS pattern and generating new structural defects at the growth meeting fronts.

As we discussed in previous section, the BSFs are stopped at the InGaN/GaN hetero junctions or threaded to surface of the p-GaN. Therefore, the TEM-CL analysis of the plan-view p-GaN specimen can enable us to observe the distributions of BSFs penetrated the MQWs. Figure 3.2.6 shows a plan-view TEM-BF image of the (11 $\bar{2}$ 2) p-GaN film and its CL mapping results. The flat top region of surface undulations was observed with dark contrast in BF image and with bright contrast in panchromatic CL map due to thickness effect.

Figure 3.2.6 (c), (d), and (e) shows the emission map of NBE, I<sub>1</sub>-type BSF, and I<sub>2</sub>-type BSF, respectively. The complementary emissions of NBE and BSFs were observed again. The luminescence features of I<sub>1</sub>-type BSFs show spread over the specimen with high density, while the emissions of I<sub>2</sub>-type BSF show narrow width with low density. Figure 3.2.6 (f) represents the emissions of structural defects associated with BSFs such as PDs, PSF, and stair-rod dislocations. It shows complex luminescence features composed of short segment line and spotty patterns.

Figure 3.2.7 (a) is a composite color CL map. The red, green, and blue colors refer to the emission map of NBE, I<sub>2</sub>-type BSF, and I<sub>1</sub>-type BSF, respectively. The distributions and identities of the BSFs were clearly observed at a glance with high resolution. Figure 3.2.7 (b) is also a composite color CL map. In this case, the structural defects associated with BSFs are colored in green. The point spectra of each labeled position in Fig. 3.2.7 (a) and (b) are presented in Fig. 3.2.7 (c). The



peaks of I<sub>1</sub>-type BSF were commonly observed in the four spectra due to the high density of it.

In this chapter, the emission properties of the semi-polar (11 $\bar{2}$ 2) GaN LED were analyzed by using TEM-CL. The CL maps with high spatial resolution clearly identify the type of the BSFs and visualize their distribution at a glance. In addition, it was directly observed that the influence of substrate pattern on defect reduction. This TEM-CL analysis method based on optical fingerprint identification can be applied to investigate the effect of various growth techniques and then contribute developing high power LED.

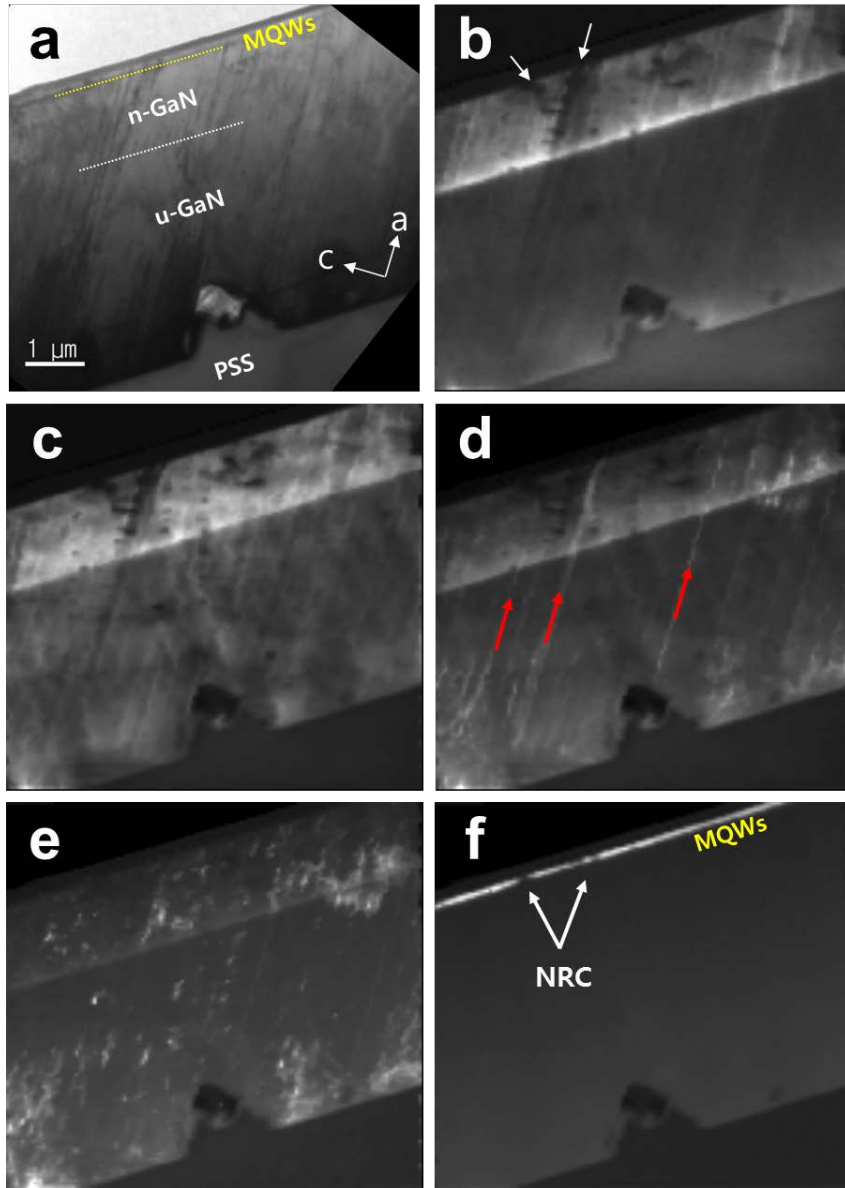


Figure 3.2.3. (a) A cross-section view TEM-BF image of the  $(11\bar{2}2)$  GaN based LED specimen. Monochromatic CL intensity maps from the emission of (b) NBE (3.48–3.45 eV), (c)  $I_1$  type BSFs (3.44–3.41 eV), (d)  $I_2$  type BSFs (3.39–3.35 eV), (e) PDs and PSFs (3.34–3.29 eV), and (f) MQWs (2.81–2.67 eV).

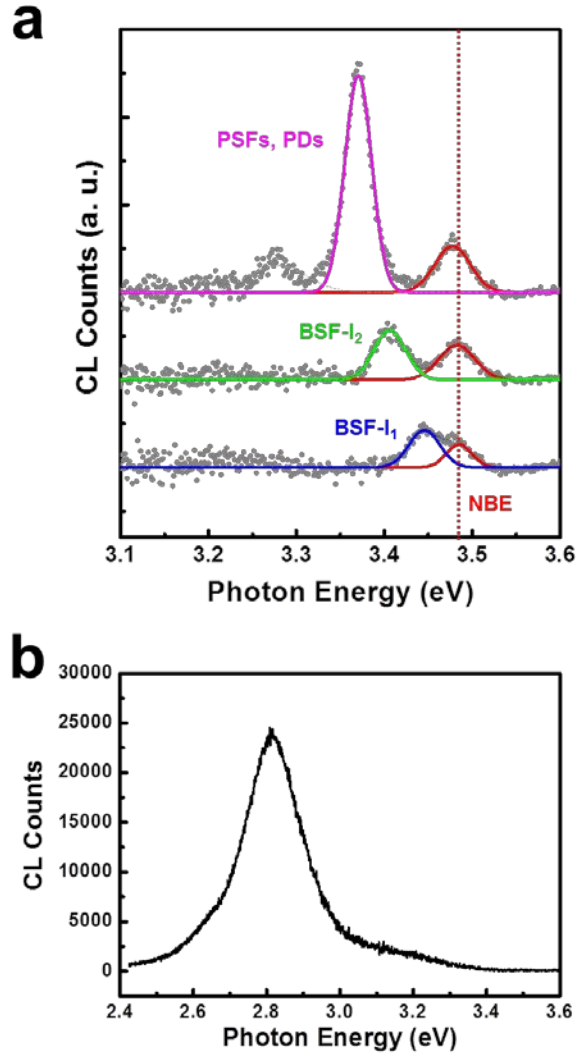


Figure 3.2.4. CL point spectra of the extended defects (a) and MQWs (b) in the cross-section view (11 $\bar{2}2$ ) GaN based LED specimen. Solid line represents Gaussian fitted curves and grey dots show measured CL spectra in (a).

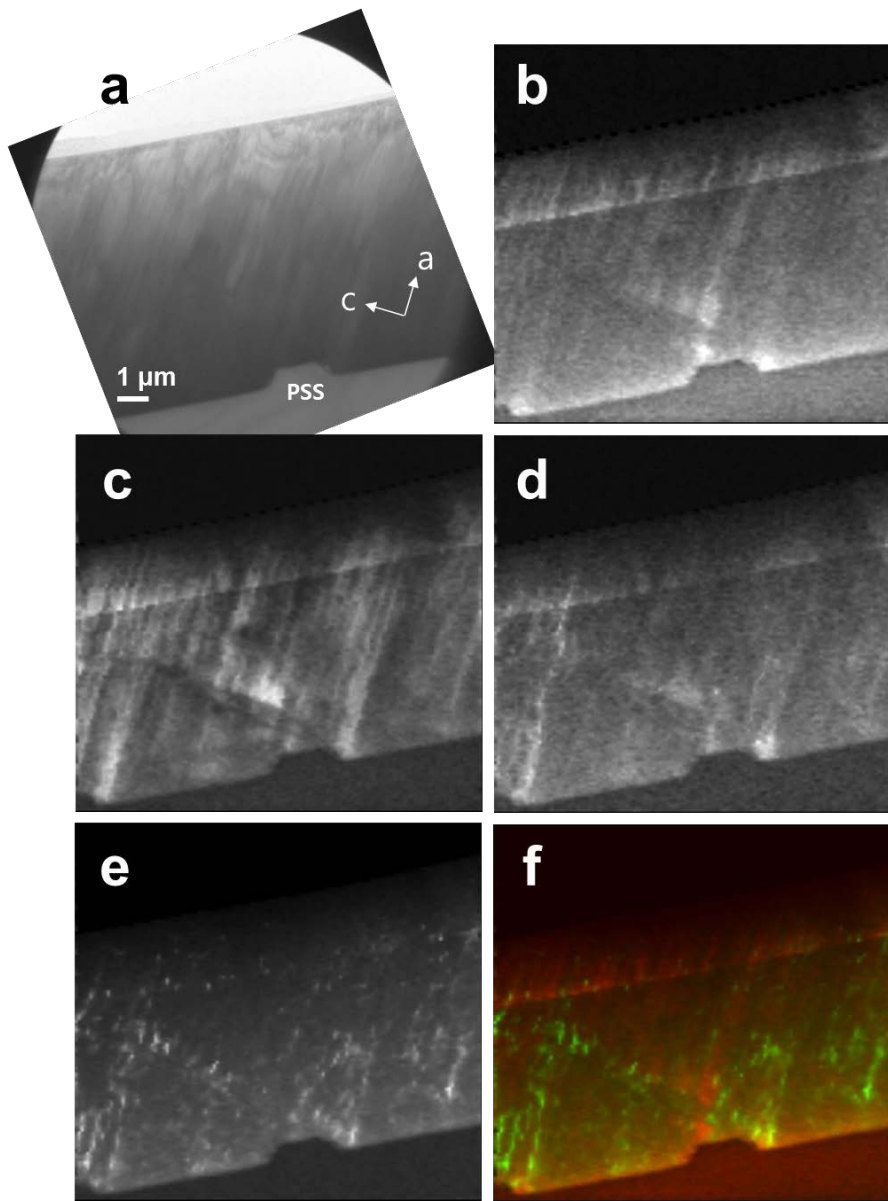


Figure 3.2.5. (a) A cross-section view TEM-BF image of the  $(11\bar{2})$  GaN based LED specimen. Monochromatic CL intensity maps from the emission of (b) NBE (3.48–3.45 eV) and (c)  $I_1$  type BSFs (3.42–3.40 eV), (d)  $I_2$  type BSFs (3.37–3.36 eV), (e) PDs and PSFs (3.33–3.21 eV), and Red-green composite color map (f). Red: NBE (3.48–3.45 eV) and Green: PSFs (3.33–3.21 eV).

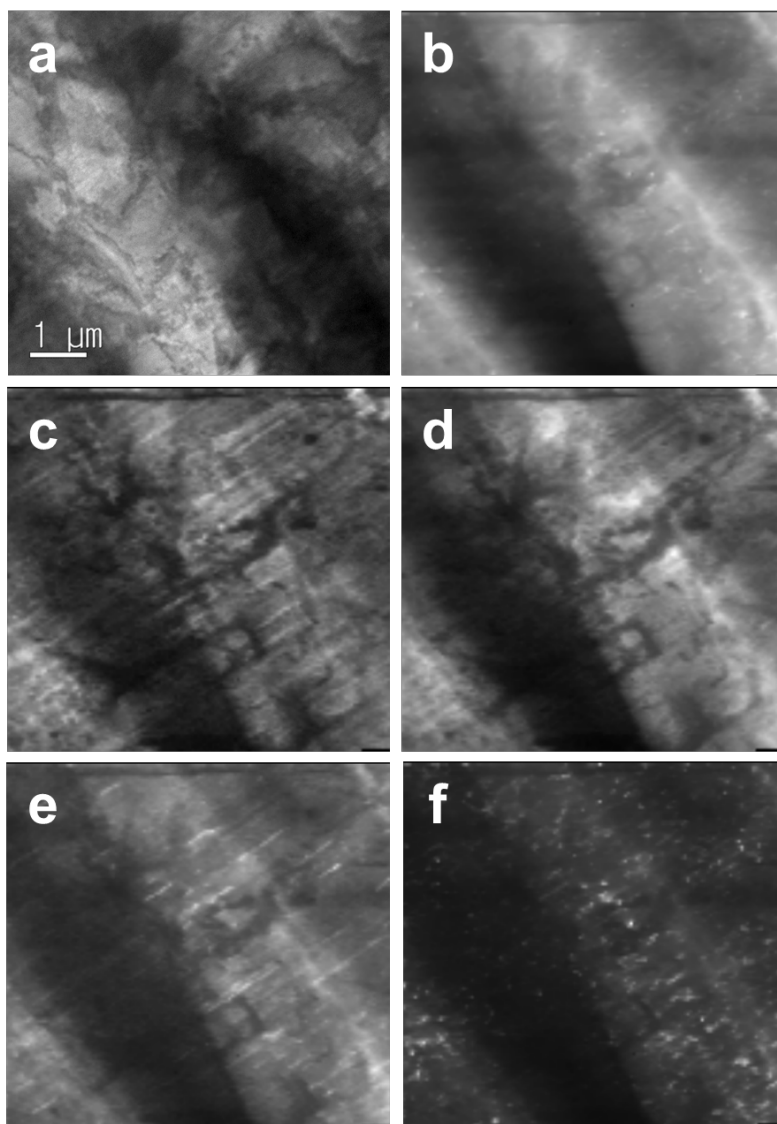


Figure 3.2.6. A plan-view TEM-BF image (a) and a panchromatic CL map (2.48–3.54 eV) of  $(11\bar{2}2)$  p-GaN film (b). Monochromatic CL intensity maps from the emission of (c) NBE (3.48–3.45 eV), (d)  $I_1$  type BSFs (3.42–3.41 eV), (e)  $I_2$  type BSFs (3.37–3.34 eV), and (f) PDs and PSFs (3.33–3.28 eV).

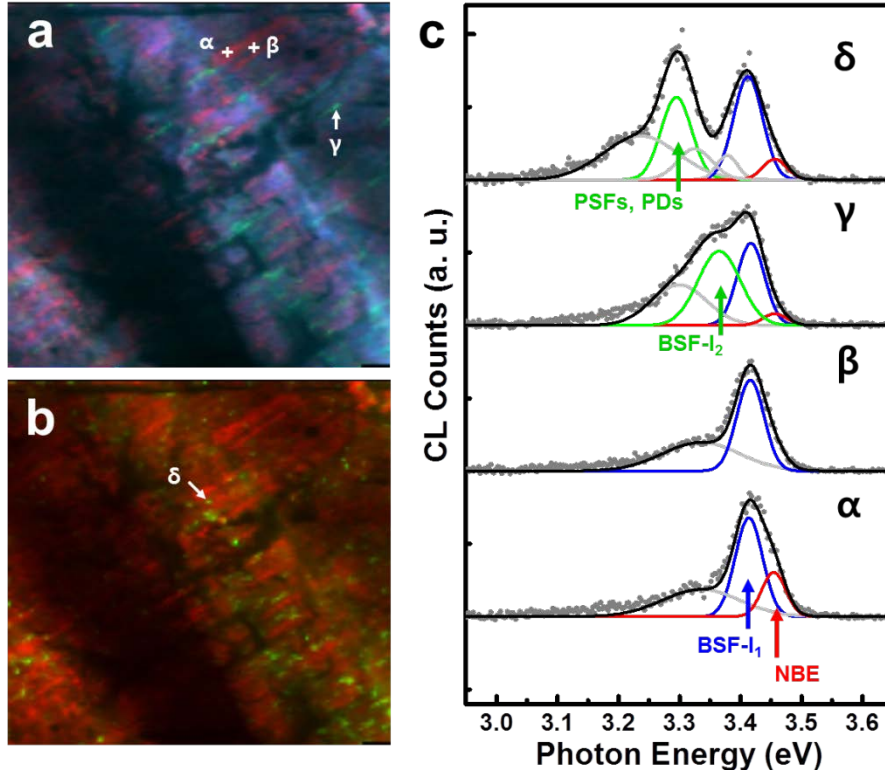


Figure 3.2.7. (a) Red-Green-Blue (RGB) color composite CL map. Red: NBE (3.48–3.45 eV), Green: I<sub>2</sub> type BSFs (3.37–3.34 eV), and Blue: I<sub>1</sub> type BSFs (3.42–3.41 eV). (b) Red-Green color composite CL map. Red: NBE (3.48–3.45 eV) and Green: PDs and PSFs (3.33–3.28 eV). (c) CL point spectra of four points labeled  $\alpha$ ,  $\beta$ ,  $\gamma$ , and  $\delta$  in (a) and (b). Solid line represents Gaussian fitted curves and grey dots show measured CL spectra.

### 3. 2. 4. Bibliography

1. Bernardini, F.; Fiorentini, V.; Vanderbilt, D. *Physical Review B* 1997, 56, (16), R10024.
2. Chichibu, S. F.; Uedono, A.; Onuma, T.; Haskell, B. A.; Chakraborty, A.; Koyama, T.; Fini, P. T.; Keller, S.; DenBaars, S. P.; Speck, J. S. *Nature materials* 2006, 5, (10), 810-816.
3. Ling, S.-C.; Lu, T.-C.; Chang, S.-P.; Chen, J.-R.; Kuo, H.-C.; Wang, S.-C. *Applied Physics Letters* 2010, 96, (23), 231101.
4. Chakraborty, A.; Haskell, B. A.; Keller, S.; Speck, J. S.; Denbaars, S. P.; Nakamura, S.; Mishra, U. K. *Japanese journal of applied physics* 2005, 44, (1L), L173.
5. Okuno, K.; Saito, Y.; Boyama, S.; Nakada, N.; Nitta, S.; Tohmon, R. G.; Ushida, Y.; Shibata, N. *Applied Physics Express* 2009, 2, (3), 031002.
6. Baker, T. J.; Haskell, B. A.; Wu, F.; Speck, J. S.; Nakamura, S. *Japanese Journal of Applied Physics* 2006, 45, (2L), L154.
7. Funato, M.; Ueda, M.; Kawakami, Y.; Narukawa, Y.; Kosugi, T.; Takahashi, M.; Mukai, T. *Japanese journal of applied physics* 2006, 45, (7L), L659.
8. Northrup, J. E. *Applied Physics Letters* 2009, 95, (13), 133107.
9. Zhao, Y.; Yan, Q.; Huang, C.-Y.; Huang, S.-C.; Hsu, P. S.; Tanaka, S.; Pan, C.-C.; Kawaguchi, Y.; Fujito, K.; Van de Walle, C. G. *Applied Physics Letters* 2012, 100, (20), 201108.
10. Wang, T. *Semiconductor Science and Technology* 2016, 31, (9), 093003.
11. Vennéguès, P.; Chauveau, J.; Bougrioua, Z.; Zhu, T.; Martin, D.; Grandjean, N. *Journal of Applied Physics* 2012, 112, (11), 113518.
12. Hirth, J.; Lothe, J. Ed.: John Willey & Sons 1982.
13. Drum, C. *Philosophical Magazine* 1965, 11, (110), 313-334.
14. Lähnemann, J.; Jahn, U.; Brandt, O.; Flissikowski, T.; Dogan, P.; Grahn, H. T. *Journal of Physics D: Applied Physics* 2014, 47, (42), 423001.

15. Lähnemann, J.; Brandt, O.; Jahn, U.; Pfüller, C.; Roder, C.; Dogan, P.; Grosse, F.; Belabbes, A.; Bechstedt, F.; Trampert, A. *Physical Review B* 2012, 86, (8), 081302.
16. Kappers, M.; Hollander, J.; McAleese, C.; Johnston, C.; Broom, R.; Barnard, J.; Vickers, M.; Humphreys, C. *Journal of crystal growth* 2007, 300, (1), 155-159.
17. Ploch, S.; Park, J. B.; Stellmach, J.; Schwaner, T.; Frentrup, M.; Niermann, T.; Wernicke, T.; Pristovsek, M.; Lehmann, M.; Kneissl, M. *Journal of Crystal Growth* 2011, 331, (1), 25-28.
18. Ploch, S.; Wernicke, T.; Dinh, D. V.; Pristovsek, M.; Kneissl, M. *Journal of Applied Physics* 2012, 111, (3), 033526.
19. Gil, B., III-nitride semiconductors and their modern devices. OUP Oxford: 2013; Vol. 18.
20. Jönen, H.; Rossow, U.; Bremers, H.; Hoffmann, L.; Brendel, M.; Dräger, A.; Schwaiger, S.; Scholz, F.; Thalmair, J.; Zweck, J. *Applied Physics Letters* 2011, 99, (1), 011901.
21. Belabbes, A.; de Carvalho, L.; Schleife, A.; Bechstedt, F. *Physical Review B* 2011, 84, (12), 125108.
22. Schulz, S.; Badcock, T.; Moram, M.; Dawson, P.; Kappers, M.; Humphreys, C.; O'Reilly, E. *Physical Review B* 2010, 82, (12), 125318.
23. Stampfl, C.; Van de Walle, C. G. *Physical Review B* 1998, 57, (24), R15052.
24. Badcock, T. J.; Dawson, P.; Kappers, M. J.; McAleese, C.; Hollander, J. L.; Johnston, C. F.; Sridhara Rao, D. V.; Sanchez, A. M.; Humphreys, C. J. *physica status solidi (c)* 2009, 6, (S2), S523-S526.
25. Badcock, T.; Hammersley, S.; Kappers, M.; Humphreys, C.; Dawson, P. *physica status solidi (c)* 2010, 7, (7-8), 1894-1896.
26. Wu, F.; Lin, Y.-D.; Chakraborty, A.; Ohta, H.; DenBaars, S. P.; Nakamura, S.; Speck, J. S. *Appl. Phys. Lett* 2010, 96, (23), 231912.



27. Dasilva, Y. A. R.; Chauvat, M.-P.; Ruterana, P.; Lahourcade, L.; Monroy, E.; Nataf, G. *Journal of Physics: Condensed Matter* 2010, 22, (35), 355802.
28. G hne, T.; Bougrioua, Z.; Venn gu s, P.; Leroux, M.; Albrecht, M. *Journal of applied physics* 2007, 101, (11), 113101.
29. Bastek, B.; Bertram, F.; Christen, J.; Wernicke, T.; Weyers, M.; Kneissl, M. *Applied Physics Letters* 2008, 92, (21), 212111-212111.
30. Northrup, J. E. *Applied physics letters* 1998, 72, (18), 2316-2318.
31. Elsner, J.; Kaukonen, M.; Heggie, M.; Haugk, M.; Frauenheim, T.; Jones, R. *Physical Review B* 1998, 58, (23), 15347.
32. Korona, K. *Physical Review B* 2002, 65, (23), 235312.
33. Renard, J.; Tourbot, G.; Sam-Giao, D.; Bougerol, C.; Daudin, B.; Gayral, B. *Applied Physics Letters* 2010, 97, (8), 081910.
34. Liu, R.; Bell, A.; Ponce, F.; Chen, C.; Yang, J.; Khan, M. A. *Applied Physics Letters* 2005, 86, (2), 1908.
35. Salviati, G.; Albrecht, M.; Zanotti-Fregonara, C.; Armani, N.; Mayer, M.; Shreter, Y.; Guzzi, M.; Melnik, Y. V.; Vassilevski, K.; Dmitriev, V. *PHYSICA STATUS SOLIDI A APPLIED RESEARCH* 1999, 171, 325-340.
36. Tischer, I.; Feneberg, M.; Schirra, M.; Yacoub, H.; Sauer, R.; Thonke, K.; Wunderer, T.; Scholz, F.; Dieterle, L.; M ller, E. *Physical Review B* 2011, 83, (3), 035314.
37. Mei, J.; Srinivasan, S.; Liu, R.; Ponce, F.; Narukawa, Y.; Mukai, T. *Applied physics letters* 2006, 88, (14).
38. Reshchikov, M. A.; Morkoc, H. *Journal of applied physics* 2005, 97, (6), 061301.
39. Jang, J.; Lee, K.; Hwang, J.; Jung, J.; Lee, S.; Lee, K.; Kong, B.; Cho, H.; Nam, O. *Journal of Crystal Growth* 2012, 361, 166-170.

### **3. 3. Correlation study between the surface morphology and the luminescence characteristics of semipolar $(11\bar{2}2)$ InGaN/GaN quantum wells**

#### **3. 3. 1. Introduction**

Conventional InGaN/GaN multi-quantum wells (MQWs) grown along the c-axis of the wurtzite structure have strong spontaneous and piezoelectric polarization field.<sup>1</sup> These internal fields cause spatial separations of electrons and holes in the MQWs, leading to hinder radiative recombination of the carriers, known as a quantum-confined stark effect (QCSE).<sup>2</sup> Since this QCSE deteriorate the emission efficiency of light-emitting diodes (LEDs), many groups have been studied to fabricate non-polar<sup>3,4</sup> and semi-polar<sup>5,6</sup> GaN epi structure to reduce the internal electric fields along the growth direction. Among various semi-polar planes,  $(11\bar{2}2)$  plane have attracted great interest in recent years because of high indium incorporation rate guaranteeing superior crystal quality with low internal polarization-induced electric fields.<sup>7,8</sup>

The semi-polar  $(11\bar{2}2)$  InGaN/GaN MQWs, however, were suffered from high density of extended defects<sup>9,10,11</sup> and anisotropic properties<sup>12,13,14</sup> due to the reduced crystal symmetries. As we already discussed about the effect of the extended defects in the previous chapter, we now focus on anisotropic structural and optical properties of the semi-polar  $(11\bar{2}2)$  InGaN/GaN MQWs.

Unlike the  $(0001)$  polar plane, the  $(11\bar{2}2)$  semi-polar plane endures lack of crystal symmetry, resulting in optical gain anisotropy<sup>12</sup> and anisotropic strain.<sup>13</sup> The surface morphology of the epitaxial layer, in addition, exhibit undulations accompanying with arrowhead like features pointing toward  $[11\bar{2}\bar{3}]$ .<sup>15,16,17</sup> The origin of this undulation is still in question; it is believed that different diffusion length of surface atoms along different crystal axis and lattice mismatch of the semi-polar GaN film on hetero-substrate might cause that anisotropy.<sup>14</sup>

In this study, it was directly observed and demonstrated that the anisotropic luminescence characteristics of the semipolar (11 $\bar{2}$ 2) InGaN/GaN MQWs located underneath the surface undulation by using transmission electron microscopy (TEM) combined with cathodoluminescence (CL). This technique enables us to analyze facet dependent emission of the MQWs beyond limitations of spatial resolution in photoluminescence<sup>12,13,14</sup> and scanning electron microscopy (SEM) combined with CL.<sup>18</sup>

### 3. 3. 2. Experimental details

The (11 $\bar{2}$ 2) semipolar GaN epi were grown on a hemispherical patterned m-plane sapphire substrate (HPSS) by metal organic chemical vapor deposition.<sup>19</sup> The LED structure was composed of a 2  $\mu\text{m}$  thick Si-doped n-type GaN layer, five periods InGaN/GaN multi-quantum wells and a 150 nm thick Mg-doped p-type GaN layer. After the growth, thermal annealing was carried out at 800 °C for 5 minutes under N<sub>2</sub> atmosphere.

A cross-sectional TEM specimen was prepared with a classic mechanical thinning and an ion milling (PIPS, Gatan, USA) for an electron beam transparency. The cross section was chosen to be perpendicular to the direction of arrowhead on surface; therefore, we can directly observe the correlation between surface undulation and internal MQWs structure.

CL spectra and maps of the specimens were acquired by using the previously introduced custom-built stage for the conventional TEM (JEM-2010F, JEOL, Japan). A low electron-beam acceleration voltage (120 kV) was used to reduce the electron beam damage and to enhance the cross section of the inelastic scattering process. In addition, the specimen was cooled down to 137 K to improve the radiative recombination rate and to reduce the carrier diffusion length.

High-resolution (HR) and annular dark-field (ADF) STEM images were acquired using a Cs-corrected STEM (ARM-200F, JEOL, Japan) operated at 200 kV and equipped with an aspherical aberration corrector (CEOS GmbH, Germany) and an EDS detector (X-Max, Oxford Instruments, UK)

### 3. 3. 3. Results and discussions

Figure 3.3.1 shows a cross-sectional ADF STEM image of the  $(11\bar{2}2)$  semipolar LED structure grown on the HPSS. The direction of zone axis is parallel to the direction of  $[11\bar{2}3]$  plane. Large voids are observed above the hemispherical pattern of the sapphire substrate. In the specimen, the width of the surface undulations was about  $1.3\ \mu\text{m}$  and the depth was about 220 nm. This can be varied depending on which position of the arrowhead-like morphology is sampled.

Figure 3.3.2 (a) is a cross-sectional BF image of the specimen. It shows that the InGa<sub>N</sub>/Ga<sub>N</sub> MQWs structure also follow the shape of the surface undulations, which is composed of a flat surface and a slanted surface. Figure 3.3.2 (b) is a panchromatic CL map of the region of Fig. 3.3.2 (a) in the wavelength range 350-550 nm. The emission of the MQWs seems like uniformly distributed over the undulated structure.

Figure 3.3.2 (c) shows CL point spectra of the two regions labeled GaN-A and GaN-B in Fig. 3.3.2 (b). A peak wavelength of the GaN-A spectrum is about 365 nm corresponding to an emission wavelength of near band edge (NBE) and basal plane stacking faults (BSFs),<sup>20,21</sup> which are commonly exist in  $(11\bar{2}2)$  GaN epi layer. The signal from GaN-B shows peak wavelength near 374.5 nm, which is known to be related with an emission wavelength of partial dislocations (PDs) and prismatic stacking faults (PSFs).<sup>20,21</sup> In addition, luminescence of donor-acceptor pair (DAP) is coexisting in the wavelength region.

Figure 3.3.2 (d) shows CL point spectra obtained from the flat and the sidewall MQWs. The peak emission wavelength of the flat MQWs is around 416 nm, and the luminescence of the sidewall MQWs contains two maxima near 458 nm and 478 nm. The sidewall MQWs emit long wavelengths compared to the flat MQWs, and exhibit broad full width at half-maximum.

Figure 3.3.3 shows CL intensity maps according to a wavelength window. Figure 3.3.3 (a) represents the emission map of NBE and BSFs. In this specimen, BSFs exist as oblique planes in the viewing direction. Unlike the line-shaped

emission pattern of BSFs discussed in previous chapter, distinct rectangular-shaped emission pattern was rarely observed. Because, high density of BSFs planes are overlapping each other, and the carriers can diffuse within the SF generated QW plane instead of being strongly confined. The emission map of PDs and PSFs (Figure 3.3.3 (b)) shows short line segment shaped emission pattern. In addition, it shows that the upper part of the epi structure about 2  $\mu\text{m}$  is brighter than the lower part, because n-type doped GaN enhance the luminescence of DAPs.<sup>22</sup>

Figure 3.3.3 (c-f) shows CL intensity maps of MQWs according to their emission wavelength. Figure 3.3.3 (f) is a red-green-yellow composite color CL map. Red color indicates the emission of sidewall MQWs, green color represents the emission of flat MQWs, and yellow color shows the emission of the NBE and BSFs. It clearly indicates that the flat MQWs emit shorter wavelength than the sidewall MQWs. These results are remarkable compared to the SEM-CL study, which only obtain a broad spectrum around 450 nm.<sup>18</sup>

A high-resolution STEM images were obtained to determine the thickness of the QWs and the crystal orientation of the sidewall QWs as shown in Figure 3.3.4 (a-d). The thickness of the sidewall MQWs are slightly thicker than that of the flat MQWs, but the difference is not large ( $< 0.1$  nm). By comparing the atomic arrangement (Fig. 3.3.4 (e)) with HR-STEM image (Fig. 3.3.4 (f)), it was verified that the sidewall MQWs formed on  $\{01\bar{1}1\}$  facet.

Figure 3.3.5 shows STEM-EDS analysis results of the specimen. The EDS quantification results reveal that the indium concentration of the sidewall  $\{01\bar{1}1\}$  facet MQWs is about four percent higher than that of the flat  $(11\bar{2}2)$  facet MQWs, and the EDS mapping results confirmed it. According to the Vegard's law, the bandgap of the InGa<sub>N</sub> ternary alloy is dependent on the indium composition  $x$  and a bowing parameter  $b$ .

$$E_{\text{InGaN}}(x) = (1-x)E_{\text{GaN}} + xE_{\text{InN}} - bx(1-x)$$

A calculated average  $E_g$  of the sidewall  $\{01\bar{1}1\}$  facet MQWs

( $\text{In}_{0.16}\text{Ga}_{0.84}\text{N}$ ) is 2.68 eV and that of the flat ( $11\bar{2}2$ ) facet MQWs is 2.84 eV ( $\text{In}_{0.12}\text{Ga}_{0.88}\text{N}$ ), where  $E_{\text{GaN}} = 3.4$  eV,  $E_{\text{InN}} = 0.77$  eV, and  $b = 1.43$  eV.<sup>23</sup> In other words, since the thicknesses of the quantum wells are almost the same, high In-incorporation efficiency of  $\{01\bar{1}1\}$  facet caused high In-composition, leading to long wavelength emission. According to a literature,<sup>24</sup> relative indium incorporation rate of several planes were reported as:

$$(10\text{-}11) > (11\text{-}22) > (0001) = (20\text{-}21) = (10\text{-}12)$$

This is also consistent with a report on the semi-polar facet properties of a GaN hexagonal annular structure<sup>25</sup> and conflict with characteristics of a planar grown semi-polar GaN.<sup>26</sup> Based on this, we speculated that the physical angle of the growth surface also affect the In-incorporation rate of the InGaN layer besides the growth conditions.

In conclusion, the surface undulations of the semipolar ( $11\bar{2}2$ ) GaN epi grown on an m-plane HPSS substrate were analyzed using TEM-CL, HR-STEM, and EDS. It was observed that the undulations are also present in MQWs composed of the flat ( $11\bar{2}2$ ) facets and the sidewall  $\{01\bar{1}1\}$  facets. The high In-incorporation efficiency of the sidewall  $\{01\bar{1}1\}$  facets caused high In composition and long wavelength emission, resulting in non-uniform luminescence and anisotropic emission of LED. It is expected that this result will assist the analysis on the characteristics of the semi-polar GaN epi and the development of the high efficiency GaN LEDs.

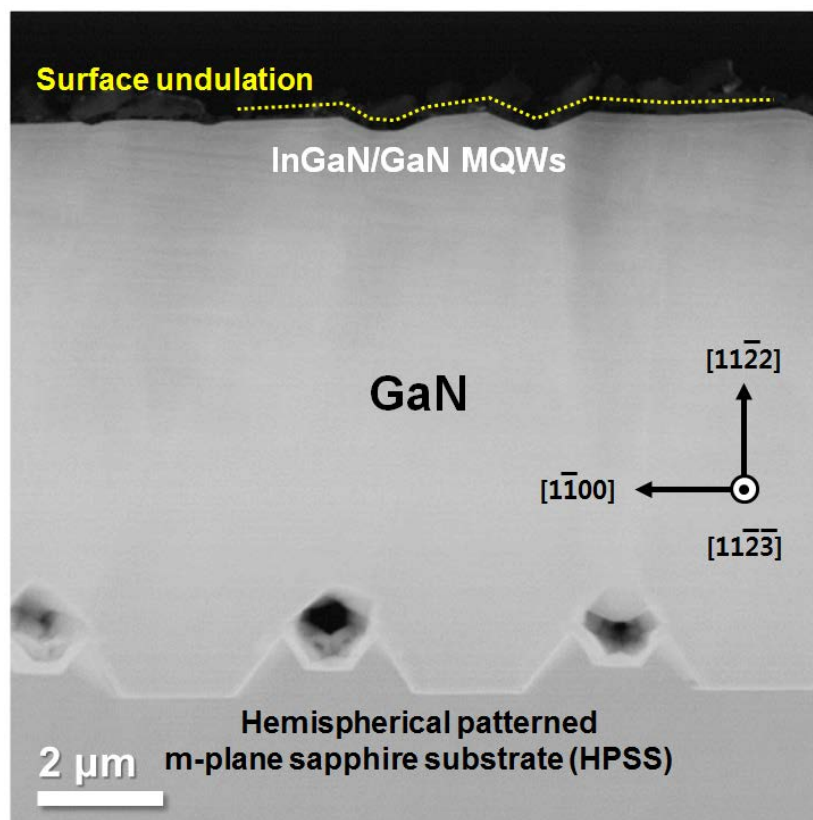


Figure 3.3.1. Cross-sectional ADF STEM image of the  $(11\bar{2}2)$  semipolar InGaN/GaN LED structure grown on the HPSS.



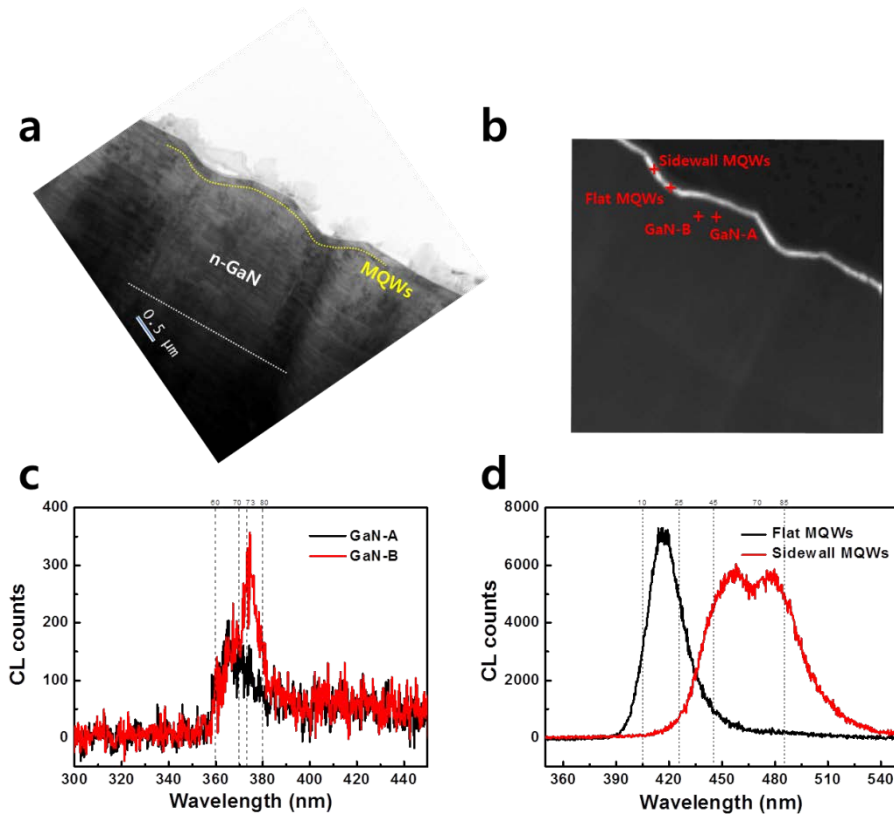


Figure 3.3.2. (a) Cross-sectional BF image of the specimen and (b) panchromatic CL map ( $\lambda$ : 350–550 nm) of the region of (a). (c) CL point spectra of the two regions labeled GaN-A and GaN-B in (b). (d) CL point spectra of the two regions labeled flat MQWs and sidewall MQWs in (b).

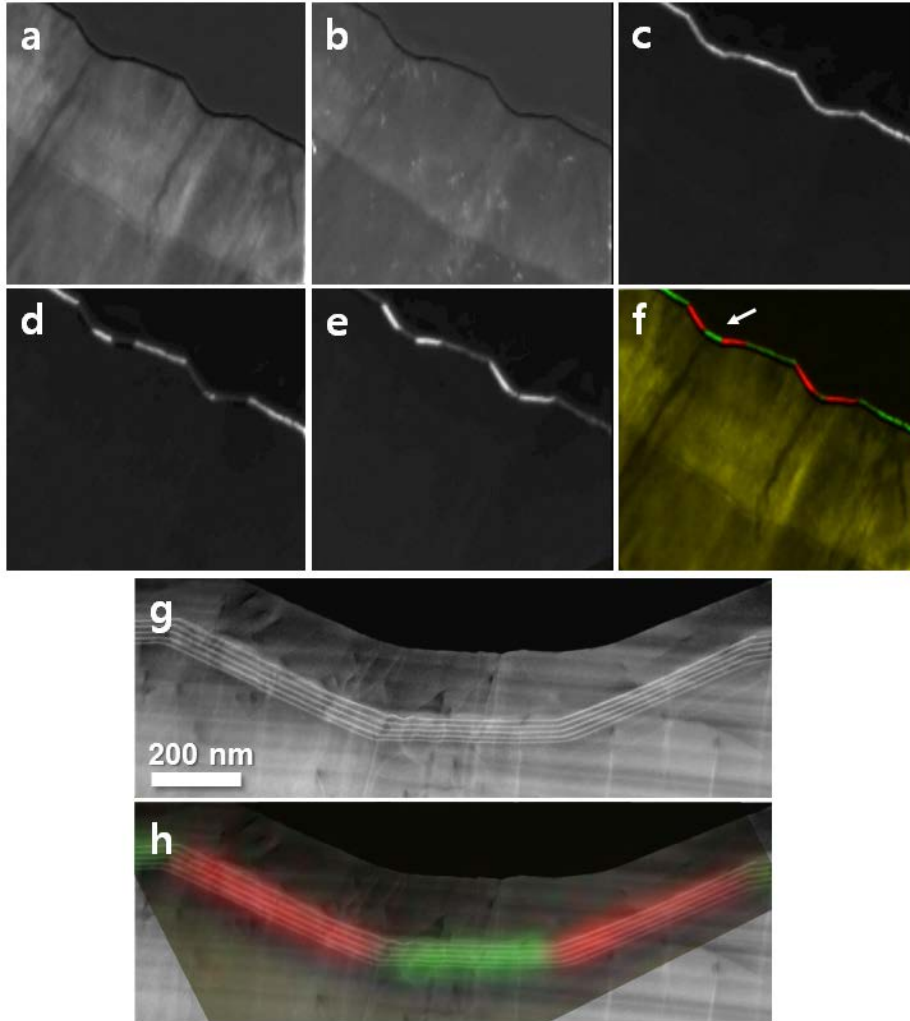


Figure 3.3.3. Monochromatic CL intensity mapping from the emission of (a) NBE and BSFs ( $\lambda$ : 360–370 nm), (b) PDs and PSFs ( $\lambda$ : 373–380 nm), (c) the intersection of the flat MQW and the sidewall MQWs ( $\lambda$ : 425–445 nm), (d) flat MQWs ( $\lambda$ : 410–425 nm), (e) sidewall MQWs ( $\lambda$ : 445–485 nm). (f) Red-green-yellow (RGY) composite color CL map. Red color indicates the emission of sidewall MQWs, green color represents the emission of flat MQWs, and yellow color shows the emission of the NBE and BSFs. (g) ADF-STEM image of the MQWs indicated with a white arrow in (f). (g) An enlarged image of (f) is superimposed on its STEM image (g).

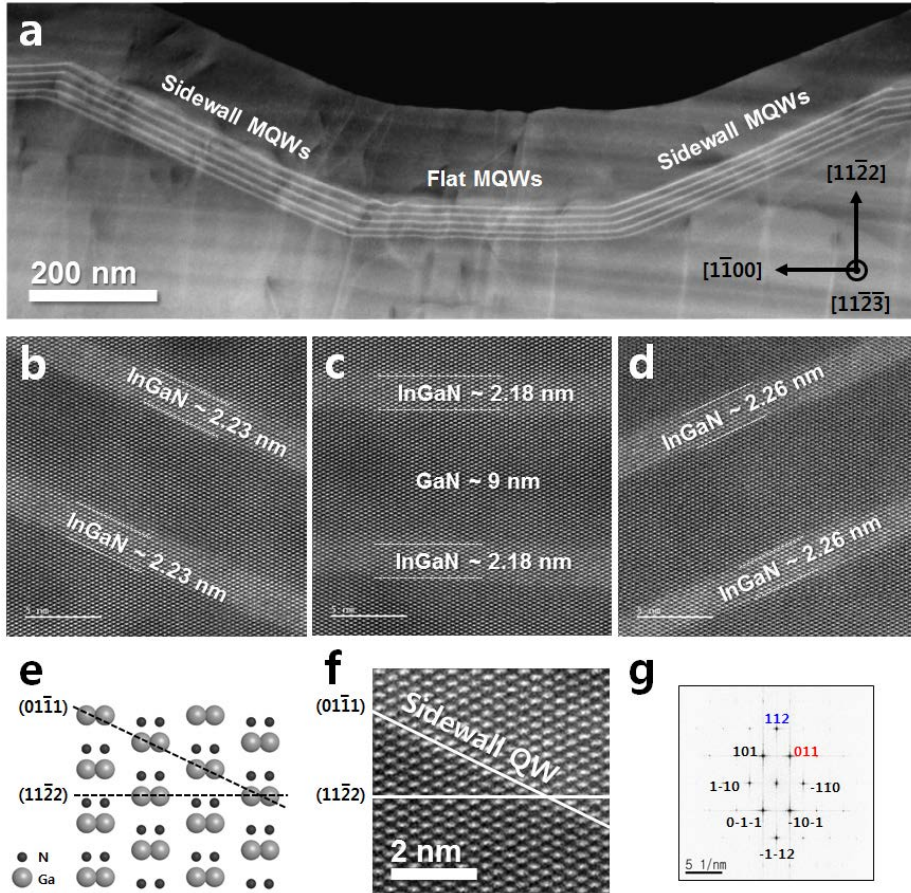


Figure 3.3.4. (a) The ADF-STEM image of the MQWs indicated with an white arrow in Fig. 3 (f). High-resolution ADF-STEM images of the left sidewall MQWs (b), flat MQWs (c), and right sidewall MQWs (d). (e) Schematic diagram of an atomic arrangement in semipolar  $(11\bar{2}2)$  GaN. (f) An enlarged image of the fig. 4(b). (g) fast Fourier transformed (FFT) image of fig. 4(f).

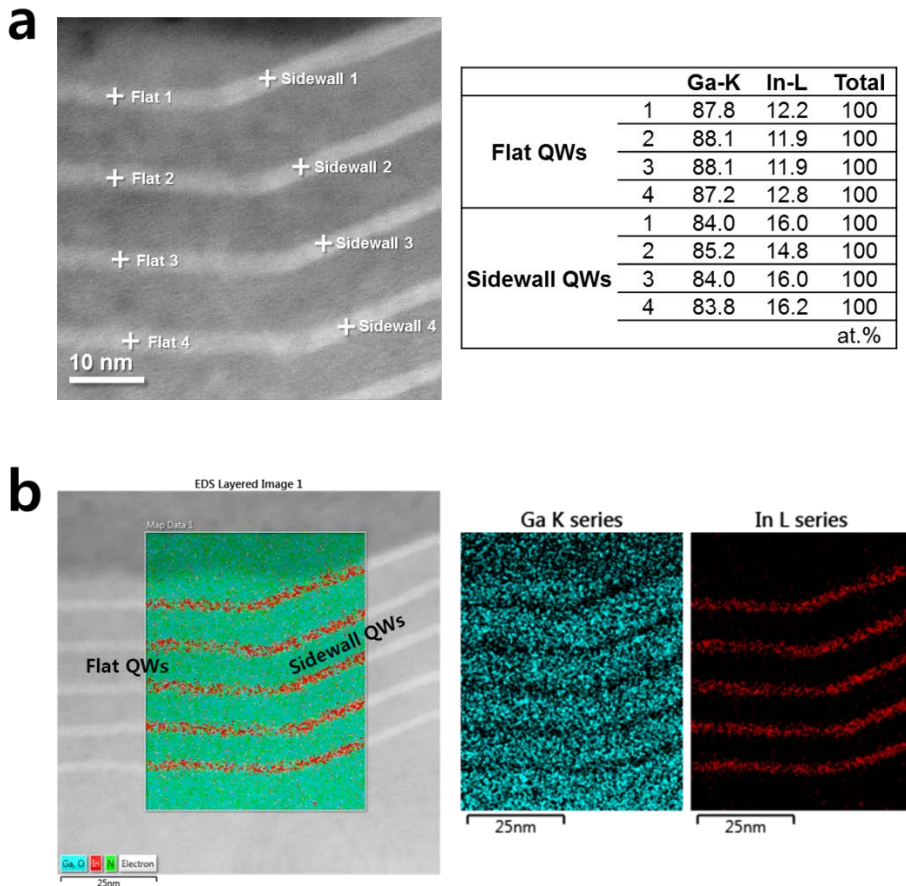


Figure 3.3.5. (a) STEM-EDS quantification results of the flat MQWs and the sidewall MQWs. (b) STEM-EDS mapping results of the flat MQWs and the sidewall MQWs.

### 3. 3. 4. Bibliography

1. Bernardini, F.; Fiorentini, V.; Vanderbilt, D. *Physical Review B* **1997**, 56, (16), R10024.
2. Chichibu, S. F.; Uedono, A.; Onuma, T.; Haskell, B. A.; Chakraborty, A.; Koyama, T.; Fini, P. T.; Keller, S.; DenBaars, S. P.; Speck, J. S. *Nature materials* **2006**, 5, (10), 810-816.
3. Chakraborty, A.; Haskell, B. A.; Keller, S.; Speck, J. S.; Denbaars, S. P.; Nakamura, S.; Mishra, U. K. *Japanese journal of applied physics* **2005**, 44, (1L), L173.
4. Okuno, K.; Saito, Y.; Boyama, S.; Nakada, N.; Nitta, S.; Tohmon, R. G.; Ushida, Y.; Shibata, N. *Applied Physics Express* **2009**, 2, (3), 031002.
5. Baker, T. J.; Haskell, B. A.; Wu, F.; Speck, J. S.; Nakamura, S. *Japanese Journal of Applied Physics* **2006**, 45, (2L), L154.
6. Funato, M.; Ueda, M.; Kawakami, Y.; Narukawa, Y.; Kosugi, T.; Takahashi, M.; Mukai, T. *Japanese journal of applied physics* **2006**, 45, (7L), L659.
7. Northrup, J. E. *Applied Physics Letters* **2009**, 95, (13), 133107.
8. Zhao, Y.; Yan, Q.; Huang, C.-Y.; Huang, S.-C.; Hsu, P. S.; Tanaka, S.; Pan, C.-C.; Kawaguchi, Y.; Fujito, K.; Van de Walle, C. G. *Applied Physics Letters* **2012**, 100, (20), 201108.
9. Gühne, T.; Bougrioua, Z.; Vennéguès, P.; Leroux, M.; Albrecht, M. *Journal of applied physics* **2007**, 101, (11), 113101.
10. Lacroix, B.; Chauvat, M.-P.; Ruterana, P.; Nataf, G.; De Mierry, P. *Applied Physics Letters* **2011**, 98, (12), 121916.
11. Vennéguès, P.; Chauveau, J.; Bougrioua, Z.; Zhu, T.; Martin, D.; Grandjean, N. *Journal of Applied Physics* **2012**, 112, (11), 113518.
12. Kojima, K.; Ueda, M.; Funato, M.; Kawakami, Y. *physica status solidi (b)* **2007**, 244, (6), 1853-1856.
13. Ueda, M.; Kojima, K.; Funato, M.; Kawakami, Y.; Narukawa, Y.; Mukai, T. *Applied physics letters* **2006**, 89, (21), 1907.

14. Zhao, G.; Wang, L.; Yang, S.; Li, H.; Wei, H.; Han, D.; Wang, Z. *Scientific reports* **2016**, 6.
15. Kappers, M.; Hollander, J.; McAleese, C.; Johnston, C.; Broom, R.; Barnard, J.; Vickers, M.; Humphreys, C. *Journal of crystal growth* **2007**, 300, (1), 155-159.
16. Ploch, S.; Park, J. B.; Stellmach, J.; Schwaner, T.; Frentrup, M.; Niermann, T.; Wernicke, T.; Pristovsek, M.; Lehmann, M.; Kneissl, M. *Journal of Crystal Growth* **2011**, 331, (1), 25-28.
17. Ploch, S.; Wernicke, T.; Dinh, D. V.; Pristovsek, M.; Kneissl, M. *Journal of Applied Physics* **2012**, 111, (3), 033526.
18. Lee, S.; Jang, J.; Lee, K. H.; Hwang, J. H.; Jeong, J.; Nam, O. *physica status solidi (a)* **2012**, 209, (8), 1526-1529.
19. Jang, J.; Lee, K.; Hwang, J.; Jung, J.; Lee, S.; Lee, K.; Kong, B.; Cho, H.; Nam, O. *Journal of Crystal Growth* **2012**, 361, 166-170.
20. Liu, R.; Bell, A.; Ponce, F.; Chen, C.; Yang, J.; Khan, M. A. *Applied Physics Letters* **2005**, 86, (2), 1908.
21. Lähnemann, J.; Jahn, U.; Brandt, O.; Flissikowski, T.; Dogan, P.; Grahn, H. T. *Journal of Physics D: Applied Physics* **2014**, 47, (42), 423001.
22. Phillips, M. R.; Telg, H.; Kucheyev, S. O.; Gelhausen, O.; Toth, M. *Microscopy and Microanalysis* **2003**, 9, (02), 144-151.
23. Wu, J.; Walukiewicz, W.; Yu, K.; Ager III, J.; Haller, E.; Lu, H.; Schaff, W. *J. Appl. Phys. Lett* **2002**, 80, 4741-4743.
24. Wernicke, T.; Schade, L.; Netzel, C.; Rass, J.; Hoffmann, V.; Ploch, S.; Knauer, A.; Weyers, M.; Schwarz, U.; Kneissl, M. *Semiconductor science and technology* **2012**, 27, (2), 024014.
25. Ko, Y.-H.; Song, J.; Leung, B.; Han, J.; Cho, Y.-H. *Scientific reports* **2014**, 4.
26. Wang, Y.; Shimma, R.; Yamamoto, T.; Hayashi, H.; Shiohama, K.-i.; Kurihara, K.; Hasegawa, R.; Ohkawa, K. *Journal of Crystal Growth* **2015**, 416, 164-168.

## **3. 4. Directly observed interband transitions in few-layered MoS<sub>2</sub> by using cathodoluminescence**

### **3. 4. 1. Introduction**

Atomically thin structures of transition-metal dichalcogenides (TMDCs) have attracted great interest in condensed matter studies because of their distinctive optical properties, including an emerging photoluminescence (PL) in a monolayer limit,<sup>1,2</sup> valley-selective dichroism,<sup>3-5</sup> strain modulated optical gap<sup>6, 7</sup> and strong photocurrent generations.<sup>8,9</sup> These two-dimensional (2D) TMDCs have also shown positive prospects for use in various electronic and optoelectronic devices.<sup>10-13</sup>

Unfortunately, it is still under investigation that the fundamental understandings about the optoelectronic structure such as an alteration of bandgap transition and a variation of an exciton binding energy according to their thickness. In the case of MoS<sub>2</sub>, the most important feature is that the bulk state maintains indirect-gap transition down to bilayer and then drastically turns into direct-gap transition on monolayer. This distinctive character is unveiled by several optical spectroscopy measurements such as photocurrent,<sup>2</sup> photoluminescence excitation<sup>14,15</sup> and PL.<sup>1,2,16</sup> More specifically, the PL spectra of few-layer MoS<sub>2</sub> have characteristic two exciton peaks (so-called A and B exciton<sup>17</sup>) around 1.9 eV, which is due to spin-orbit splitting at the K/K' valleys in the Brillouin zone.<sup>9,18</sup> Until recently, these peaks have been considered as an occurrence of direct band edge transitions because of the dramatic increasing of the intensity on monolayer thickness.

The 2D MoS<sub>2</sub>, however, is expected to preserve the strong excitonic effects due to weak dielectric screening and geometrical confinement of the excitons. Recent theoretical calculations based on quasiparticle self-consistent GW<sup>19</sup> and G<sub>0</sub>W<sub>0</sub><sup>20</sup> methods predicted that monolayer MoS<sub>2</sub> has a strong excitonic binding energy (~0.9 eV), and therefore quasiparticle bandgap is more larger than

the experimentally observed exciton peaks in PL. In addition, it was firstly proposed that an existence of many strongly bound excitonic states (so-called C excitons) near 2.5 eV around  $\Gamma$ -point in the Brillouin zone (Figure 3.4.1. (b)) through sophisticated approach to many-body effects by using GW-Bethe-Salpeter equation (GW-BSE).<sup>18</sup> Despite of these computational advances, experimental evidences for existence of C excitons are barely reported.

In this study, interband transitions of large excitonic states near  $\Gamma$ -point resulting in luminescence were firstly demonstrated in mechanically exfoliated few-layer MoS<sub>2</sub> by using TEM-CL. The CL is an emission of light resulted in recombination of electron-hole pair, which is generated in the material under electron beam bombardment. While the photon in PL tends to stimulate particular emission process depending on their excitation energy, the high energy and large momentum of the electron beam in CL lead to excite all the possible luminescence mechanisms.<sup>21-23</sup> This unique nature of the CL enables us to observe the interband transitions of the excitonic states in few-layer MoS<sub>2</sub>. These experimental results may provide crucial information for developing 2D TMDCs devices.



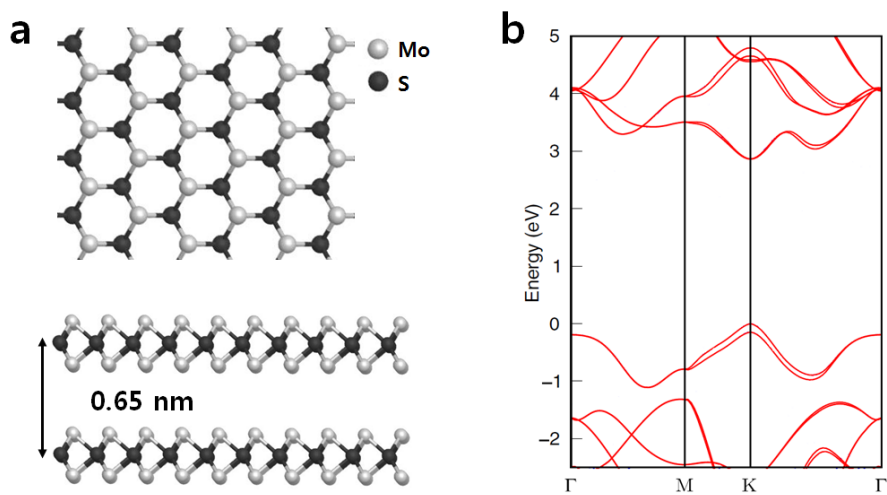


Figure 3.4.1. (a) Top and side views of the 2H-MoS<sub>2</sub>. Mo atoms have trigonal prismatic coordination. (b) Calculated band structure of monolayer MoS<sub>2</sub>.<sup>18</sup>

### 3. 4. 2. Experimental details

Figure 3.4.2 (a) shows a flow chart of this experiment. Figure 3.4.2 (b) shows optical images of mechanically exfoliated MoS<sub>2</sub> flake on SiO<sub>2</sub>/Si substrate from a piece of single crystalline MoS<sub>2</sub> (SPI supplies, USA) by using scotch tape. After optical measurements, the MoS<sub>2</sub> flake was directly transferred on perforated carbon film (SPI supplies, USA) for TEM analysis. To do this transfer, firstly, the MoS<sub>2</sub> flake was covered with a TEM grid and one droplet of isopropyl alcohol (IPA) was released on the grid. After the IPA was completely dried, we immersed the sample in 30% solution of potassium hydroxide (Alfa Aesar, USA) to remove the SiO<sub>2</sub> layer. After separating the grid from the Si substrate, the grid was rinsed with deionized water.

(1) Optical measurements. An Ar ion laser with 515.5 nm line was used for Raman measurement and a He-Cd laser with 441.6 nm line was applied for PL measurement. A 50 x objective lens (0.8 N.A.) was used for focusing the laser beam and collecting the scattered light. To avoid heating, the laser power was maintained below 0.2 mW.

(2) TEM-CL measurements. The previously introduced custom-built CL stage was used for measuring TEM-CL. A field emission type TEM (JEM-2010F, JEOL, Japan) was used to acquire images and to generate CL signals. In addition, other TEM (JEM-2100F, JEOL, Japan) was used to obtain the CL signal at low acceleration voltage 80 kV. The CL signals were collected by a mirror and were transmitted to an optical fiber, which was coupled to a spectrometer with a 300 mm<sup>-1</sup> and 500 mm<sup>-1</sup> groove density grating. Each point spectrum was obtained for two second per iteration and accumulated for 30 times. The spectrum was measured at room temperature and at 137 K with liquid nitrogen cooling.

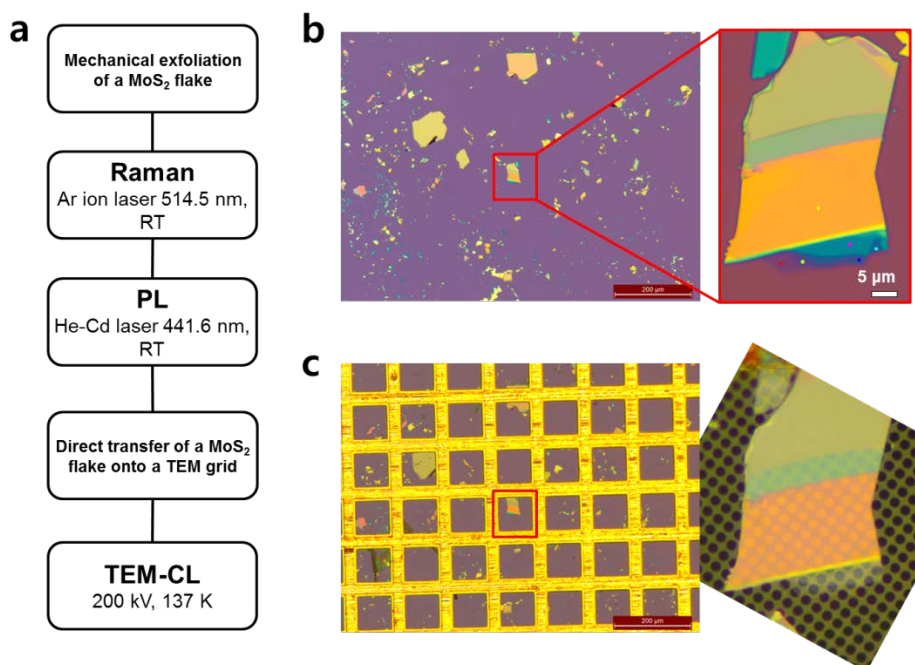


Figure 3.4.2. (a) Experimental flow chart. Optical images of the MoS<sub>2</sub> flake on a SiO<sub>2</sub>/Si substrate (b) and on a perforated carbon film (c).

### 3. 4. 3. Results and discussions

Figure 3.4.3 (a) is an optical image of the MoS<sub>2</sub> flake lying on SiO<sub>2</sub>/Si substrate. Based on the interference color through underlying oxide layer, the number of MoS<sub>2</sub> layer can be roughly estimated from NL-(N = 1-3, 5 and 6) layer to bulk (> 10 layers). To verify the number of the MoS<sub>2</sub> layer, Raman spectrum is acquired for each sheet (Fig. 3.4.3 (b)). As the film thickness is increased, it is observed that the frequency of the out-of-plane vibration mode  $A_{1g}$  is increased due to enhancement of the restoring force between inter-layer S-S bonds, and the frequency of the in-plane vibration mode  $E_{2g}^1$  is decreased due to an expansion of intra-layer S-Mo-S distance.<sup>24</sup> In addition, Stokes and anti-Stokes Raman spectra in low frequency region (Fig. 3.4.3 (c)) confirmed the thickness of each layer based on its unique pattern, which is composed of highest frequency shear mode (S1) and lowest frequency breathing mode (B1).<sup>25</sup>

Figure 3.4.3 (d) shows PL spectra of the few-layer MoS<sub>2</sub>. Two emission peaks are located at 1.85 eV and 1.99 eV in monolayer; the peaks correspond to A and B excitonic transitions occurring at the K-point of Brillouin zone. The emission intensities of the peaks increase with thinning of the sheets and shows drastic enhancement at the monolayer. According to the previous studies,<sup>1, 2</sup> this phenomenon is caused by an alteration of interband transition according to their thickness. In other word, the indirect bandgap transition occurred from  $\Lambda$  valley in the conduction band to  $\Gamma$  point in the valence band until bilayer, and it changed to direct bandgap transition at K point in the monolayer.

Note that significant emission intensities of A and B peaks are still observed from the bilayer to the six layers, even though their band structure already changed to indirect bandgap. This could be explained by PL excitation mechanisms. In the indirect bandgap material, the conduction band minimum and the valence band maximum are located having different  $k$  values. Photon absorption in the material, therefore, must imply either an emission or absorption of phonons to conserve momentum during the excitation, thus showing low probability of the

occurrence. In the meantime, the wavelength of the excitation laser is 442 nm, which is over the A and B excitonic transition energy and below the direct bandgap energy. This quasi-resonant excitation preferentially can increase the population of carriers in the K valley without phonon-assisted process, leading to recognizable exciton recombination.<sup>16</sup> The intensity of peak A is, furthermore, relatively stronger than that of peak B. This strong peak probably originated from high carrier density, because a majority of the hole-carriers exists in the highest-lying valence band states in equilibrium.

Figure 3.4.3 (e) shows low intensity region of the PL spectra. It is observed that a broad spectrum around 550 nm arising from SiO<sub>2</sub> thin film. This background peak can be generated and be added to the signal of MoS<sub>2</sub>, even if several tens of MoS<sub>2</sub> layers are lying on the SiO<sub>2</sub> thin film due the penetration depth of the visible light within the submicron scale. This area, unfortunately, overlaps with the region of the high bound exciton energy and the quasiparticle bandgap energy, which are predicted by various-simulation works.<sup>18-20</sup> Due to the background area, it is difficult to determine the presence of the unknown peak associating with the high-energy excitonic states, as well as a notable peak has not been observed in the region.

After the optical measurements, the MoS<sub>2</sub> flake was carefully transferred on perforated carbon film and inserted in a transmission electron microscope (TEM) chamber (Fig. 3.4.4 (a)). In the chamber, the specimen was cooled down to 137 K for acquiring an unambiguous CL peak and avoiding carbon contamination. To reduce electron beam damage, the beam exposure time was minimized during CL measurement. The CL spectrum of each layer was measured on freestanding region to rule out the background peak of the supporting film.

Figure 3.4.4 (b) exhibits the CL spectra of mono- and bi-layer MoS<sub>2</sub>. In the monolayer, the CL signal is very weak and is hard to decide an existence of excitonic states. The bilayer, however, shows significant emission signal; this is contrary to the thicker film emits weaker signal in PL (see Fig. 3.4.3 (d)). This phenomenon might be explained by comparing luminescence mechanism between

CL and PL. While one photon in PL simply generates one electron-hole pair, an incident electron in CL dissipates its energy through successive inelastic scatterings in the material and generates multiple electron-hole pairs in the excitation volume. Therefore, carrier generations are enhanced with increasing of scattering events in the thicker film, leading to stronger CL signal. Figure 3.4.4 (c) also shows that the intensity of CL spectrum gradually increases as increasing the number of the MoS<sub>2</sub> layer. In the spectrum of six-layer MoS<sub>2</sub>, three distinguishable peaks are observed: One intensive peak around 480 nm and two less intensive peaks around 620 nm. According to the spectrum deconvolution result (Fig. 3.4.5), energy of the each peak corresponds to ~2.55 eV, 2.07 eV and 1.90 eV. The two peaks centered at 1.9 eV and at 2.08 eV correspond to the A and B excitonic peaks, which were observed in PL. Blue shift of the peak in CL could be caused by the low measuring temperature.

Note that the intensive peak centered at 2.55 eV disappeared in PL and appeared in CL (Fig. 3.4.6). In other words, the strong peak marked as C is observed only in CL measurement. This newly founded emission began to appear from two-layer MoS<sub>2</sub> and still exist over ten-layer MoS<sub>2</sub> (Fig. 3.4.7). After that, it is transformed into another peak in the thickness of at least several tens of layers (Fig. 3.4.7). According to the theoretical calculation,<sup>18, 26</sup> the peak might be arising from six nearly degenerate excitonic states accompanying with transitions between the highest valence band and the three lowest conduction bands near  $\Gamma$  point.

Figure 3.4.8 represents CL mapping results of the MoS<sub>2</sub> flake on the perforated carbon film. The three distinct regions correspond to the thin, intermediate, and thick area of Figure 3.4.7. The peak wavelength maps were acquired after Gaussian fitting of each CL point spectrum according to their energy window range. It clearly visualized that the peak wavelength of the excitonic emissions tend to red shift on carbon film. This tendency was observed to be the largest at peak C.

To understand why the high-energy excitons were only appeared in CL analysis, we considered the differences of luminescence mechanism between the

PL and CL. For generating the high-energy transitions, above all, the number of electrons in the conduction band near  $\Gamma$  point should be sufficient. In the case of PL, the energy of excited carrier strongly depends on the energy of laser  $h\nu$ , tending to excite selectively. When the excitation energy is below the bandgap energy, the most of the excited carriers are concentrated on K point.<sup>16</sup> When the excitation energy is over the bandgap energy, the produced electron and hole near  $\Gamma$  point are immediately separated from each other before making C exciton because of band nesting phenomenon,<sup>9,15</sup> leading to radiative recombination loss and enormous photoconductivity.

On the other hand, in the case of CL, highly accelerated electrons in TEM are capable of exciting most valance electrons regardless of their ionization energy. In addition, the excited valance electrons possess energy and momentum simultaneously because source electrons transfer their energy to the valance electrons through successive scatterings. The generated carriers, therefore, might tend to spread over Brillouin zone instead of being concentrated in a particular valley, thus filling large excitonic states enough to observe radiative recombination,<sup>22, 23</sup> while avoiding the band nesting.

In terms of experimental method, high acceleration voltage of 200 kV was applied to the electron beam for excitation in CL. This high voltage can damage the specimen. In the case of MoS<sub>2</sub>, atomic displacement was reported under highly accelerated electron beam irradiation.<sup>27</sup> However, no significant difference was observed in the visible region of CL spectrum as increasing the acceleration voltage from 80 kV to 200 kV (Figure 3.4.9).

To summarize, luminescence properties of few-layered MoS<sub>2</sub> are investigated by the optical excitation and the electron beam excitation. As a result, it was observed the peak A and B due to direct excitonic transitions at K point in both PL and CL. The large peak C, which is more close to the quasiparticle bandgap energy, is appeared only in CL. Based on previously reported calculation works, I speculate that the peak C correspond to nearly degenerate excitonic transitions near  $\Gamma$  point. To our knowledge, the luminescence of the high-energy

exciton in MoS<sub>2</sub> is firstly observed and investigated. I believe that these results provide insight into understanding the excitonic behavior of MoS<sub>2</sub> and exploring novel optoelectronic applications.



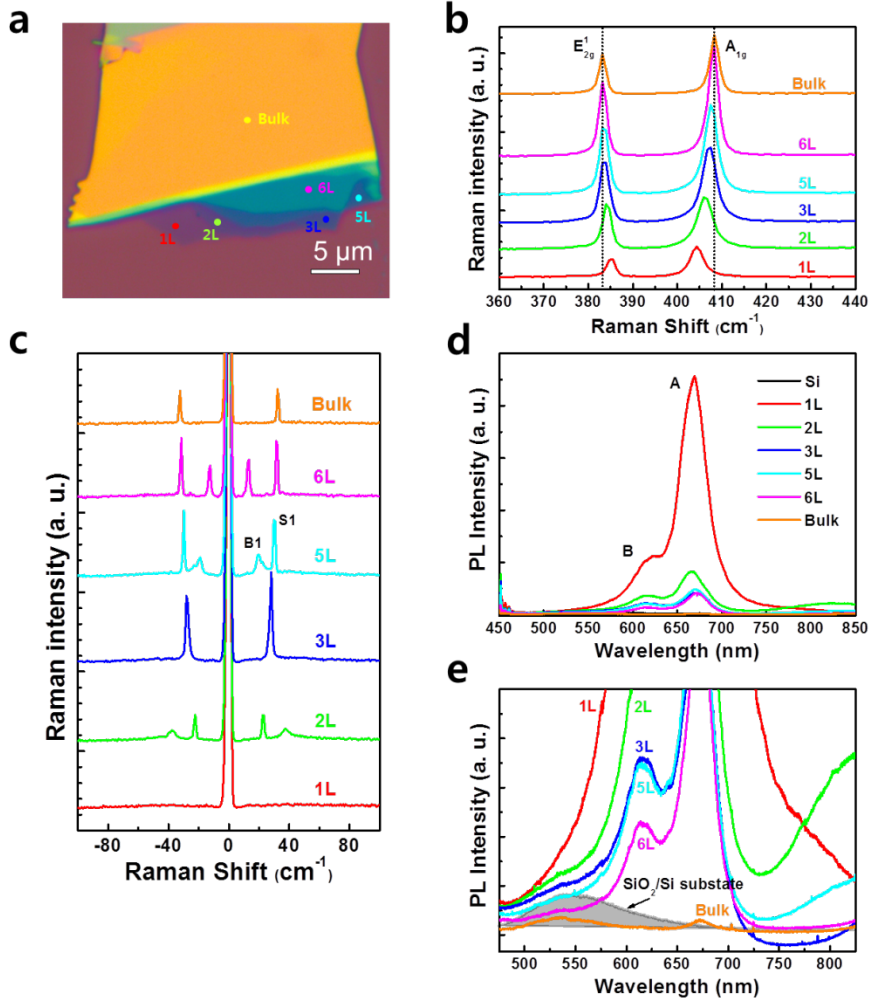


Figure 3.4.3. Characterizing optical properties of few-layer MoS<sub>2</sub> using laser excitation (a) An optical image of a mechanically exfoliated MoS<sub>2</sub> flake on a SiO<sub>2</sub>/Si substrate. (b) PL spectra of the few-layer MoS<sub>2</sub> (c) Closeup of the PL spectra near the emission of SiO<sub>2</sub>/Si substrate, which is filled with gray color. (d) Raman spectra of the NL-(N = 1-3, 5 and 6) and bulk MoS<sub>2</sub>. The position of two main mode ( $E_{2g}^1$  and  $A_{1g}$ ) are indicated as dot-line. (e) Stokes and anti-Stokes Raman spectra of the few-layer MoS<sub>2</sub>.

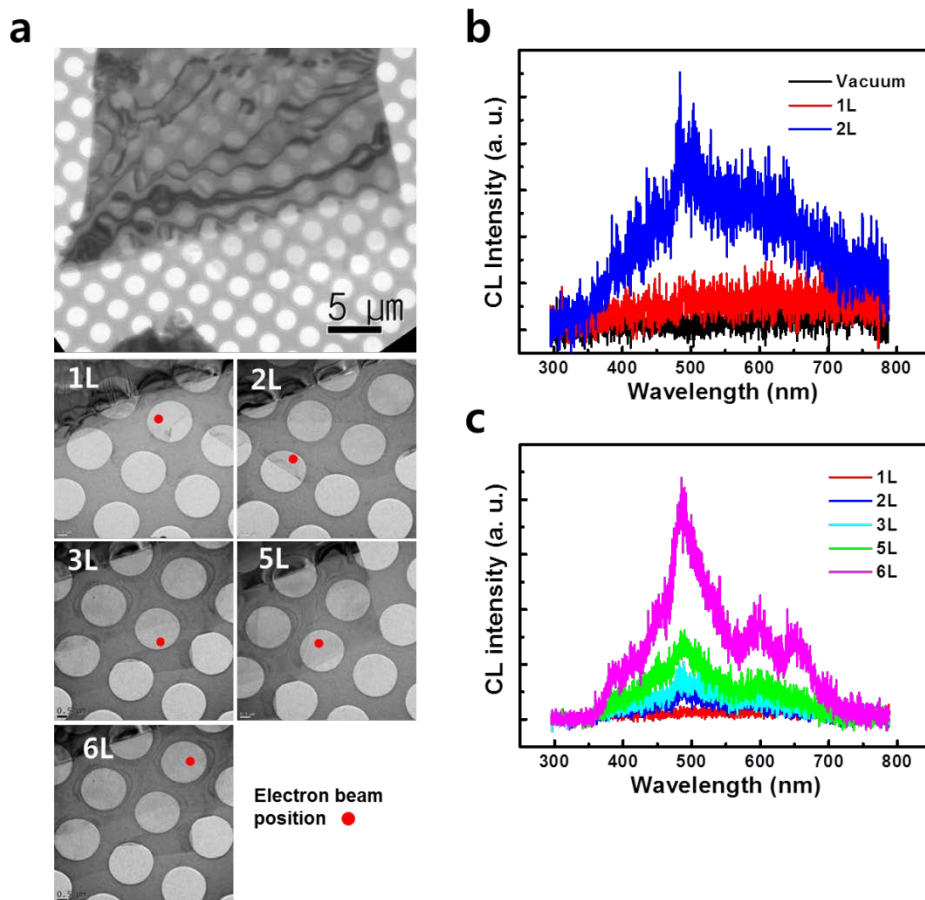


Figure 3.4.4. (a) A bright field TEM image of the MoS<sub>2</sub> flake on the perforated carbon film. (b) CL spectra of the mono- and bi-layer MoS<sub>2</sub> (c) CL spectra of the NL-(N = 1-3, 5 and 6) MoS<sub>2</sub>

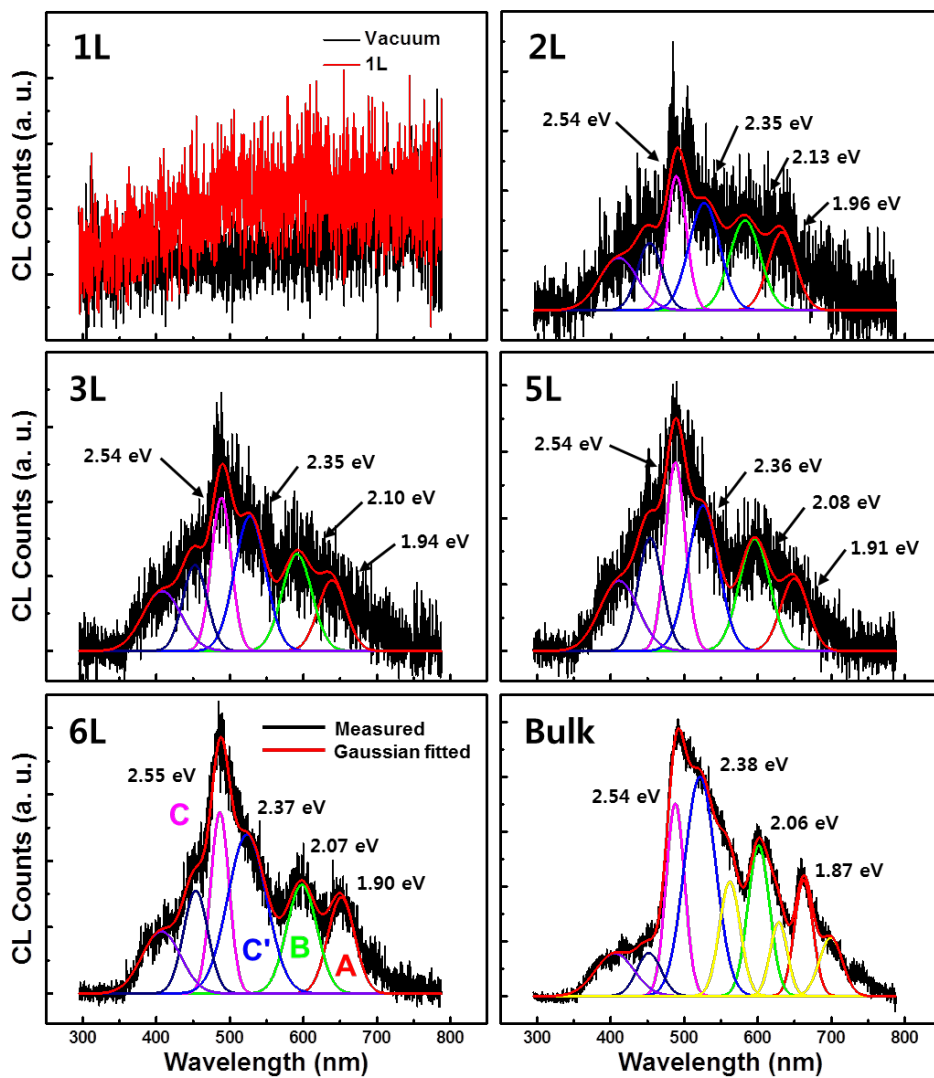


Figure 3.4.5. Measured CL spectrum (black line) and Gaussian fitted CL spectrum (red line) of NL-(N = 1-3, 5 and 6) MoS<sub>2</sub>. Each Gaussian-fitting curve is indicated by their peak energy.

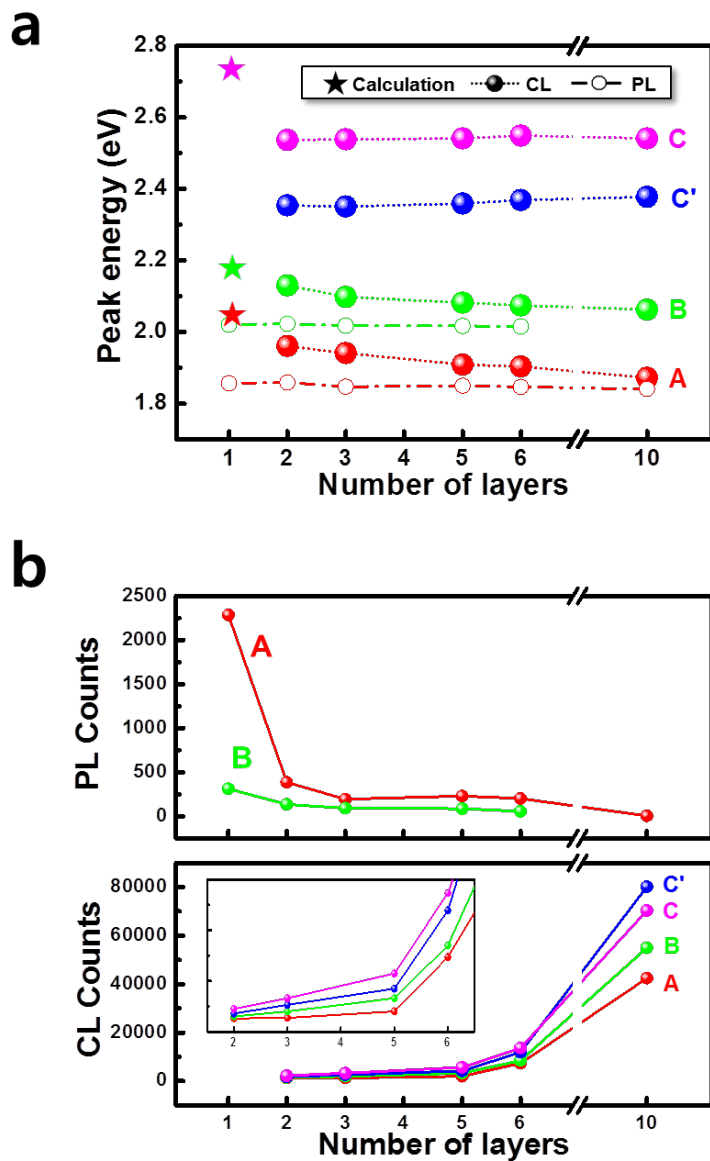


Figure 3.4.6. (a) Peak energies of the A, B, C' and C excitons with a different number of layers. (b) Peak intensities of the A, B, C' and C excitons with a different number of layers.

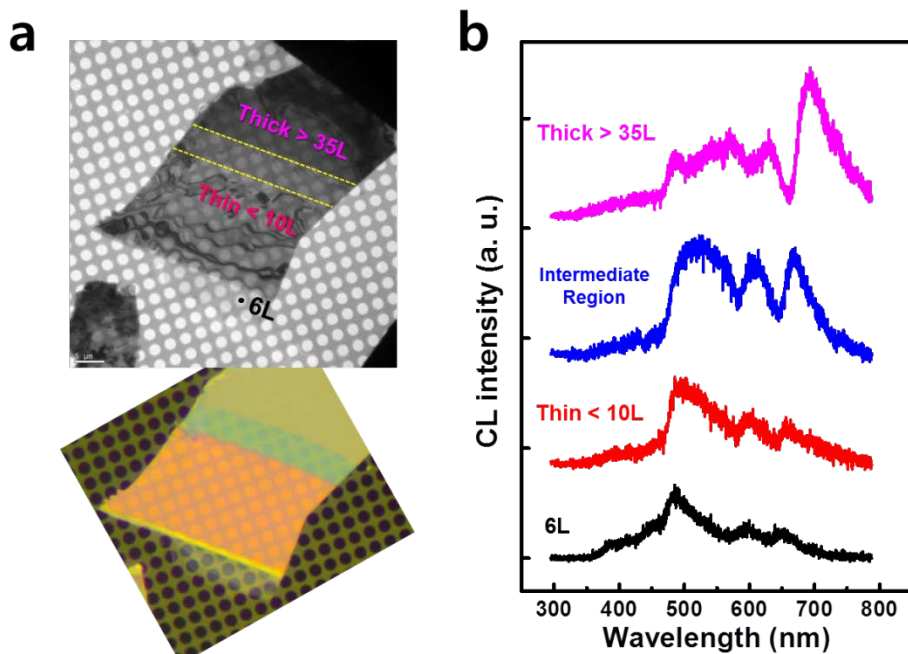


Figure 3.4.7. (a) A bright field TEM image and an optical image of the MoS<sub>2</sub> flake on a perforated carbon film. (b) CL spectra with a different number of layers.

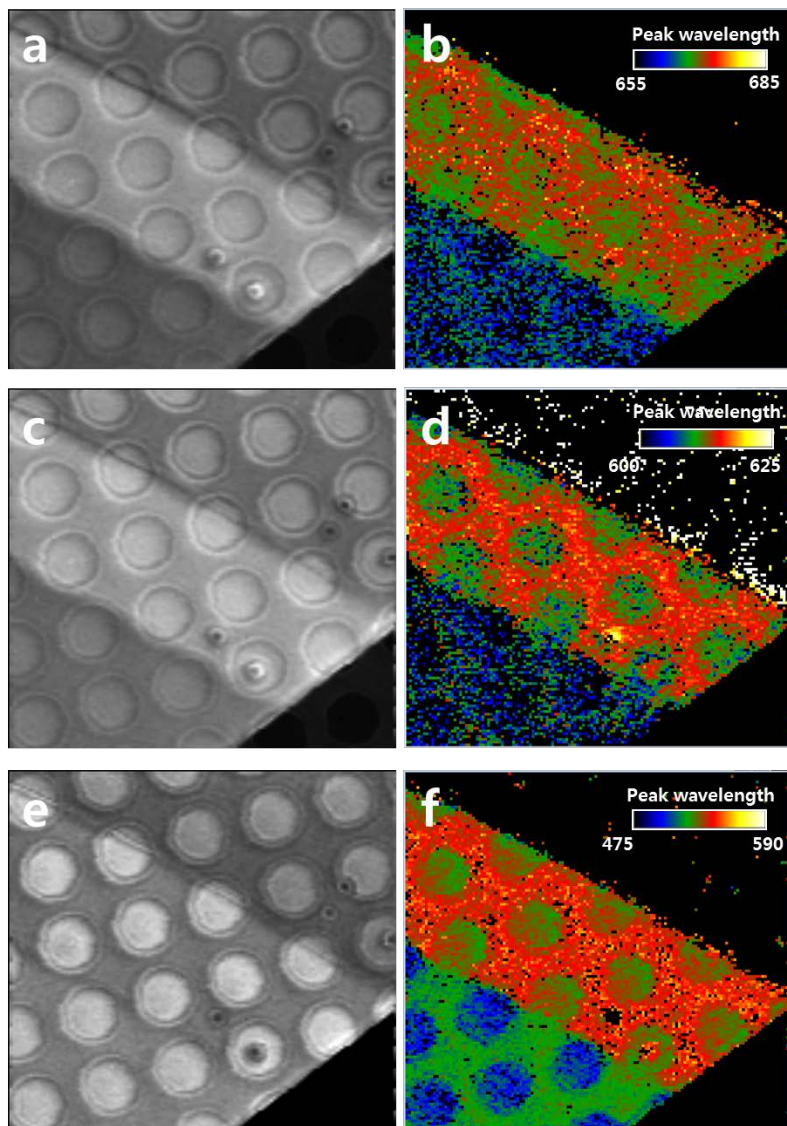


Figure 3.4.8. Monochromatic CL intensity map (left) and peak wavelength map (right) from the emission of exciton A ( $\lambda$ : 475 – 560) (a, b), exciton B ( $\lambda$ : 590 – 620) (c, d) and exciton C ( $\lambda$ : 645 – 680) (e, f) in the MoS<sub>2</sub> flake on the perforated carbon film.

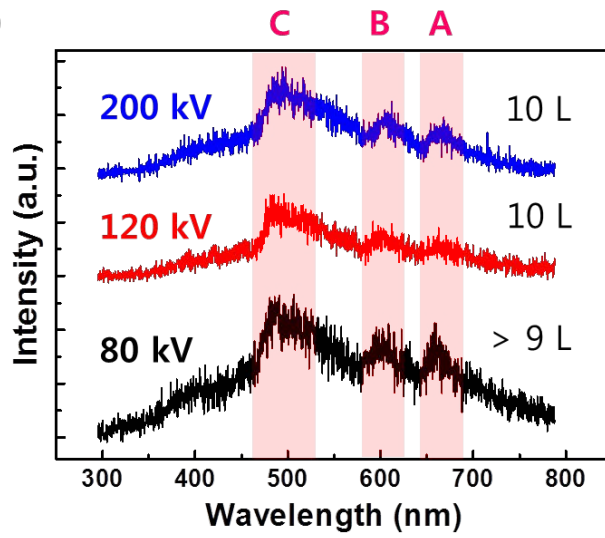
**a****b**

Figure 3.4.9. (a) A setup for TEM-CL measurement at low electron-beam acceleration voltage (80 kV) (b) CL spectra with a different electron-beam acceleration voltage.

### 3. 4. 4. Bibliography

1. Splendiani, A.; Sun, L.; Zhang, Y.; Li, T.; Kim, J.; Chim, C. Y.; Galli, G.; Wang, F. *Nano Lett* **2010**, 10, (4), 1271-5.
2. Mak, K. F.; Lee, C.; Hone, J.; Shan, J.; Heinz, T. F. *Phys Rev Lett* **2010**, 105, (13), 136805.
3. Zeng, H.; Dai, J.; Yao, W.; Xiao, D.; Cui, X. *Nat Nanotechnol* **2012**, 7, (8), 490-3.
4. Mak, K. F.; He, K.; Shan, J.; Heinz, T. F. *Nat Nanotechnol* **2012**, 7, (8), 494-8.
5. Cao, T.; Wang, G.; Han, W.; Ye, H.; Zhu, C.; Shi, J.; Niu, Q.; Tan, P.; Wang, E.; Liu, B.; Feng, J. *Nat Commun* **2012**, 3, 887.
6. Feng, J.; Qian, X.; Huang, C.-W.; Li, J. *Nature Photonics* **2012**, 6, (12), 866-872.
7. He, K.; Poole, C.; Mak, K. F.; Shan, J. *Nano Lett* **2013**, 13, (6), 2931-6.
8. Britnell, L.; Ribeiro, R. M.; Eckmann, A.; Jalil, R.; Belle, B. D.; Mishchenko, A.; Kim, Y. J.; Gorbachev, R. V.; Georgiou, T.; Morozov, S. V.; Grigorenko, A. N.; Geim, A. K.; Casiraghi, C.; Castro Neto, A. H.; Novoselov, K. S. *Science* **2013**, 340, (6138), 1311-4.
9. Carvalho, A.; Ribeiro, R. M.; Castro Neto, A. H. *Physical Review B* **2013**, 88, (11).
10. Radisavljevic, B.; Radenovic, A.; Brivio, J.; Giacometti, V.; Kis, A. *Nat Nanotechnol* **2011**, 6, (3), 147-50.
11. Wang, Q. H.; Kalantar-Zadeh, K.; Kis, A.; Coleman, J. N.; Strano, M. S. *Nat Nanotechnol* **2012**, 7, (11), 699-712.
12. Ponomarev, E.; Gutierrez-Lezama, I.; Ubrig, N.; Morpurgo, A. F. *Nano Lett* **2015**, 15, (12), 8289-94.
13. Eda, G.; Maier, S. A. *ACS Nano* **2013**, 7, (7), 5660-5.
14. Hill, H. M.; Rigosi, A. F.; Roquelet, C.; Chernikov, A.; Berkelbach, T. C.; Reichman, D. R.; Hybertsen, M. S.; Brus, L. E.; Heinz, T. F. *Nano Lett*



- 2015**, 15, (5), 2992-7.
15. Kozawa, D.; Kumar, R.; Carvalho, A.; Kumar Amara, K.; Zhao, W.; Wang, S.; Toh, M.; Ribeiro, R. M.; Castro Neto, A. H.; Matsuda, K.; Eda, G. *Nat Commun* **2014**, 5, 4543.
  16. Steinhoff, A.; Kim, J. H.; Jahnke, F.; Rosner, M.; Kim, D. S.; Lee, C.; Han, G. H.; Jeong, M. S.; Wehling, T. O.; Gies, C. *Nano Lett* **2015**, 15, (10), 6841-7.
  17. Beal, A.; Kinghts, J.; Liang, W. *J Phys C: Solid State Phys* **1972**, 5, (5), 3540.
  18. Qiu, D. Y.; da Jornada, F. H.; Louie, S. G. *Phys Rev Lett* **2013**, 111, (21), 216805.
  19. Cheiwchanchamnangij, T.; Lambrecht, W. R. L. *Physical Review B* **2012**, 85, (20).
  20. Ramasubramaniam, A. *Physical Review B* **2012**, 86, (11).
  21. Yacobi, B. G.; Holt, D. B., *Cathodoluminescence microscopy of inorganic solids*. Plenum Press: New York, 1990; p ix, 292 pages.
  22. Petrov, V. I. *Phys Usp* **1996**, 39, (8), 807.
  23. Mitdank, R.; Sveshnikova, A.; Schulze, E.; Oelgart, G.; Reinhart, F.-K. *Semicond Sci Technol* **1995**, 10, 835.
  24. Lee, C.; Yan, H.; Brus, L. E.; Heinz, T. F.; Hone, J.; Ryu, S. *ACS Nano* **2010**, 4, (5), 2695-700.
  25. Zhao, Y.; Luo, X.; Li, H.; Zhang, J.; Araujo, P. T.; Gan, C. K.; Wu, J.; Zhang, H.; Quek, S. Y.; Dresselhaus, M. S.; Xiong, Q. *Nano Lett* **2013**, 13, (3), 1007-15.
  26. Molina-Sánchez, A.; Sangalli, D.; Hummer, K.; Marini, A.; Wirtz, L. *Physical Review B* **2013**, 88, (4), 045412.
  27. Zhou, W.; Zou, X.; Najmaei, S.; Liu, Z.; Shi, Y.; Kong, J.; Lou, J.; Ajayan, P. M.; Yakobson, B. I.; Idrobo, J. C. *Nano Lett* **2013**, 13, (6), 2615-22.

## Chapter 4. Conclusions

In this thesis, the developments of the TEM-CL system and its applications to the investigation of bandgap-transition characteristics of GaN and MoS<sub>2</sub> were presented. Firstly, it was developed that the novel TEM-CL holder with a retractable light-collecting optics, which is composed of miniaturized optical components and integrated on head part of the holder. By moving the whole optics isolated from built-in cryostat, large CL observation area and successive measurement of EDS signal were guaranteed while maintaining accurate alignment of the optics. Performance and applicability of the system were demonstrated by analyzing ZnO nanowires.

Secondly, the TEM-CL analysis results of polar (0001) GaN LED were discussed. The luminescence properties of V-shape pits, which are the characteristic defects in c-plane InGaN/GaN quantum well structures, were directly correlated with its microstructure. It was clearly revealed that potential barriers, formed by discontinuous QWs around the hexagonal pit, can effectively block the diffusion of carriers into the {10 $\bar{1}$ 1}-faceted QWs and TDs, which increases the effective carrier density contributing radiative recombination.

Thirdly, the emission properties of the semi-polar (11 $\bar{2}$ 2) GaN LED were analyzed. The CL maps clearly identify the type of the extended defects and visualize their distribution at a glance. In addition, it was directly observed that the influence of substrate pattern on the defect reduction. The characteristic surface undulations of the semipolar (11 $\bar{2}$ 2) GaN epi were also investigated. It was clearly observed that the undulations are also present in MQWs composed of the flat (11 $\bar{2}$ 2) facets and the sidewall {01 $\bar{1}$ 1}- facets. The high In-incorporation efficiency of the sidewall {01 $\bar{1}$ 1} facets caused high In composition and long wavelength emission, resulting in non-uniform luminescence and anisotropic emission of LED. It is expected that this result will assist the analysis on the characteristics of the semi-polar GaN epi and the development of the high efficiency GaN LEDs.

Lastly, the luminescence properties of few-layered  $\text{MoS}_2$  were investigated with the optical excitation and the electron beam excitation. As a result, it was observed the peak A and B due to direct excitonic transitions at K point in both PL and CL. The large peak C, which is more close to the quasiparticle bandgap energy, is appeared only in CL. Based on previously reported calculation works, the peak C may correspond to nearly degenerate excitonic transitions near  $\Gamma$  point. The luminescence of the high-energy exciton in  $\text{MoS}_2$  was firstly observed and investigated. I believe that these results provide insight into understanding the excitonic behavior of  $\text{MoS}_2$  and exploring novel optoelectronic applications.

## **Abstract (in Korean)**

---

수십 keV로 가속된 전자가 재료에 조사될 때, 이 전자는 재료 내부에서 연속적인 비탄성 산란 충돌을 일으키며 다수의 가전대 전자를 전도대로 여기시켜 전자-홀 쌍을 생성한다. 이때, 이와 같이 생성된 전자-홀 쌍이 재결합하며 그 과잉 에너지를 광자로 방출하는 과정이 음극형광이다. 이러한 음극형광 신호는, 재료 내부의 전자 구조 특성에 의존하므로, 반도체 재료의 밴드갭 에너지, 엑시톤 및 불순물에 의한 에너지 준위, 결함에 의한 비발광 특성을 분석할 수 있다. 또한, 이러한 음극형광 분석법을 투과전자현미경과 같은 전자현미경에 접목할 경우, 반도체 재료의 고분해능 영상과 연계하여 광 특성을 분석할 수 있는 장점이 있다. 한편, 이러한 유용성에도 불구하고 투과전자현미경 용 음극형광 분석법은 널리 보급되지 못한 실정이다. 그 이유는, 투과전자현미경 내 홀더가 장착되는 공간이 매우 협소하고, 이 공간안에 미약한 광 신호를 효율적으로 집적하는 시스템을 구현하기 어렵기 때문이다. 이로 인해, 일부 연구진들은 투과전자현미경의 경통을 개조하여 음극형광 신호를 수집할 수 있도록 구축한 바 있다.

본 논문에서는, 첫째로, 널리 상용화된 투과전자현미경에 장입이 가능한 이동형 음극형광 수집 시스템을 구축한 결과에 대해 보고한다. 이 시스템은 이동 가능한 반사경 기술을 적용하여, 음극형광 신호 수집뿐만 아니라 에너지 분산 분광 신호 또한 수집할 수 있어, 재료의 구조적, 광학적, 화학적 특성 분석이 가능한 장점이 있다. 둘째로, 개발된 음극형광 시스템을 이용하여 기존 분석법들이 명확히 규명하지 못한 반도체 재료의 광학적 특성을 분석한 내용에 대해 보고한다.

먼저, 질화물계 청색 LED의 양자우물구조에 존재하는 V-자 형태 결함의 특성이 조사되었다. 일반적으로 Sapphire, Si, SiC 등 이종 기판 위에 성장한 GaN 박막은 기판과의 격자상수 차이에 의해 높은 결함 밀도를 갖게 되며, 이러한 결함들은 비발광 재결합 센터로 동작하여 LED (light-emitting diodes)의 효율을 떨어뜨리는 것으로 알려져있다. 한편, InGaN/GaN 양자우물구조를 적용한 청색 LED는 높은 결함 밀도에도 불구하고 높은 내부양자효율 특성을 보여 그 원인을 규명을 위해 많은 연구가 계속되어 왔다.

최근의 연구 결과에 따르면, 저온에서 InGaN 양자우물층 성장 시 생성되는 V-자 형태의 결함 (V-pit)이 LED의 상온 발광 효율 향상에 기여하는 것으로 알려졌다. V-pit은, In 원자와 Ga 원자의 표면 확산 속도 차이에 발생하는 것으로, 전위를 중심으로 여섯 개의  $\{10\bar{1}1\}$  면 양자우물층이 둘러싼 역육각피라미드 구조를 띄며 그 단면 모양이 V자 형태로 나타난다. 이러한 V-pit과 LED 효율의 상관관계를 직접적으로 규명하기 위해, 다수의 선행 연구 그룹들이 저온 PL (photoluminescence), NSOM (near-field scanning optical microscopy), SEM (scanning electron microscopy)-CL 과 같은 다양한 분석기기를 이용하여 결함의 광 특성을 분석하고자 하였으나, 각 분석 기기의 공간분해능 한계로 인해 V-pit의 미세 구조와 그 발광 특성을 직접 연계시키지는 못하였다. 투과전자현미경 용 음극형광 시스템을 이용하여, 전자현미경 이미지와 음극형광 이미지를 교차 분석한 결과, V-pit 중심에 존재하는 전위의 비발광 재결합 특성과, V-pit 주변 양자우물층의 단파장 천이 발광 특성을 확인할 수 있었다. 주목할 만 한 점으로는, V-pit 둘레를 따라  $\{10\bar{1}1\}$  -plane에서 c-plane으로 천이하는 양자우물영역이 비발광하는 것으로 나타났다. 이는 주변부 보다 낮은 In 함량으로 인해 발생한 높은 전위 장벽에 기인한 것으로, 이러한 전위장벽이 carrier sink로 동작하는 중심 전위로 유입되는 carrier의 이동을 막아 LED의 내부양자효율 향상에 기여할 수 있을 것으로 기대된다.

다음으로, 반분극 GaN 박막에 존재하는 면 결함의 특성과 분포가 조사되었다. 기존의 c-plane 분극 GaN는, 자발 분극 및 압전 분극에 의한 전기장이 c축 방향으로 존재하여, 이 전기장이 양자우물구조 내의 전자와 정공을 분리시킴에 따라 LED 효율이 저하되는 한계가 있다. 이를 개선하기 위해, 무분극 및 반분극 GaN 박막을 이용한 LED 개발이 연구되어 왔다. 그러나, 이러한 GaN는, 비록 내부 전기장은 감소하지만, 결정 구조의 비대칭성으로 인해 다양한 결함이 높은 밀도로 존재하는 문제가 있다. 특히 BSF (basal plane stacking faults)는, 비발광 재결합 센터로 알려진 PD (partial dislocations)을 동반하며, 그 자체로도 양자우물구조의 특성 뿐만 아니라 표면 형상 또한 저해하는 것으로 알려져 그 특성 파악과 밀도 감소를 위한 노력이 시급하다. 한편, BSF는 그 구조에 따라 크게 3 가지 종류 ( $I_1$ ,  $I_2$ , E)로 나뉘며, 각기 발생 원리와 LED에 미치는 영향의 정도가 다른 것으로 알려져 있다. 이러한 BSF는,

그 두께가 매우 얇고 3차원의 입체적인 구조를 가져 그 특성을 분석하기 어려운 것으로 알려져 있다. 종래에는 BSF의 종류 판별을 위해 투과전자현미경의  $g \cdot R$  법칙에 기반한 영상법이 사용되었으나, 이는 매우 한정적인 영역만을 관찰할 수 있고 장시간의 노력을 필요로 한다. 본 논문에서는, (11 $\bar{2}2$ )면 GaN의 단면과 평면의 시편에 대해 음극형광 분석을 실시한 결과, 광지문 분석법을 기반으로,  $I_1$ -BSF와  $I_2$ -BSF를 손쉽게 구분할 수 있었으며 그 분포를 한눈에 파악할 수 있었다. 이러한 음극형광 분석 기술은, 추후 다양한 무분극 및 반분극 GaN 에피 분석에 이용할 경우, 효과적으로 결함의 분포를 파악하고 에피 성장 기술 개선에 기여할 것으로 기대된다.

이에 더해, 반분극 GaN 에피에서 특징적으로 나타나는 비 대칭형 파도 모양의 에피의 표면과 양자우물간의 상관 관계 또한 조사되었다. 앞서 언급한 바와 같이, 반분극 기판은 결정 구조의 비대칭성으로 인해, 비대칭적 표면 형상과 이방형 발광 특성을 갖는 것으로 보고되어 왔으나, 기존 분석법들의 공간분해능 한계로 인해 그 구조적, 광학적 특성이 명확히 규명되지 못한 한계가 있다. 본 논문에서는, 음극형광 분석을 통해 표면 뿐만 아니라 하단의 양자우물구조 또한 파도 형상을 나타내는 것을 확인하였으며, 평탄면과 경사면이 각기 (11 $\bar{2}2$ ) 면과 {01 $\bar{1}1$ } 면에 대응하고, 경사면인 {01 $\bar{1}1$ } 면은 높은 인듐 함량으로 인해 장파장을 방출하는 것을 직접적으로 확인하였다.

마지막으로, 최근들어 이차원 전자 소자 재료로 각광받고 있는 전이금속 칼코겐 화합물의 발광 특성이 조사되었다. MoS<sub>2</sub> (Molybdenum disulfide)는, 층상 구조를 갖고 있으며 그 두께가 얇아짐에 따라 밴드갭이 증가하며, 한 층만 존재할 경우 간접형 밴드 구조에서 직접형 밴드 구조로 천이하는 독특한 특성을 갖는 것으로 알려졌다. 본 논문에서는, 수 층의 MoS<sub>2</sub> 시편을 제작하고, 이를 광학적 여기 (PL)를 통한 발광 특성을 측정하고, 전자빔 여기 (CL)를 통한 발광 특성을 측정하여 비교하였다. 그 결과, PL과 CL 모두 K-위치의 직접 천이에 의한 엑시톤 신호 A, B가 검출되었으며 PL에서는 층수가 얇아짐에 따라 그 신호가 증가하다 단일 층이 될 때 그 크기가 급증한 반면, CL에서는 감소하는 것이 관찰되었다. 흡수 스펙트럼에서만 관찰되는 것으로 보고된 C 엑시톤의 에너지 영역에서 CL 신호가 검출되어, 전자빔에

의한 큰 에너지 및 모멘텀 전달에 의해  $\Gamma$ -위치 부근의 높은 에너지 준위에 여기된 전자가 존재하여 발생하였을 가능성이 있는 것으로 보고 있다.

주요어: 음극형광, 투과전자현미경, 선 전위, 면 결함, 양자우물, 질화갈륨, 발광 다이오드, 전이금속 칼코겐 화합물

학 번: 2013-30182

신 미 향

# Curriculum Vitae

---

Mi-Hyang Sheen

*In-situ* Electron Microscopy Laboratory

Department of Materials Science and Engineering

Seoul National University

E-mail: mhsheen@snu.ac.kr

Tel.: +82-2-878-5010 Fax: +82-2-878-5010

## ■ Education

- |                       |   |
|-----------------------|---|
| Mar. 2013 – Present   | Ph.D course, Department of Materials Science and Engineering, College of Engineering, Seoul National University, Seoul, Republic of Korea (Advisor: Prof. Young-Woon Kim) |
| Mar. 2008 – Feb. 2010 | M.S., Department of Electrical Engineering, Pohang University of Science and Technology, Pohang, Republic of Korea (Advisor: Prof. O'Dae Kwon)                            |
| Mar. 2003 – Feb. 2008 | B.S., Department of Electrical and Electronic Communications Engineering, Pusan National University, Busan, Republic of Korea   |

## ■ Scholarships and Awards

- |                       |  |
|-----------------------|--|
| Sep. 2013 – Mar. 2015 | Teaching Assistant Scholarship, Seoul National University  |
| Mar. 2013 – Aug. 2013 | Academic Excellence Scholarship, Seoul National University |



## ■ Experimental Skills

### 1. Preparation of TEM specimen

Mechanical polishing & Ion milling (PIPS, Gatan)

### 2. Transmission Electron Microscope (TEM) Operation

Instruments: JEM-200CX, JEM-3000F, JEM-2010F, JEM-2100F, ARM-200F, Tecnai-F20, Tecnai-F30

Techniques: high-resolution (HR) imaging, bright field (BF) and dark field (DF) imaging, weak beam dark field imaging (WBDF), convergent beam electron diffraction (CBED), selected area diffraction (SAD), nanobeam electron diffraction (NBD), scanning transmission electron microscopy (STEM), electron energy loss spectroscopy (EELS), energy dispersive x-ray spectroscopy (EDS), cathodoluminescence (CL)

### 3. Scanning Electron Microscope (SEM) Operation

Instrument: JSM-6390LV, JSM-5600

### 4. Focus Ion Beam (FIB) Operation

Instrument: SMI3050SE (SII Nanotechnology)

### 5. X-ray Photoelectron Spectroscopy (XPS) Operation

Instrument: Sigma Probe (Thermo VG Scientific)

### 6. X-ray Diffraction (XRD) Operation

Instrument: X'Pert Pro (PANalytical)

### 7. EM simulation tools

JEMS (Java version of the EMS electron microscopy simulation program), Crystal maker

### 8. Image editing tools

ImageJ (Image stack generating and editing), DM (Digital Micrograph), Camtasia (Movie making), VirtualDub (Movie editing)

### 9. Instrument design tools

Autodesk Inventor (3D design), Autodesk AutoCAD (2D design)

## ■ Patents

Young-Woon Kim, **Mi-Hyang Sheen**, ‘전자현미경용 홀더장치’, 10-2015-0068007 (application), 2015 (Korea patent)

## ■ List of Publications

1. **Mi-Hyang Sheen**, Sung-Dae Kim, Jong-Hwan Lee, Jong-In Shim, and Young-Woon Kim, “V-pits as Barriers to Diffusion of Carriers in InGaN/GaN Quantum Wells”, *Journal of Electronic Materials*, 44, 4134 (2015)
2. Pil-Seok Ko, Kyoung-Seok Park, Yeo-Chang Yoon, **Mi-Hyang Sheen**, Sam-Dong Kim, “Interface characteristics of spin-on-dielectric SiO<sub>x</sub>-buffered passivation layers for AlGaIn/GaN high electron mobility transistors”, *Thin Solid Films*, 589, 838 (2015)
3. Chandreswar Mahata, Il-Kwon Oh, Chang Mo Yoon, Chang Wan Lee, Jungmok Seo, Hassan Algadi, **Mi-Hyang Sheen**, Young-Woon Kim, Hyungjun Kim and Taeyoon Lee, “The impact of atomic layer deposited SiO<sub>2</sub> passivation for high-k Ta<sub>1-x</sub>Zr<sub>x</sub>O on the InP substrate”, *J. Mater. Chem. C*, 3, 10293 (2015)
4. Kim, D.K., Kim, Y.C., **Sheen, M.H.** and O’Dae Kwon, “Spatiotemporal dynamics in Rayleigh band of photonic quantum ring laser”, *Opt. Quant. Electron.*, 41, 913 (2009)
5. Y. C. Kim, **M. H. Shin**, K. H. Chae, C. H. Kim and O’Dae Kwon, “Photonic quantum ring flower laser of whispering cave mode”, *Electronics Letters*, 45, 739 (2009)
6. O’Dae Kwon, D. K. Kim, J. H. Yoon, Y. C. Kim, Y. H. Jang, and **M. H. Shin**, “Photonic quantum ring laser of 3D whispering cave mode”, *Microelectronics Journal*, 40, 570 (2009)
7. O’Dae Kwon, **M. H. Sheen** and Y. C. Kim, “Photonic Quantum Ring Laser of Whispering Cave Mode”, *Advances in Optical and Photonic Devices*, INTECH (2010)

## ■ International Conferences

### Oral presentations

1. **Mi-Hyang Sheen**, Sung-Dae Kim, Jongjin Jang, Okhyun Nam, Young-Woon Kim, “Investigation on defect related luminescence in semipolar InGaN/GaN quantum well by using TEM-CL”, *Asia-Pacific Microscopy Conference11*, Phuket, Thailand (2016)
2. **Mi-Hyang Sheen**, Sung-Dae Kim, Jong-Hwan Lee, Hyun-Ju Kim, Jong-In Shim, and Young-Woon Kim, “Role of defect as a diffusion barrier for carriers in InGaN/GaN quantum wells”, *East-Asia Microscopy Conference2*, Himeji, Japan (2015)
3. **M. H. Sheen**, S. D. Kim, and Y. Kim, “Investigation on Electro-Optical Property of GaN LED using TEM-EBIC combined with cathodoluminescence,” *226<sup>th</sup> Meeting of The Electrochemical Society*, Cancun, Mexico (2014)
4. Jong-Hwan Lee, **Mi-Hyang Sheen**, Sung-Dae Kim, and Young-Woon Kim, “Defect Concentration Mapping of BaTiO<sub>3</sub> Using Transmission Electron Microscope Equipped with Cathodoluminescence”, *Meeting of Materials Research Society*, San Francisco, USA (2014)
5. **M. H. Shin**, Y. C. Kim, K. H. Chae, C. H. Kim and O'Dae Kwon, “Multi-petal flower laser of photonic quantum ring can outperform LED in power consumption and emission”, *International Conference on Electrical Engineering*, Shenyang, China (2009)
6. **M. H. Shin**, Y. C. Kim, K. H. Chae, C. H. Kim and O'Dae Kwon, “7-fold power increase from 12-petal flower laser of photonic quantum ring for replacing the LED display”, *Display & Solid State Lighting Conference*, Seoul, Republic of Korea (2009)
7. **M. H. Shin**, Y. C. Kim, K. H. Chae, C. H. Kim and O'Dae Kwon, “Multi-petal flower photonic quantum ring laser of whispering cave modes can outperform LEDs”, *International Workshop on Microcavities and Their Applications*, Seoul, Republic of Korea (2009)

Poster presentations

1. **M. H. Sheen**, M. C. Lee, J. H. Lee and Y. W. Kim, “Investigation on polarization induced electro-optical property of GaN LED using TEM-EBIC combined with cathodoluminescence”, *Microscopy & MicroAnalysis*, Hartford, CT, USA (2014)
2. Jong-Hwan Lee, Sung-Dae Kim, **Mi-Hyang Sheen**, Young-Woon Kim, “Optical emission characteristics from the oxygen deprived SrTiO<sub>3</sub> using TEM cathodoluminescence”, *Meeting of Materials Research Society*, San Francisco, USA (2014)